UNCLASSIFIED

AD NUMBER
AD911378
NEW LIMITATION CHANGE
TO **Approved for public release, distribution unlimited**
FROM **Distribution authorized to U.S. Gov't. agencies only; Test and Evaluation; 02 JUL 1973. Other requests shall be referred to U.S. Army Mobility Equipment Research and Development Center, Fort Belvoir, VA 22060.**
AUTHORITY
USAMERDC D/A ltr, 15 Jan 1974

THIS PAGE IS UNCLASSIFIED

1

Report No. U1-840150-F

IMAGING CROWD SURVEILLANCE SYSTEM

FINAL TECHNICAL REPORT

Forrest D. Colegrove
James E. Robinson
Michael A. Kinch
David R. Boyd
Jack K. Hickman
Cecil R. Coale

May 1973

for

U.S. ARMY MOBILITY EQUIPMENT RESEARCH
AND DEVELOPMENT CENTER
FORT BELVOIR, VIRGINIA 22060

CONTRACT NO. DAAK02-71-C-0429

EQUIPMENT GROUP
TEXAS INSTRUMENTS INCORPORATED
P.O. BOX 6015, DALLAS, TEXAS, 75222

T+E

2 JUL 1973

Each transmittal of this document outside the agencies of the U.S. Government must have prior approval of the Commander, U.S. Army Mobility Equipment Research and Development Center, Fort Belvoir, Virginia, 22060.

Report No. U1-840150-F

IMAGING CROWD SURVEILLANCE SYSTEM

FINAL TECHNICAL REPORT

Forrest D. Colegrove
James E. Robinson
Michael A. Kinch
David R. Boyd
Jack K. Hickman
Cecil R. Coale

May 1973

for

U.S. ARMY MOBILITY EQUIPMENT RESEARCH
AND DEVELOPMENT CENTER
FORT BELVOIR, VIRGINIA 22060

CONTRACT NO. DAAK02-71-C-0429

EQUIPMENT GROUP
TEXAS INSTRUMENTS INCORPORATED
P.O. BOX 6015, DALLAS, TEXAS, 75222

T+E

2 JUL 1973

Each transmittal of this document outside the agencies of the U.S. Government must have prior approval of the Commander, U.S. Army Mobility Equipment Research and Development Center, Fort Belvoir, Virginia, 22060.

ABSTRACT

An instrument to test the feasibility of imaging weapons concealed in a person's clothing has been developed. A simple object-plane scanner, which records images on film, has been used with two sensors. The gallium arsenide photodetector has peak response at a wavelength of 0.285 mm and the indium antimonide free electron bolometer responds at wavelengths near 0.75 mm. The performance of this instrument is analyzed and potential improvements are suggested. The imagery obtained with the two sensors is compared.

TABLE OF CONTENTS

Section *Title* *Page*

LIST OF ILLUSTRATIONS

LIST OF TABLES

SECTION I

INTRODUCTION

The Imaging Crowd Surveillance System (ICSS) was built to test the feasibility of using passive radiation in the wavelength range of 0.2 to 1.0 millimeter to detect weapons concealed in clothing. Feasibility has been demonstrated and it should be possible to develop a system that could display real-time imagery. The operator would be able to see the shape of metallic objects carried in the clothing of individuals in a crowd. On the basis of shape, location and possibly the action of the person, he would be able to make a judgment concerning the potential threat to public figures appearing before the crowd. This system might be set up in a fixed location within a building or on a vehicle for use outdoors.

The same concept could be used to observe people passing through a controlled access, especially if used in conjunction with a nonimaging metal detector. The region of observation would not need to be confined, particularly, since the surveillance could be done from a distance of 20 or more feet. Image interpretation by the operator would greatly reduce the false-alarm rate with the combined system, even when a fairly sensitive nonimaging metal detector was used.

The concept to be tested was based on the fact that clothing appears to be partially transparent at wavelengths longer than 0.2 mm. The transmission of a few types of cloth is shown in Figure 1. These are all single-layer materials. At shorter wavelengths, clothing is opaque

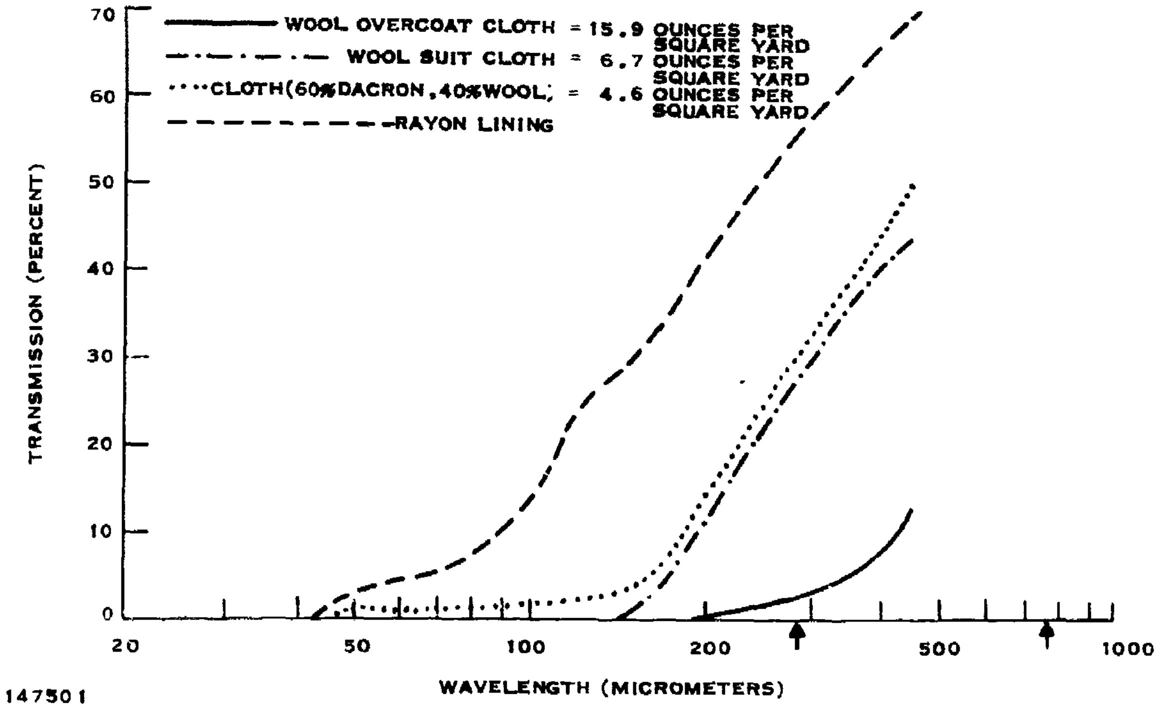

Figure 1. Infrared Spectral Transmission of Cloth

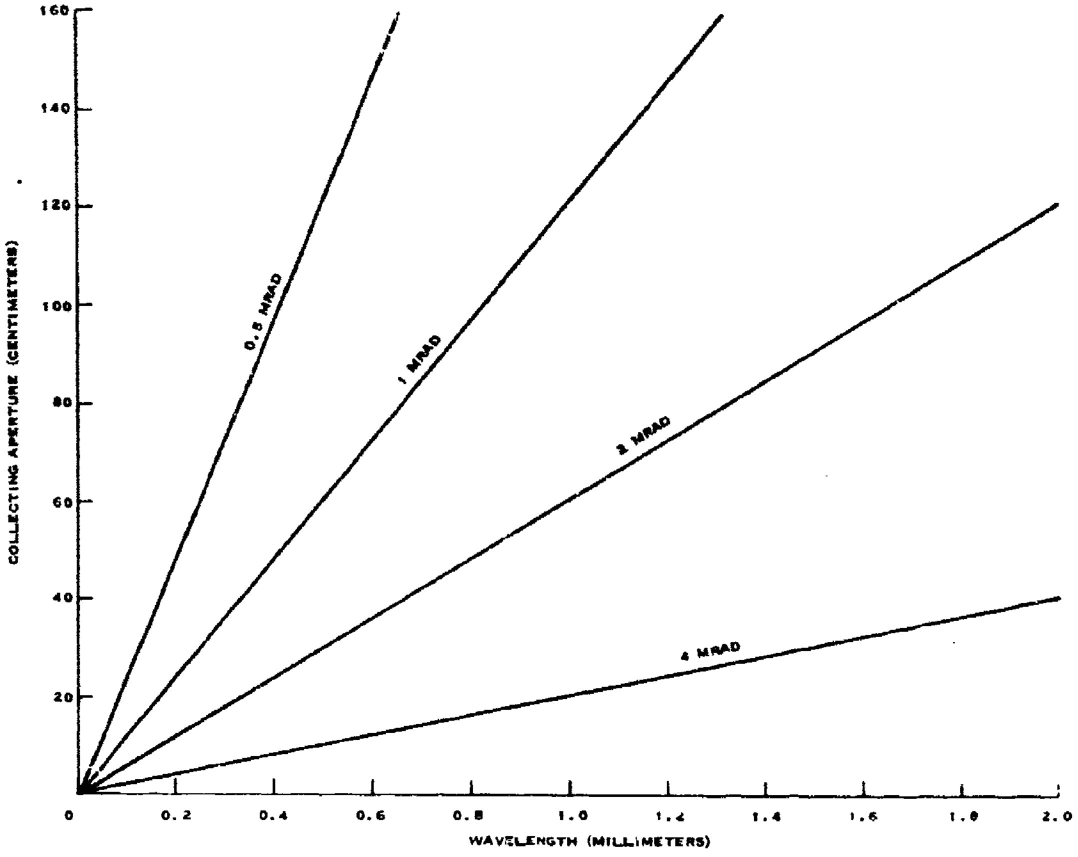

147502

Figure 2. Diffraction-Limited Collecting Aperture Required at Submillimeter Wavelengths

out to the X-ray portion of the electromagnetic spectrum, where an active system would be required. The health hazard for an X-ray system designed to operate at distances greater than a few feet would probably be unacceptably high. Therefore, if objects concealed on a person are to be detected 20 feet away, or more, submillimeter or longer wavelength radiation will most likely be necessary. If this detection can be accomplished passively, no hazard exists.

Two video (fast) detectors with adequate sensitivity are available in the submillimeter portion of the spectrum. The wavelengths of their peak response to blackbody radiation are indicated by the two arrows in Figure 1. Although transmission improves with wavelength, the energy available for passive imaging decreases and the resolution for a given aperture becomes worse as shown in Figure 2.

The most expedient method for obtaining images with these two detectors was to build an object plane scanner based on an existing instrument that uses a single detector. The medical thermoscope concept used for this demonstration records the image line by line on an oscilloscope from which a picture is taken.

In Section II, a detailed description of the feasibility demonstration system is given. Overall system performance, including pictures taken with both sensors, is presented in Section III and a discussion of possible improvements and modifications is given in Section IV.

SECTION II

DESIGN AND OPERATION

A. Sensors

Two types of detectors were used, gallium arsenide and indium antimonide. Each detector was mounted in modified research Dewars with appropriate cold shields and filters. The characteristics of each of these components are described below.

1. Indium Antimonide Electron Bolometer

The InSb bolometer is a thermal detector which utilizes the electron gas in n-type InSb at low temperatures as a sensing element. At temperatures below 10°K, the electrons are only weakly coupled to the semiconductor lattice, and the absorption of radiant energy effectively raises the temperature of the electron gas above the lattice temperature. This increase manifests itself as a change in resistance.

The responsivity of the bolometer[1] to incident radiation, ΔW, for constant-current bias, is given by

$$S = \frac{\Delta V}{\Delta W} = \frac{\eta V \gamma}{G} \tag{1}$$

where η is the quantum efficiency for absorption of radiation, V is the applied dc bias voltage across the detecting element, $\gamma \equiv (dR/dT)/R$, the temperature coefficient of resistance of the detector, and G represents the thermal conductance of the electron gas with its surroundings, that is, the lattice.

For InSb at low temperatures, $R \alpha T^Z$, where $0.5 < Z < 1.5$ depending on carrier concentration. For $2 \times 10^{13} < n < 6 \times 10^{13}$, $Z \cong 1.0$. Thus,

$$\frac{1}{R}\frac{dR}{dT} \simeq \frac{1}{T} \tag{2}$$

Under optimum dc bias conditions

$$\frac{V^2}{R} \simeq G\,\Delta T \simeq G \tag{3}$$

for $\Delta T \cong 1°K$.

Substituting Equations (2) and (3) into (1), the detector responsivity is

$$S = \frac{\eta R^{1/2}}{G^{1/2} T} \tag{4}$$

Because the absorption mechanism in this hot electron bolometer is one of free carrier absorption, η depends strongly on the value of resistance. Electromagnetic theory calculations[2] show that the absorption coefficient is given by

$$\alpha = \frac{\sigma}{c\epsilon_o}\left(\frac{1}{\epsilon}\right)^{1/2} \tag{5}$$

where σ, the material conductivity, is given by

$$\sigma = \frac{\sigma_o}{1 + \omega^2\tau^2} \tag{6}$$

σ_o is the dc conductivity, and τ the momentum relaxation time for electrons. The velocity of light is c, ϵ_o the permittivity of free space and ϵ the relative permittivity of the semiconductor. For InSb, from Equation (5),

$$\alpha = 10^2\sigma \text{ cm}^{-1} \tag{7}$$

Thus, for optimum detector thickness (provided no integrating optics are used), $t \cong \alpha^{-1}$; and for a square element, from Equation (7)

$$R = (\sigma t)^{-1} = 10^2 \ \Omega \tag{8}$$

The remaining quantity in Equation (4) is the thermal conductance, G, which is determined by the electron-phonon interactions in the semiconductor at the operating temperature. Quantitative measurements[3] of this parameter have shown that a reasonable value for the quantity, G_e, representing the thermal conductance per electron, is approximately 7×10^{-17} W/°K.

Thus, from Equation (4), for T = 4°K,

$$S = \frac{\eta R^{1/2}}{G^{1/2} T} \simeq 1.5 \times 10^8 (N)^{-1/2} \tag{9}$$

where N represents the total number of electrons in the detector. If it is assumed that the mobility at 4.2°K is $3 \times 10^4 \text{ cm}^2\text{V}^{-1}\text{ s}^{-1}$, then as the thickness to optimize absorption is $(10^2\sigma)^{-1}$, for a square detector of side L,

$$\begin{aligned} N &= n \cdot \frac{L^2}{10^2 n \cdot q \cdot 3 \times 10^4} \\ &= 2 \times 10^{12} \cdot L^2 \end{aligned} \tag{10}$$

Thus, from Equation (9)

$$S \cong 10^2 \ L^{-1} \text{ volts per watt} \tag{11}$$

Hence, for a 1-mm square detector, the optimum responsivity is $\cong 10^3 \text{ V} \cdot \text{W}^{-1}$.

This figure obviously can be improved upon if some form of integrating optics is employed, as then, the active volume of the device can be reduced while still achieving the same quantum efficiency.

The noise equivalent power (NEP) of the device will be determined by the responsivity given in Equation (11) and the dominant noise mechanism. The ultimate NEP would be achieved for the Johnson noise-limited case. It was determined earlier that the optimum detector resistance is $10^2\ \Omega$. Thus,

$$\begin{aligned} V_J &= (4kTR\Delta f)^{1/2} \\ &= 1.5 \times 10^{-10}\ \mathrm{V \cdot Hz^{-1/2}} \end{aligned} \tag{12}$$

However, temperature fluctuations of the electron gas normally contribute a certain amount of noise in these electronic bolometers and this effect will raise the noise voltage across the detector by some 50 to 100 percent. Thus, the noise voltage in the ideal case will be given by

$$V_N \cong 2.5 \text{ to } 3 \times 10^{-10}\ \mathrm{V \cdot Hz^{-1/2}} \tag{13}$$

which in turn, when combined with Equation (11) yields an NEP for a 1-mm square detector of $\cong 3 \times 10^{-13}\ \mathrm{W \cdot Hz^{-1/2}}$. This would correspond to a peak $D^* \cong 3 \times 10^{11}\ \mathrm{cm\ Hz^{1/2} \cdot W^{-1}}$.

The response time of the electron bolometer is given by

$$\tau_r \cong C/G \tag{14}$$

where C represents the heat capacity of the electron gas, which in the nondegenerate case is $\cong (3/2)Nk$, where k is a Boltzmann's constant. Thus,

$$\begin{aligned} \tau_r &\simeq 1.5k/G_e \\ &\text{or} \\ \tau_r &\simeq 3 \times 10^{-7}\ \mathrm{s} \end{aligned} \tag{15}$$

using the value for the thermal conductance per electron quoted earlier. Thus, the bolometer, although in essence a thermal detector, is inherently quite fast, with a bandwidth capability approaching 1 MHz.

The spectral response of the detector is determined by the absorption mechanism, that is, free carrier absorption, as expressed in Equations (5) and (6). Classical conductivity theory yields a $(1 + \omega^2\tau^2)^{-1}$ dependence on the absorption coefficient, thus, when $\omega\tau > 1$, the spectral response should roll off as λ^2. The measured spectral response of the detector is flat to $\lambda < 1000\ \mu\mathrm{m}$, and then begins to roll off approximately as λ^3. This type of behavior is predicted from quantum theory of free carrier absorption. The peak response of the InSb detector to blackbody radiation occurs in the region of $750\ \mu\mathrm{m}$.

A summary of expected detection characteristics based on calculations for the optimum square detector of 100 ohms is given below.

1. Responsivity $\cong$ 1,000 volts W^{-1}
2. NEP $\cong 3 \times 10^{-13}$ W $Hz^{-1/2}$
3. D* $\cong 3 \times 10^{11}$ cm $Hz^{1/2}$ W^{-1}
4. Response time $\tau_r \cong 3 \times 10^{-7}$ seconds
5. Flat spectral response for $\lambda > 1{,}000$, short wavelength rolloff as λ^3.

The preamplifier developed for use with the InSb bolometer has an equivalent noise at the input $\cong 5 \times 10^{-10}$ V $\cdot$ $Hz^{-1/2}$, and represents the state-of-the-art for this type preamplifier. This is larger than the noise predicted from the ideal device and would degrade the estimated NEP and D* values in the calculations for the 100-ohm detector. To overcome this preamplifier limitation, detectors with resistances greater than 100 ohms were fabricated. The increase in device responsivity, coupled with the fixed preamplifier noise limitation, more than offset the small loss in absorption.

Typical detector resistances are from 200 to 700 ohms. The fabrication of these devices and the characteristics of these detectors as measured with a blackbody are discussed in the following paragraphs. In rare instances, a detector was observed to go through an aging process in which the operating resistance and the detector responsivity increased by more than an order of magnitude. Because the mode of operation of this type detector is not well understood, discussion of its characteristics will be deferred to the discussion on increased sensitivity in Subsection IV.D.

a. Fabrication Procedure

Indium antimonide (InSb) material was supplied in wafer form by Cominco American Incorporated, Spokane, Washington. These 20-mil-thick wafers were cut from various regions of a single crystal boule and have a resistivity of 0.19 to 0.59 ohm-cm, a Hall mobility of 5.1 to 5.8 $\times 10^5$ cm^2/V-s, and a net carrier concentration of 2.1 to 5.7 $\times 10^{13}$ cm^{-3} at 77°K. The best units were fabricated from the most closely compensated material. At 4.2°K this material had a 10 ohm-cm resistivity and a mobility calculated to be 3.5×10^4 cm^2/V-s. Then, to obtain the optimum detector resistance of 100 ohms, a detector thickness of about 1 mm is required.

As pointed out, best results were obtained with higher resistance detectors which are considerably thinner than 1 mm. Typically, 20-mil-thick rectangular chips (60 by 90 mil) are polished to a 10-mil final thickness using 5.0-μm alumina grit. The surface damage resulting from this lapping process is removed by polishing the chips with 0.3-μm and then 0.05-μm alumina grit.

The electrical contacts are formed by alloying sulphur-doped indium onto the ends of the chip. The sulphur was found to be necessary to form good ohmic contact to the InSb. The temperature at which this alloying takes place was found to be a crucial parameter in determining detector characteristics. When this temperature is kept to a minimum, i.e., a value near 270°C, devices with good detection characteristics could be consistently reproduced. At higher temperatures ($T > 300$°C), more erratic results including aging effects were observed. These will be discussed in Subsection IV.D.

Several chemical etches were used to improve surface finish and to reduce 1/f noise in the device. Of these, the best seems to be HNO^3:HF:acetic acid in 5:3:3 volumetric ratio. This etch acts fairly rapidly; an etch time of 3 to 5 seconds is required to give a clean surface having a slight orange-peel like appearance. The detector is mounted on a sapphire substrate and 1-mil gold leads are ball-bonded to the indium contacts. The finished device is then ready for measurement.

b. Detector Measurement

A reasonable estimate of detector sensitivity can be obtained from a simple analysis of the current-voltage characteristic. This data is taken at 4.2°K by mounting the detector on a dip stick and immersing it in a bath of liquid helium. The current-voltage relationship for a typical detector is shown in Figure 3. The beginning of the nonohmic region at a 40-μA bias current results from the electric field heating of the electron gas to a temperature slightly above that of the lattice. Observing this nonohmic behavior is a quick indication that a particular device will be sensitive to submillimeter radiation and is worthy of the time required for further investigation. A very rough estimate of device responsivity can be obtained from the I-V data by noting that

$$S = dV/dW \tag{16}$$

$$dW = IdV + VdI \tag{17}$$

$$dI/dV \cong R^{-1} \tag{18}$$

$$S \cong (2I)^{-1} \tag{19}$$

where I is taken at the operating point of the device near the beginning of the nonohmic region. In this instance, a responsivity in the mid 10^3-V/W range is estimated.

Because a calibrated source of submillimeter radiation was unavailable, a blackbody radiator was used to measure detector responsivity. In these measurements, errors introduced while estimating filter transmission characteristics and detector wavelength response can easily give rise to errors of a factor of two or three in responsivity. At the submillimeter wavelengths of interest, normal blackbody radiators no longer act in exact accord with Planck's radiation formula.[4] Corrections for this nonideal behavior were not taken into account. Hence, detector responsivities obtained from the blackbody measurements must be considered as estimates.

Bias dependence of the measured responsivity is displayed in Figure 4. The peak in this curve corresponds to about 10^4-V/W responsivity, which is in rough agreement with that estimated from the I-V data. It is noted that these values are somewhat higher than the 10^3 V/W predicted for the free-electron bolometer. However, because of the crudeness of these calculations and the possible errors in the blackbody measurements, it is thought that the typical detector, as characterized in Figure 3, is behaving as a free-electron bolometer.

As mentioned earlier, system noise is limited by the 0.5 $nV/Hz^{1/2}$ input-noise voltage of the preamplifier. At lower frequencies, the detector 1/f noise rises above this limit (Figure 5). This data is a marked improvement over that obtained from earlier detectors in which the "knee" occurred at about 400 Hz. Further improvement in these noise characteristics at the

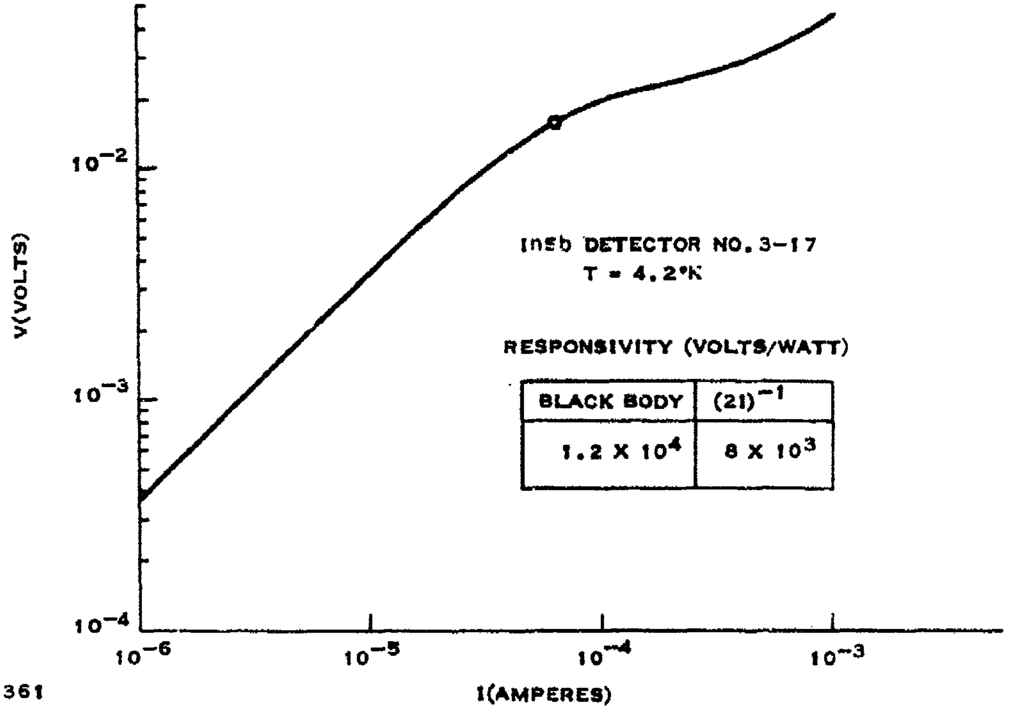

162361

Figure 3. Current-Voltage Relationship for the Typical InSb Free Electron Bolometer.

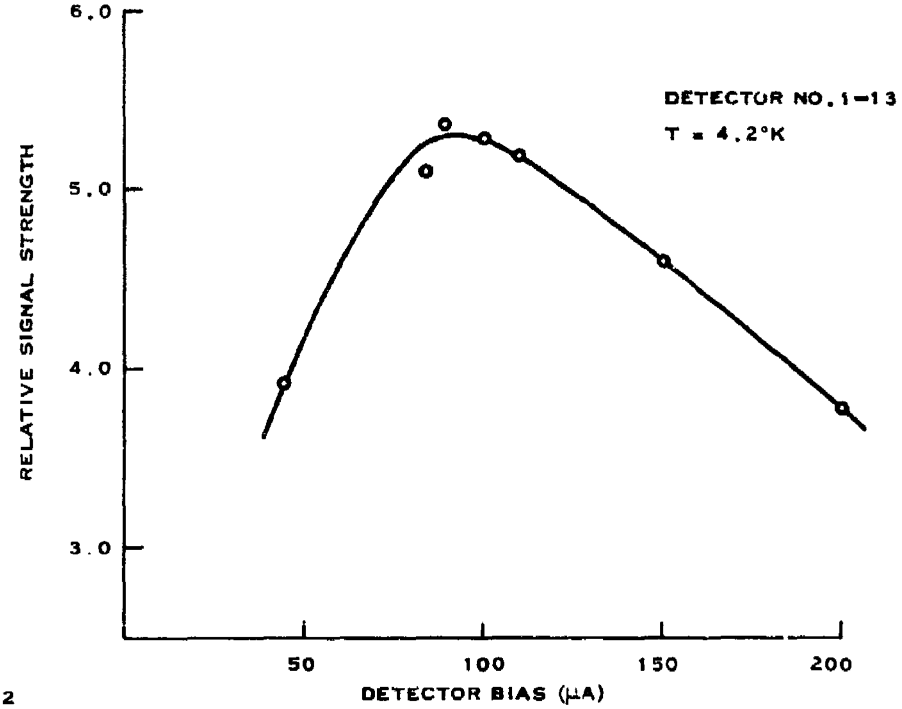

162362

Figure 4. Detector Responsivity Dependence on Bias Current

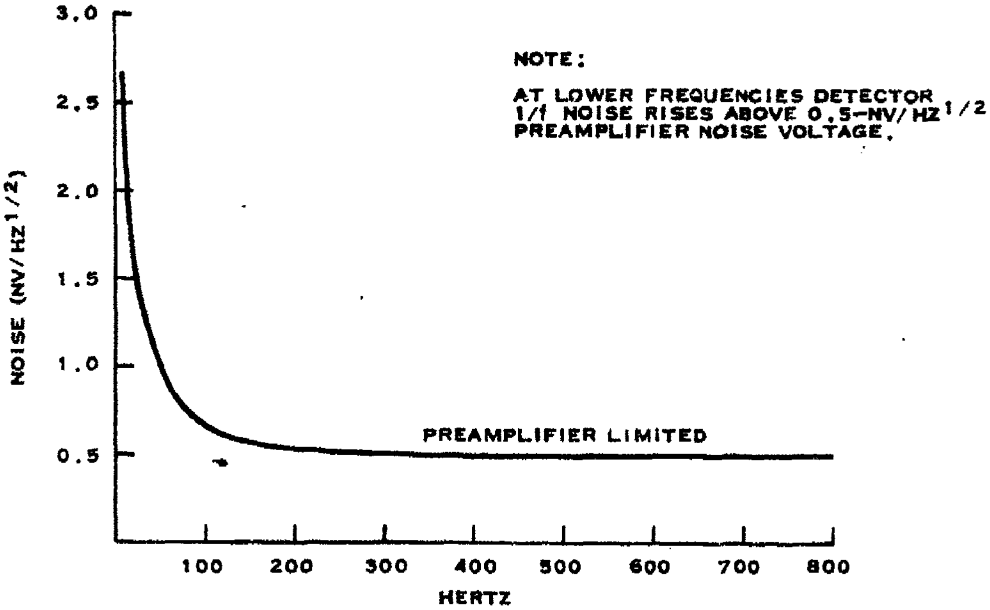

162360

Figure 5. System Noise as a Function of Frequency

lower frequencies may possibly be obtained with additional work on the surface-preparation and contacting techniques.

The system NEP, as measured with the typical detector at a chopping frequency of 800 Hz, ranges between 1×10^{-13} and 3×10^{-13} W/Hz$^{1/2}$. This corresponds to a peak D* approaching 10^{12} cm Hz$^{1/2}$ W^{-1}. Further improvement in detection characteristics might be obtained by using condensing light cones and integrating cavities to help reduce the active detector volume while still maintaining high quantum efficiency.

2. Gallium Arsenide Extrinsic Photoconductor

The Gallium Arsenide (GaAs) photoconductive detector used in this work was supplied by Dr. G. Stillman of Lincoln Laboratories, and has been described at length in the literature.[5] It is discussed here only briefly. The photon-induced transition involved is bound state to bound state (1s → 2p), which in itself does not result in photoconductivity. The transition from the 2p level to the conduction band is made via phonons, and thus, the optimum temperature operation range of this device is quite restricted. The temperature must be low enough for a significant number of donors to be neutralized (1s states occupied) for the first stage of the transition (1s → 2p), and yet high enough so that enough phonons are available for the second transition (2p → conduction band). The optimum range of temperature is 4° to 6.0°K.

The unusual nature of the photoconductive transition means that the spectral response is very sharp, and for the Dewar and filter arrangement is centered around 286 μm (the 1s → 2p transition is $\cong 4.4 \times 10^{-3}$ eV), with a spectral bandwidth of approximately 40 μm. The detector element consists of a high-purity epitaxial layer of n-type GaAs on a substrate of semi-insulating GaAs and is 1.7-mm square. The measured resistance under the reduced background conditions of operation was 8 X 10^6 Ω. The optimum bias voltage for the detector was 0.15 V. At higher bias levels, the signal and the signal to noise began to degrade, because of impact ionization of the shallow donor levels involved.

Blackbody measurements yielded a value for blackbody responsivity $S_{bb} \cong 60$ V W^{-1}, and a blackbody $D^* \cong 5 \times 10^7$ cm $Hz^{1/2}W^{-1}$. Using the measured spectral response, these translate into peak values of $S_\lambda \cong 10^6$ V W^{-1}, and $D_\lambda{}^* \cong 10^{12}$ cm $Hz^{1/2}W^{-1}$. The D* value corresponds to an NEP (noise equivalent power in 1-Hz bandwidth) 2 X 10^{-13} W/$Hz^{-1/2}$.

The measured noise voltage at optimum bias was 2 X 10^{-7} V $Hz^{-1/2}$ and there was no indication of excess 1/f noise down to frequencies of 20 Hz.

The frequency response of the detector is limited by the high impedance of the device in conjunction with the input parameters of the preamplifier. This aspect of the detector performance is discussed in Subsection II.B.

3. Dewars and Cold Shield

a. Dewar Design

The helium Dewars used in this work were standard research Dewars models CLF-2 and CLF-3MD, made by Quantum Electronics Corporation, Houston, Texas. The working surface of the CLF-3MD Dewar was modified to make a cylindrical cavity projecting into the helium bath. Schematics of the Dewar working space for the two sensors are shown in Figures 6 and 7. Parts were aluminum or copper. No identifiable difference in cooling was noticed as long as the surfaces fit tightly.

The preamplifiers are mounted directly on the connector at the side of the Dewar. Twisted, number 35 manganin leads are used between the detector and the connector because of the low thermal-to-electrical conductivity ratio of manganin.

Crystalline quartz and polyethylene windows were used, however, polyethylene provided notably better transmission for the GaAs detector than the quartz. For the InSb, the difference was not significant. Additional tests demonstrated that Teflon would have made very good windows.

The filters were fitted tight mechanically, and a small amount of thermal grease was used to assure adequate thermal conductivity. It was important that the filters be well cooled and that no light leaks occur inside the inner cavity if the detectors were to operate at their maximum efficiency. The aluminum relay mirror was placed inside the cold shield so it could be used as a reflection filter, if necessary.

The inside of the outer aluminum cold shield had a specially prepared absorbing surface so that all radiation outside the acceptance cone was absorbed and not reflected onto the filters. The acceptance cone at the detector was defined by the hole in this shield. The absorbing surface was prepared in the manner described by Pipher and Couck.[6] This consisted mainly of Parsons Optical Black Undercoat and Flat Black made into a thick layer by dusting the tacky

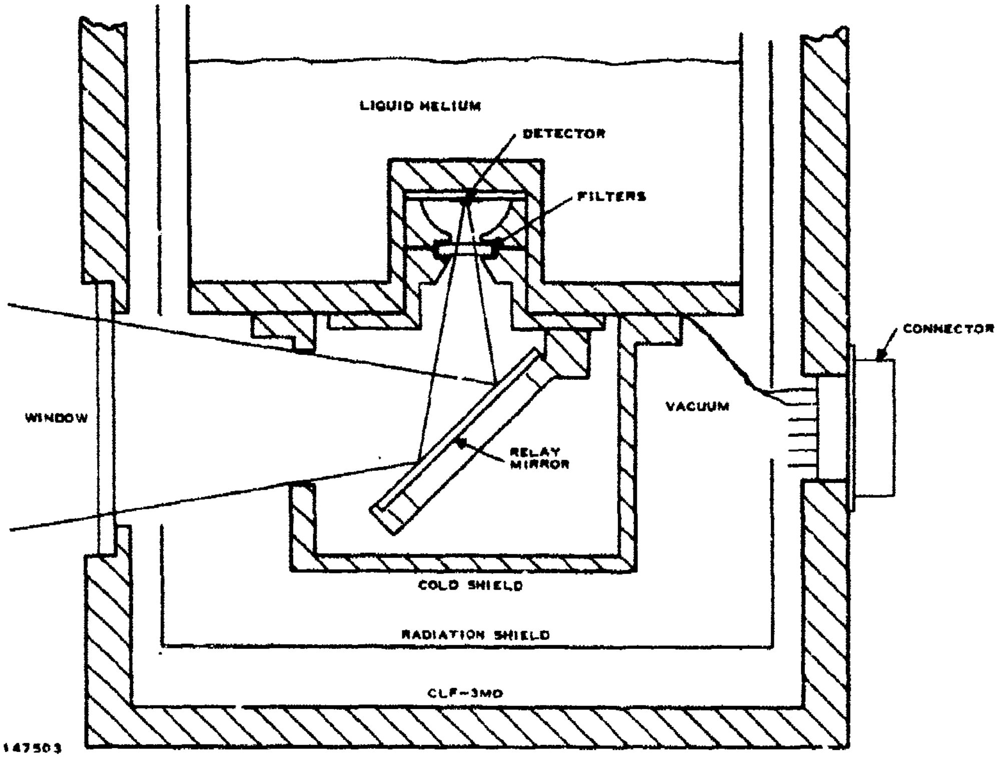

Figure 6. Indium Antimonide (InSb) Sensor Design

surface between applications with a hairy flock. The ½- to 1-mm thickness used in this work appeared to be sufficiently black for all wavelengths of interest.

b. Cold Shield Temperatures

The temperature of surfaces mounted on the Dewar cold plate can be estimated from a knowledge of the radiant energy reaching the cold shield and the rate at which this heat is conducted to the liquid helium. The important heat transfer features and the approximate temperatures that should be encountered can be determined with a plane geometry approximation shown in Figure 8. In this model,

ϵ_i = emissivity of surface i

α_i = absorptivity of surface i = ϵ_i

ζ_i = reflectivity of surface i = $1 - \epsilon_i$

A_o = outside area of cold shield

A_s = cross section of cold shield walls

A_c = cross section of contact with cold surface

L_s = length of cold shield

L_c = thickness of contact

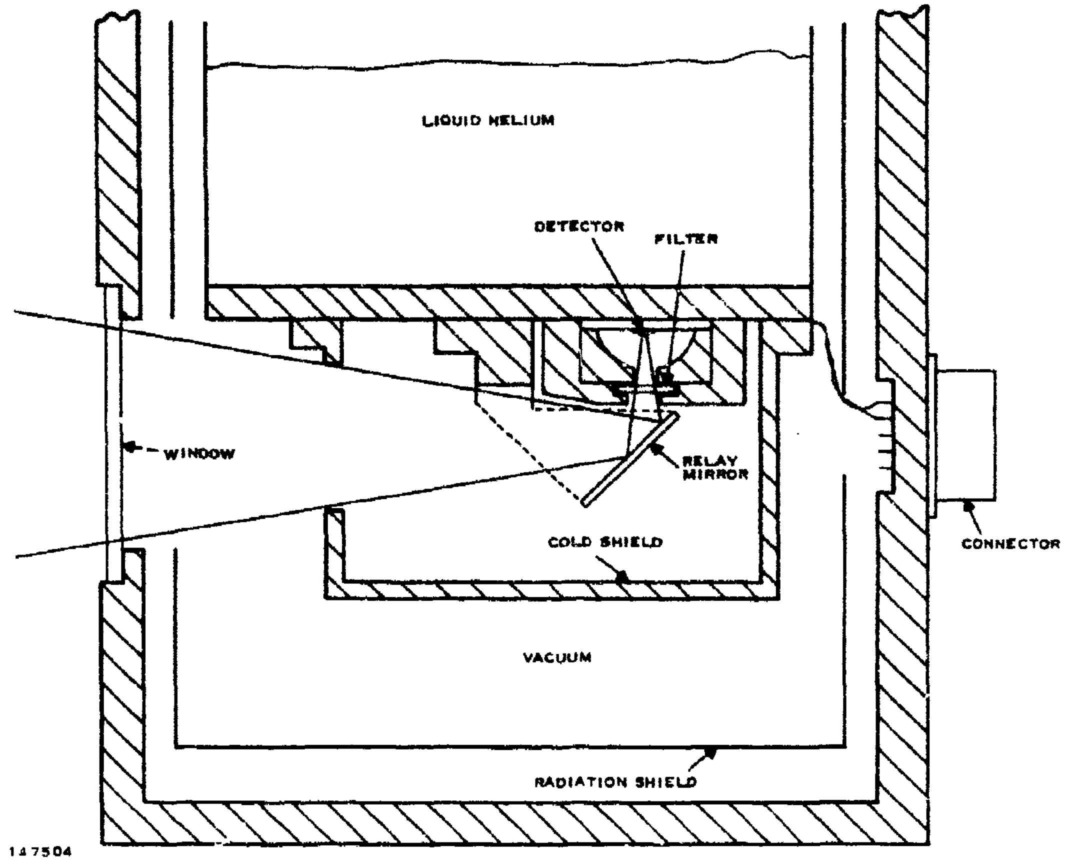

Figure 7. Gallium Arsenide (GaAs) Sensor Design

k_s = thermal conductivity of cold shield material

k_c = thermal conductivity of contact material.

The heat flow from the outside to the cold surface is given by the differences in heat radiated and absorbed by the surfaces 1, 2, and 3 and by conduction through the cold shield and its contact with the cold surface. The radiant transfer of heat is given by

$$q = \frac{A_o \, \sigma \, (T_1^4 - T_3^4)}{\frac{\zeta_1}{\epsilon_1} + 1 + \frac{\zeta_{2a}}{\epsilon_{2a}} + \frac{\zeta_{2b}}{\epsilon_{2b}} + 1 + \frac{\zeta_3}{\epsilon_3}} = \frac{A_o \, \sigma \, (T_1^4 - T_3^4)}{\frac{1}{\epsilon_1} + \frac{1}{\epsilon_{2a}} + \frac{1}{\epsilon_{2b}} + \frac{1}{\epsilon_3} - 2} \qquad (16)$$

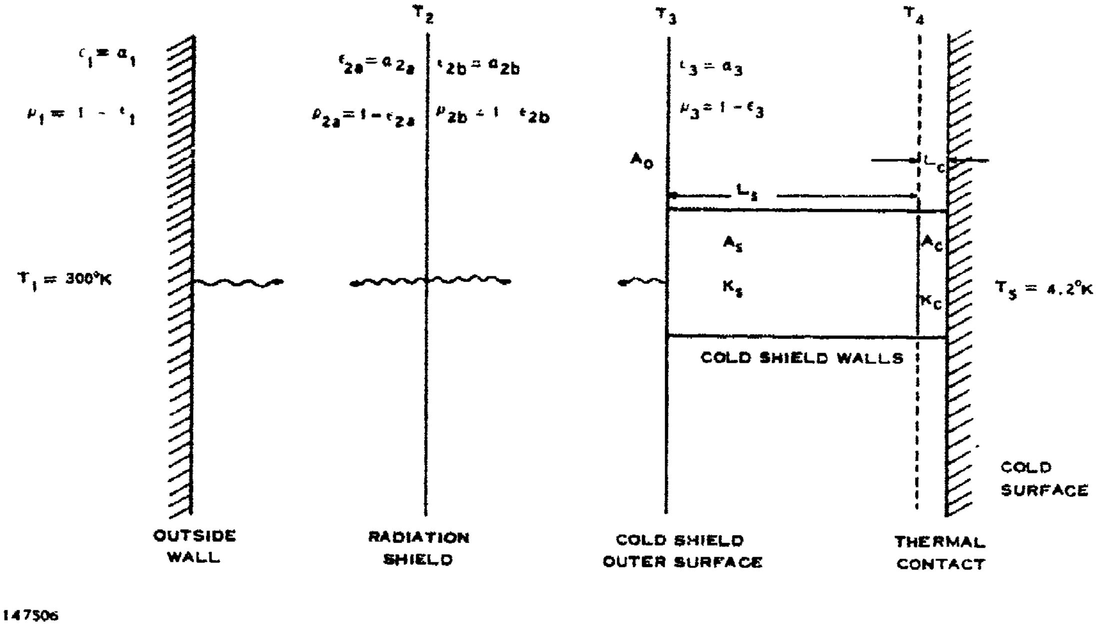

Figure 8. Heat Flow Model

where $\sigma = 5.67 \times 10^{-12}$ W/cm² $(°K)^4$. At equilibrium, this same amount of heat is conducted from surface 3 to 5:

$$q = \frac{k_s A_s}{L_s} (T_3 - T_4) = \frac{k_c A_c}{L_c} (T_4 - T_5) \tag{21}$$

In practice, the emissivities are all small and approximately equal so that

$$q \simeq \frac{A_0 \, \sigma \, (T_1^4 - T_3^4)}{4/\epsilon - 2} = \frac{k_s k_c}{k_s + k_c} (T_3 - T_5) \tag{22}$$

where $k_s = (k_s A_s)/L_s$ and $k_c = (k_c A_c)/L_c$. In properly functioning Dewars, T_3 will be much less than T_1 so that T_3 can be determined from

$$T_3 = T_5 + \frac{(k_s + k_c) \, \sigma \, A_0 \, T_1^4}{k_s k_c \, (4/\epsilon - 2)} \tag{23}$$

The heat absorbed by the liquid helium is given by Equation (22). The temperature of the outer cold shield, T_3, should not be much greater than 20°K. Except for radiation through the window, where surfaces 1, 2, and 3 do not exist, it will be much nearer to 4.2°K. Typical conditions might be represented by the following values:

$\epsilon = 0.02$ to 0.15
$A_o = 100$ to $135\ \text{cm}^2$
$A_s = 6$ to $9\ \text{cm}^2$
$A_c = 20$ to $40\ \text{cm}^2$
$L_s = 5.5$ to $10\ \text{cm}$
$L_c = 10^{-3}$ to $10^{-2}\ \text{cm}$
$k_s = 4$ to $30\ \text{W/cm}\ {}^\circ\text{K}$
$k_c = 5 \times 10^{-4}$ to $7.5 \times 10^{-3}\ \text{W/cm}\ {}^\circ\text{K}$
$T_1 = 300^\circ\text{K}$
$T_5 = 4.2^\circ\text{K}$.

Using worst case values, $k_s = 2.4\ \text{W}/^\circ\text{K}$, $k_c = 1.0\ \text{W}/^\circ\text{K}$

$$T_3 = 4.2 + \frac{3.4 \times 5.67 \times 10^{-12} \times 135 \times (300)^4}{2.4 \times 24.75} = 4.56^\circ\text{K}$$

and $q = 0.25$ W which represents, even in the worst case, about 0.3 liter per hour of liquid helium evaporation due to the cold shield on the bottom of the Dewar. Actual helium boiloff from all causes was about this rate.

The window will admit additional heat, most of which will be absorbed by the inside surface of the outer cold shield. This will not significantly alter temperatures of the filters and the inside cold shield if they are in close thermal contact with the Dewar cold surface. The outer edge of the outer cold shield was measured to be about 9°K.

c. Cold-Shield Requirements

Sensor noise, for a detector that is adequately cold-stopped, will arise either from internal detector noise, or in the theoretical limit from photon fluctuations in the signal. For this condition to be met, the cold shield must be maintained at a sufficiently low temperature that the statistical photon noise from the detector surroundings is small compared to the signal statistical noise or the detector noise, whichever is larger. The detector noise is limiting in this case and the noise equivalent power (NEP) is less than $1 \times 10^{-12}\ \text{W/Hz}^{1/2}$. Detectors may be improved, so it is important that noise from other sources be kept well below this value.

The NEP due to radiation from the cold shield used in this system can be calculated in a straightforward manner. However, the usual blackbody approximations cannot be applied at these wavelengths and temperatures. For instance, the peak energy emission for a 10°K cold shield is at a wavelength of 0.29 mm.

The power radiated into a hemisphere per unit wavelength is

$$W_\lambda = \frac{2\pi c^2 h}{\lambda^5} \; \frac{1}{e^x - 1} \tag{24}$$

where x = hc/λkT. The number of photons/cm² s per unit wavelength is

$$n_\lambda = \frac{2\pi c}{\lambda^4} \frac{1}{e^x - 1} \tag{25}$$

and the mean square fluctuation in the number of photons/cm² s in the interval Δλ is given by

$$\overline{\Delta n^2} = \frac{2\pi c \Delta\lambda}{\lambda^4} \frac{e^x}{(e^x - 1)^2} \tag{26}$$

This is the statistical fluctuation in numbers of photons emitted and absorbed on all surfaces inside a uniform temperature cold shield, including the detector of area A. Therefore the mean square fluctuation in number of photons/s in an area of the size of the detector is $\overline{\Delta n^2} A$. The rms fluctuation in the electrical bandwidth, Δf, for a photoconductive detector of quantum efficiency Q is

$$\sqrt{4\Delta f \overline{\Delta n^2} AQ} \tag{27}$$

A noise equivalent power (NEP) can be calculated as the signal power in a band centered at λ_s, which would produce the same fluctuation as the photons from the cold shield. Then

$$\mathrm{NEP} = \frac{hc}{\lambda_s} \sqrt{\frac{4\Delta f \overline{\Delta n^2} A}{Q}} \tag{28}$$

To calculate the mean square fluctuation in number of photons on the detector from the cold shield it is necessary to integrate the product of Equation (26) and the unfiltered detector response over all wavelengths. To simplify the procedure, an equivalent square wave response is substituted for the true response so that integration can be performed between two wavelengths λ_1 and λ_2.

$$\overline{\Delta n^2} = 2\pi c \int_{\lambda_1}^{\lambda_2} \frac{1}{\lambda^4} \frac{e^x}{(e^x - 1)^2} \, d\lambda \tag{29}$$

$$\overline{\Delta n^2} = 2\pi c \left(\frac{kT}{hc}\right)^3 \sum_{n=1}^{\infty} \left(x^2 + \frac{2x}{n} + \frac{2}{n^2}\right)\Bigg|_{x_1}^{x_2} \tag{30}$$

The series of Equation (30) converges rapidly for Tλ ⩽ 1 cm °K. For larger values, Equation (29) can be evaluated numerically, or as in the case of the InSb bolometer (which has response to very long wavelengths such that $\lambda T \gg 1$), the sum for $x_2 \to 0$ becomes $\pi^2/3$ and Equation (30) can be evaluated with only a few terms of the series for the short wavelength cut-on λ_1. Two detector response bands of interest are 0.25 to 0.30 mm, representative of unfiltered GaAs, and 0.6 to ∞, representative of InSb. The mean square fluctuations in the number of photons/s on the detector from the cold shield in these bands is shown in Figure 9. Also indicated is the mean square fluctuation from 300°K signals through the filter bandpass.

The noise equivalent power due to statistical fluctuation in the signal will depend on the spectral character of the sensor response and on the sensor geometry. This is the lower limit to NEP for this particular system looking at 300°K objects and can be approximated by assuming an equivalent square-wave spectral response for the detectors.

The power emitted by a 300°K graybody (emissivity ϵ) in the wavelength interval λ_1 to λ_2 is

$$P = \int_{\lambda_1}^{\lambda_2} \epsilon W_\lambda d\lambda = \int_{\lambda_1}^{\lambda_2} \epsilon \frac{2\pi kcTd\lambda}{\lambda^4} \cong \epsilon \times 2.6 \times 10^{-10} \left(\frac{1}{\lambda_1^3} - \frac{1}{\lambda_2^3}\right) \qquad (31)$$

for

$$\frac{hc}{\lambda kT} \ll 1$$

For the two detectors used in this work,

GaAs

$\lambda_1 = 2.7 \times 10^{-2}$ cm

$\lambda_2 = 2.9 \times 10^{-2}$ cm

$P = \epsilon 2.39 \times 10^{-6}$ W/cm^2

InSb

$\lambda_1 = 5.90 \times 10^{-2}$ cm

$\lambda_2 = \infty$

$P = \epsilon 1.26 \times 10^{-6}$ W/cm^2

The emitting area of a target for each resolution element will be approximately

$$\pi \left(\frac{\alpha R}{2}\right)^2$$

where α is the angular resolution and R is the distance of the target from the collecting aperture. The radiant intensity from one resolution element of the target is then

$$J = \frac{P\alpha^2 R^2}{4} \text{ W/sr}$$

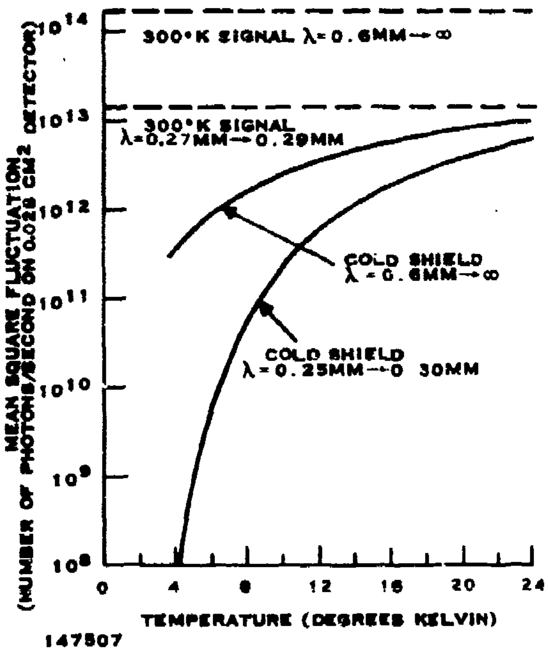

Figure 9. Statistical Photon Fluctuation from Cold Shields

The fraction of radiation reaching the collecting aperture is determined from the solid angle

$$\Omega = \pi \sin^2 \theta/2 = \pi \sin^2(\text{arc tan } D/2R) \left(\approx \frac{\pi D^2}{4R^2} \text{ for small } \theta\right)$$

where θ is the angle subtended by the aperture of diameter D at the target. For an optical efficiency η, the radiant power at the detector will be

$$\begin{aligned} P_d &= \frac{\pi \eta P \alpha^2 R^2}{4} \sin^2 (\text{arc tan } D/2R) \\ &\approx \frac{\pi \eta P \alpha^2 D^2}{16} \end{aligned} \tag{32}$$

For this system, $\alpha^2 D^2/16 \cong 2.25 \times 10^{-4}$ cm² for $\alpha \cong 2 \times 10^{-3}$ radian. Therefore, for GaAs,

$$P_d = \epsilon\eta \; 1.69 \times 10^{-9} \text{ W}$$

and for InSb, where $\alpha \cong 4 \times 10^{-3}$ rad:

$$P_d = \epsilon\eta \; 3.55 \times 10^{-9} \text{ W}$$

The mean square fluctuation in numbers of photons reaching the detector in this system is

$$\overline{\Delta n^2} = \frac{P_d}{h\nu} \frac{e^x}{e^x - 1} \cong \frac{P_d}{h\nu} \left(\tfrac{1}{2} + \frac{1}{x}\right) \tag{33}$$

For GaAs

$h\nu = 7.0 \times 10^{-22}$ Ws/photon

$x = 0.168$

$\overline{\Delta n^2} = \epsilon\eta \; 1.6 \times 10^{13} \text{ s}^{-1}$

For InSb

$h\nu = 2.8 \times 10^{-22}$ Ws/photon

$x = 0.069$

$\overline{\Delta n^2} = \epsilon\eta \; 1.9 \times 10^{14} \text{ s}^{-1}$

These are the values indicated in Figure 9 for $\epsilon = \eta = 1$.

The NEP from the signal energy alone is

$$NEP_s = \frac{h\nu}{\sqrt{Q}} \sqrt{4 \Delta f \overline{\Delta n^2}} \tag{34}$$

where Q is the quantum efficiency

Thus, for

GaAs

$$\mathrm{NEP_s} = \sqrt{\frac{\epsilon\eta}{Q}}\, 5.5 \times 10^{-15}\ \mathrm{W/Hz^{1/2}}$$

InSb

$$\mathrm{NEP_s} = \sqrt{\frac{\epsilon\eta}{Q}}\, 7.8 \times 10^{-15}\ \mathrm{W/Hz^{1/2}}$$

This is, then, the theoretical limit to NEP for this system looking at 300°K objects. If photon noise from the cold shield is comparable to this, it will be well below detector noise. It can be seen from Figure 9 that for cold shield temperatures less than about 25°K, the noise contributed by the shield is less than that due to statistical fluctuations of the incoming signal. Both contribute significantly less noise than the measured NEP of the detectors.

4. Images Through Clothing

Images are made from differences in power reaching the detector as the scanning optics moves the scene across the detector. At long wavelengths, the power emitted by a graybody depends linearly on the temperature so that as the target area passes from an object at temperature T_1 to one at T_2 the power change on the detector is

$$\Delta P = P_d \frac{T_1}{300} - P_d \frac{T_2}{300} = \frac{P_d}{300}\, \Delta T$$

since P_d was calculated for a 300°K graybody. For the case of a metallic object concealed beneath a partially absorbing layer of cloth, the contrast is between the power from the person and his clothing and the power reflected from the surroundings after passing twice through the covering material. Assuming the clothing and body to have an emissivity of one at these wavelengths and the metal to be a perfect reflector, the power difference will be

$$\Delta P = \frac{P_d}{300} \left\{ T_b \tau_c + T_c(1 - \tau_c) - [T_r \tau_s + T_s(1 - \tau_s)]\, \tau_s - T_s(1 - \tau_s) \right\} \qquad (35)$$

where

T_b = Body temperature

T_c = Average clothing temperature

T_s = Temperature of cover over the metal (which may equal T_c if the metal has reached equilibrium)

T_r = Temperature of the room or outdoor surroundings

τ_c = Clothing transmission

τ_s = Transmission of cover over the metal

For instance, if the metal is carried next to the body and is at body temperature, so that $\tau_s = \tau_c = \tau$ and $T_s = T_c$, then

$$\Delta P = \frac{P_d}{300}\,\tau\left\{T_b - T_r\tau - T_c(1 - \tau)\right\} \tag{36}$$

If the cloth assumes an average temperature between T_b and T_r,

$$\Delta P = \frac{P_d}{300}\,\tau\,\frac{(1 + \tau)}{2}\,(T_b - T_r) \tag{37}$$

The coefficient $\tau(1 + \tau)/2$ is shown in Figure 10. For good transmissivity, this does not differ greatly from the simple assumption that the differential power reaching the detector as it scans over the concealed metal is directly proportional to τ. In fact, some of the numerous approximations that have been made in arriving at Equation (37) will result in a signal overestimate and some in an underestimate. For instance, if temperature of the clothing over the metal is less than clothing not over metal, that is, $T_s < T_c$, then the signal will be greater than indicated by Equation (37). Also, when $\tau_s > \tau_c$, which will often be the case, the signal should be improved. Therefore, the difference in power reaching the detector in the two circumstances will be assumed to be

$$\Delta P \simeq \frac{P_d}{300}\,\tau(T_b - T_r) \tag{38}$$

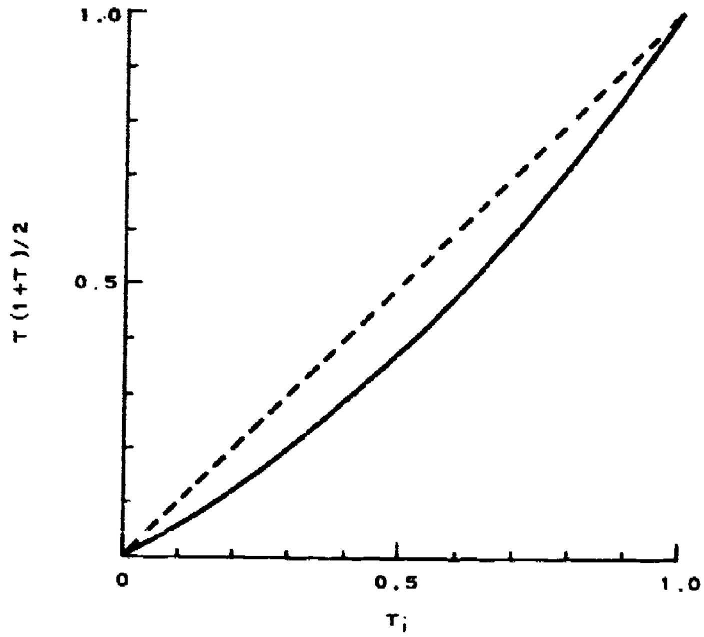

162363

Figure 10. Coefficient $\tau(1 + \tau)/2$

The temperature difference is typically 15°C, so that $\Delta P \cong P_d \tau/20 = \epsilon\eta\tau \; 2 \times 10^{-10}$ W for the InSb detector. If the NEP of the system is 10^{-13} W/Hz$^{1/2}$, then in a 15-kHz bandwidth the signal to noise is

$$\Delta P/NEP \cong 14\ \epsilon\eta\tau$$

5 Filters

Response curves for the GaAs and InSb detectors used in the study are given in Figure 11 along with the 300°K blackbody radiation curve. The filters were black polyethylene and quartz. These curves are plotted as a function of wavelength for convenience. However, the response and radiation intensity are for unit wave number. On a scale above these response curves is plotted the atmospheric absorption coefficient as measured by Furashov.[7]

Without filters or atmospheric attenuation, the signal from the detector when looking at a 300°K blackbody would be proportional to the product of the spectral radiant emittance and the detector response. When filters are added, it is necessary to convolve the filter characteristics with those of the detector and blackbody radiant emittance.

One of the most common filters employed in the submillimeter portion of the spectrum is black polyethylene which consists of carbon powder embedded in polyethylene sheet. The transmittance curve in Figure 12 is taken from the measurements given by Moller.[8] While this material is effective in eliminating visible radiation, it transmits too much of the infrared to be used by itself as a long wavelength pass filter for GaAs in the submillimeter.

The use of restrahlen crystal powder suspended in polyethylene has been shown to provide high absorption in the far infrared and good transmission at submillimeter wavelengths.[8,9] Restrahlen filters were made at Texas Instruments in order to obtain the sharpest cutoff possible for wavelengths shorter than about 0.28 mm. Two slightly different compositions were used.

TI-1 Polyethylene, 2.0 parts; KI, 0.4 parts; NaCl, 0.2 parts; TlI, 0.5 parts

TI-2 Polyethylene, 2.0 parts; KI, 0.4 parts; NaCl, 0.2 parts; KRS, 6 (44-percent TlBr, 56 percent TlCl), 0.5 parts.

Filter characteristics for these two compositions are plotted in Figure 9, based on measurements made by Professor Hiroshi Yoshinaga. Many other restrahlen crystal power combinations are possible but none have absorption bands at wavelengths longer than 0.2 mm.

For long-wavelength pass filters with a cutoff wavelength longer than 0.2 mm, it is necessary to use metal mesh as either a transmission or as a reflection filter. Reflection filters are preferred because the reflected energy at long wavelengths is greater and the rejection of short wavelengths, by scattering or transmission, is better. Measured characteristics of a variety of reflection filters are given by Mitsuishi, and others,[10] and their use is described by Moller.[11] The measured reflection characteristics of 100-mesh (wires per inch) metal mesh filter are plotted in Figure 12. Other mesh could be chosen to select a different portion of the submillimeter spectrum.

Reflection filters were not used in the GaAs Dewar, however the relay mirror surface was roughened to scatter short-wavelength radiation. The detector response curves of Figure 11 were made with filters consisting of black polyethylene and crystal quartz. When the TI-2

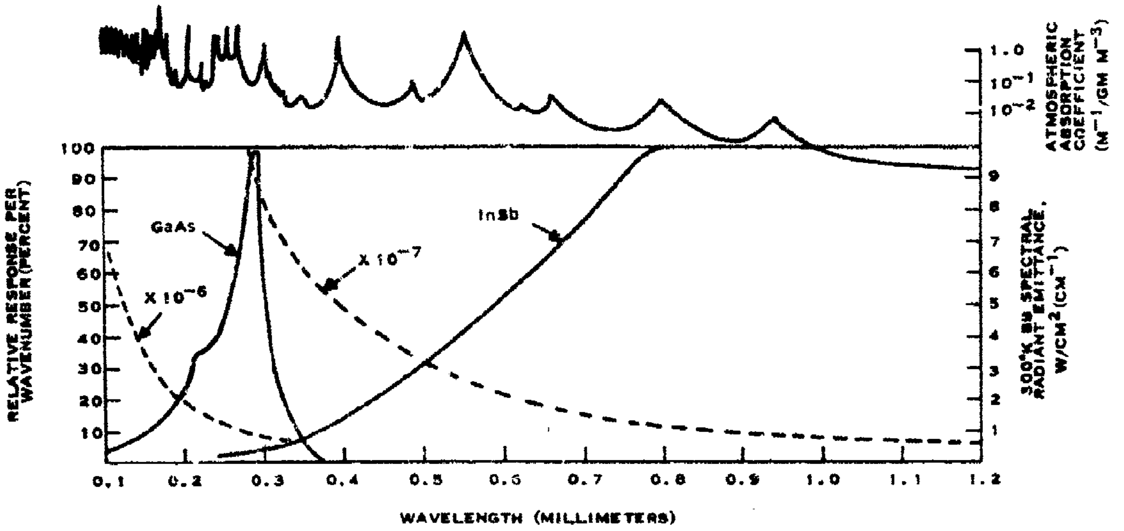

147508

Figure 11. Unfiltered Detector Response

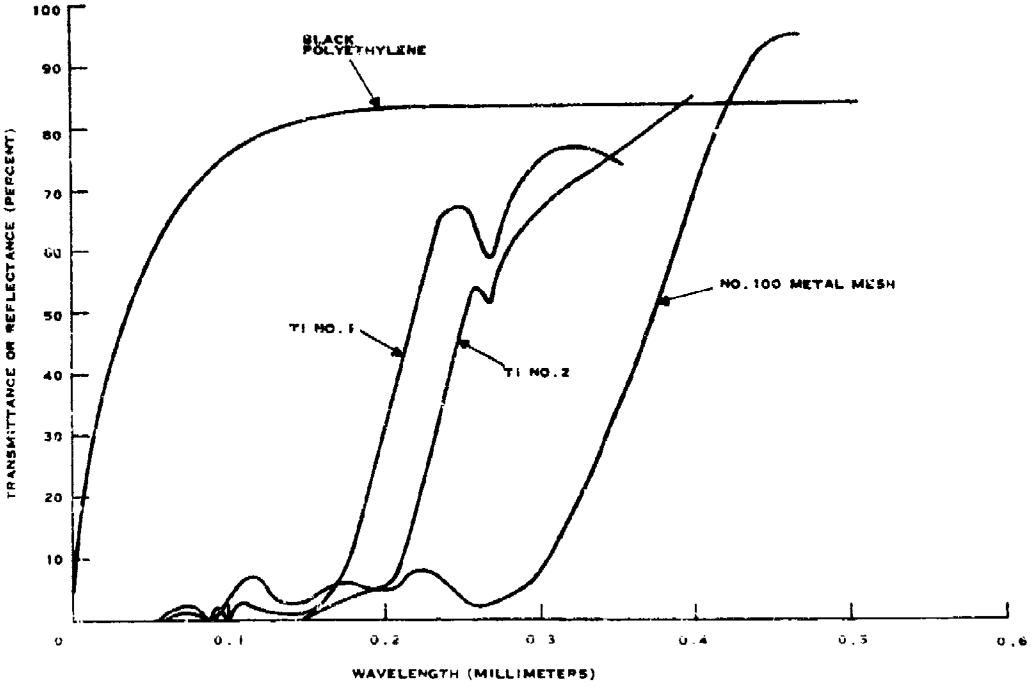

Figure 12. Spectral Filter Transmittance

restrahlen filter was added to the GaAs sensor, the response curve was changed as shown in Figure 13. This was the filter combination used in the system except that the crystal quartz filters were sometimes removed with no apparent change in detection performance.

To determine the spectral response of these two filtered sensors to a 300°K blackbody, the response curves of InSb and GaAs from Figure 11 and the filters from Figure 12 must be weighted with the blackbody emission curve of Figure 11. This renormalized response is shown in Figure 14. This should be a good approximation to the spectral response of the present system to radiation emitted by the target scene. However, in the case of InSb, the spectral response curve may be shifted to shorter wavelengths due to the mismatch of the detector size to the diffraction blur circle for longer wavelengths.

6. Pressure-Induced Noise in the InSb Detector

Low frequency noise ($\overset{\cong}{<}$ 5 Hz) with a variable amplitude that is sometimes as large as a microvolt has been directly correlated with changes in gas pressure above the liquid helium bath. Since signals are typically a few tenths of a microvolt, this noise source causes image streaking and can even saturate the screen. Images can be obtained by passing the signal through a high-pass filter that cuts off at 5 Hz. However, there is probably still some noise from this source and some loss of signal. To verify the mechanism responsible for these fluctuations, an estimate was made of the signal to be expected within the system bandpass ($\cong$0.3 to 3,000 Hz) from a change in pressure above the helium bath.

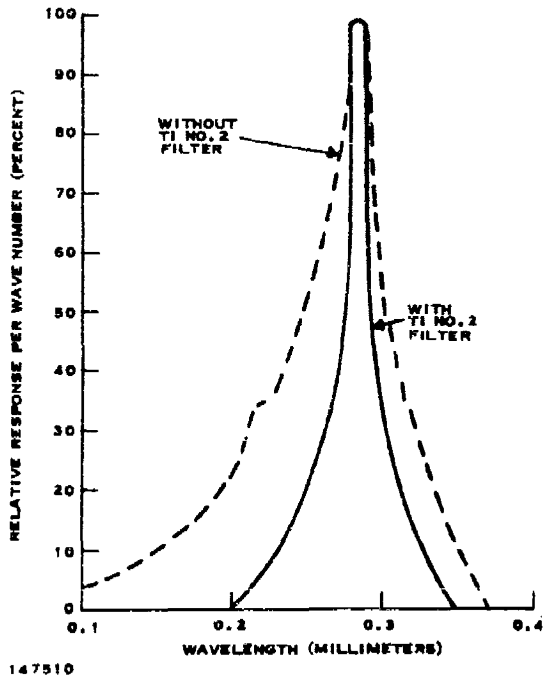

Figure 13. Gallium Arsenide Filtered Detector Response

a. Detector Temperature

For carrier concentrations in these InSb detectors, the resistance at temperatures near 4.2°K is approximately proportional to temperature. Therefore, for small ΔT,

$$\Delta R \cong R\,\Delta T/T$$

For a bias current I, the signal across the detector due to a temperature change ΔT will be

$$\Delta N = I\,\Delta R = I\,R\,\Delta T/T \qquad (39)$$

For instance, under present operating conditions,

$I = 7 \times 10^{-5}$ amperes

$R = 500$ ohms

$T = 4.2°K.$

so that

$$\Delta N \cong 0.83 \times 10^{-2}\ \Delta T \text{ volts}$$

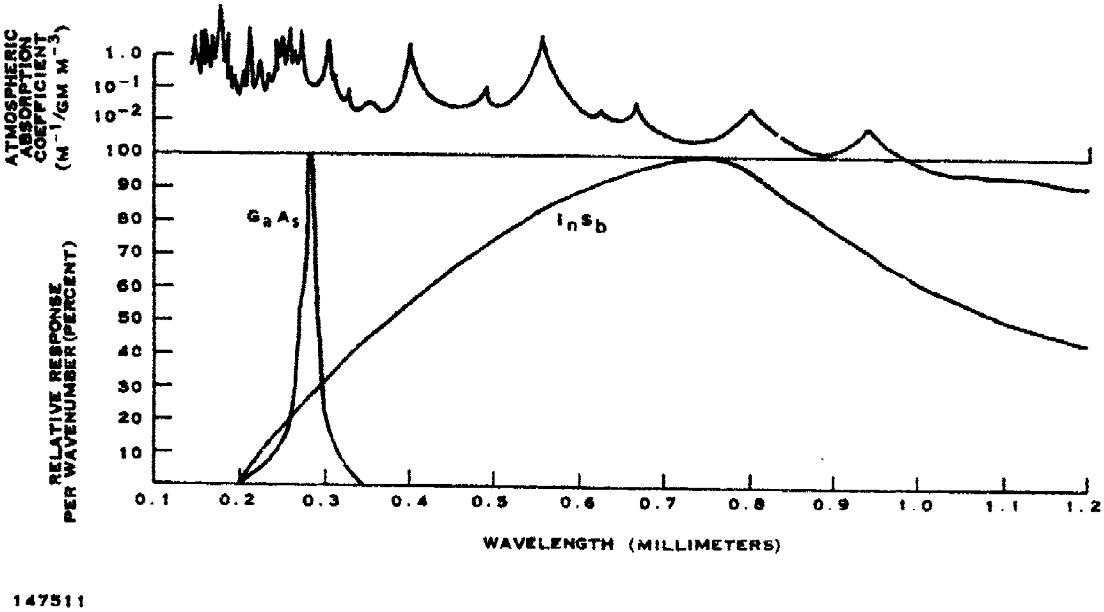

Figure 14. Spectral Response of Filtered Detectors to 300°K Blackbody Radiation

Therefore, temperature variations of 10^{-4}°K would produce almost 1 microvolt of noise.

b. Liquid Helium Thermal Inertia

The vaporization curve slope for liquid helium near 4.2°K and one atmosphere pressure is

$$\Delta T/\Delta P \cong 1.4 \times 10^{-3}\,{}^{\circ}\mathrm{K/torr} \tag{40}$$

If the total heat load on the liquid helium bath is H cal/s, then the temperature will change to the new equilibrium temperature at the rate of

$$S = H/C\rho V\ {}^{\circ}\mathrm{K/s} \tag{41}$$

where C = 1.0 cal/g°K is the heat capacity, $\rho = 0.1251$ g/cm³ is the density and V the volume of liquid helium in the Dewar. If the low-frequency cutoff of the system is f_L, the largest temperature change of the liquid helium that could be observed through the system electronics is

$$\Delta T_{max} = \frac{H}{C\rho V f_L}\ {}^{\circ}\mathrm{K} \tag{42}$$

This is equivalent to saying that the thermal inertia of the helium bath will allow only changes of ΔT_{max} or smaller within the time interval $1/f_L$. More noise can be expected from this source with smaller volumes and larger heat loads. A typical heat load of $H \cong 0.25$ W $\cong 0.06$ cal/s with 0.25 liter of helium and $f_L = 0.3$ Hz would result in an observable change for $\Delta T_{max} \cong 6.4 \times 10^{-3}$°K which represents about a 4-torr pressure change.

Since the helium is boiling, almost all the heat load is going into heat of vaporization (6 cal/g). When the boiling point is changed slightly by changing the vapor pressure, the entire liquid temperature will change at about the rate S. However, the temperature at the liquid-container interface will probably change faster and this new temperature will be distributed rapidly throughout the liquid by convective processes. Although it is the temperature at the walls rather than that of the entire liquid that is important, an estimate of the rate of change of inside-wall temperature caused by a pressure change is not as easy to make. This would depend upon such things as the shape of the container and the effectiveness of detailed convective processes at the container wall. Therefore estimates of the thermal inertia of the liquid helium derived here are conservative.

e. Cold Wall Thermal Inertia

The problem is to find what fraction of the temperature change occurring on the inside wall of the Dewar is transmitted to the detector within the system response time.

The solution for the temperature change on one side of a slab of thickness ℓ, and thermal diffusivity κ due to a temperature change ΔT_o on the other side is[12]

$$\Delta T_{(\ell,t)} = \Delta T_o \left(1 - \frac{4}{\pi} \sum_{0}^{\infty} \frac{(-1)^n}{2n+1} e^{-\frac{(2n+1)^2 \pi^2}{4} \frac{\kappa t}{\ell^2}} \right)$$

This form coverges rapidly for values of $\kappa t/\ell^2 > 0.1$, but after a sufficiently long time, $t \gg \ell^2/\kappa$, the change in temperature is transmitted almost undiminished through the slab. Thermal diffusivity is given by

$$\kappa = \frac{K}{\rho C}$$

where K is the thermal conductivity, ρ the density and C the heat capacity of the slab. The InSb detector is mounted on a thin sapphire sheet which is attached to a copper disk. This copper disk is bolted to the Dewar copper work surface. The sapphire sheet and copper impurities will be ignored and only the properties of pure copper will be used for the slab.

T	4.2°K	300°K
ρ	8.9 g/cm^3	8.9 g/cm^3
K	28.2 cal/s cm°C	0.95 cal/s cm°C
C	2.5×10^{-5} cal/g°C	9.2×10^{-2} cal/g°C
$\kappa = K/\rho C$	1.27×10^{4} cm^2/s	1.16 cm^2/s

These figures show that for time intervals and slab thicknesses for which there is great attenuation at room temperature, there will be no significant attenuation at 4.2°K. In this case, $\ell \cong 1$ cm so that any changes in temperature on the helium side of the work surface will be transmitted almost unattenuated to the detector within the system response time of about 3×10^{-4} seconds. Therefore, the thermal inertia of the cold wall and detector mounts can be neglected.

Equations (39) and (40) can be combined to give the noise voltage associated with pressure changes above the liquid helium

$$\Delta N = 1.4 \times 10^{-3}\ \Delta P\ IR/T = 1.16 \times 10^{-5}\ \text{volts/torr} \tag{43}$$

with the restriction imposed by Equation (42) that the maximum voltage that could be detected at a frequency f would be

$$\Delta N_{max} = \frac{IRH}{TC\rho Vf} = 6.63 \times 10^{-2}\ \frac{H}{Vf}\ \text{volts}$$

For instance, if $H \cong 0.06$ cal/s, $V = 250$ cm^3 and $f = 1$ Hz

$$\Delta N \leqslant 1.6 \times 10^{-5}\ \text{volts}$$

Equation (43) therefore shows that pressure changes of only 0.1 torr will add noise at low frequencies.

B. Amplifiers

The overall bias and preamplifier function plan for both detector types (photoresistive GaAs and InSb) is shown schematically in Figure 15A. The preamplifier and bias functions are accomplished in an input circuit termed a "preamplifier" as indicated in Figures 15B and C. The balance of the gain necessary to raise signal and noise levels to that required at the scanner electronics input is accommodated in a circuit called an auxiliary amplifier. The auxiliary amplifier also provides step variable gain for two bandwidths (3 and 30 kHz) for the two detectors, continuously variable gain adjust, and a step down (±30 to ±15 V) voltage regulator to bridge from scanner electronics mains to those required for the pre- and auxiliary amplifiers.

Two preamplifiers are required because of the considerable differences in the resistance levels and output noise voltages exhibited by the two detectors. The GaAs detector employed exhibited resistances around 2 MΩ and output noise voltages of $\cong 200$ nV/Hz$^{1/2}$ when operating at optimum bias of $\cong 0.15$ V, at liquid helium temperature. The typical InSb detector, in contrast, had a resistance of a few hundred ohms and output noise voltages of 0.5 nV/Hz$^{1/2}$ at 10 kHz at optimum operational bias and temperature.

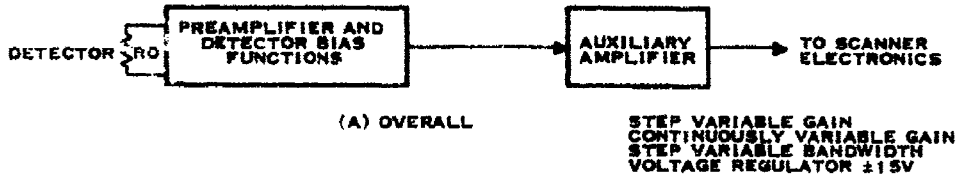

(A) OVERALL

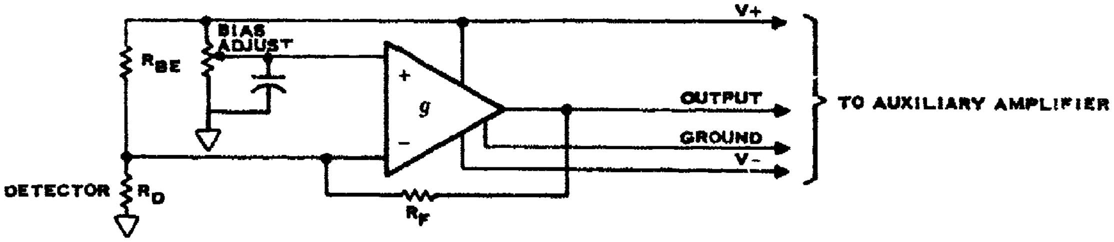

(B) Ga As PREAMPLIFIER

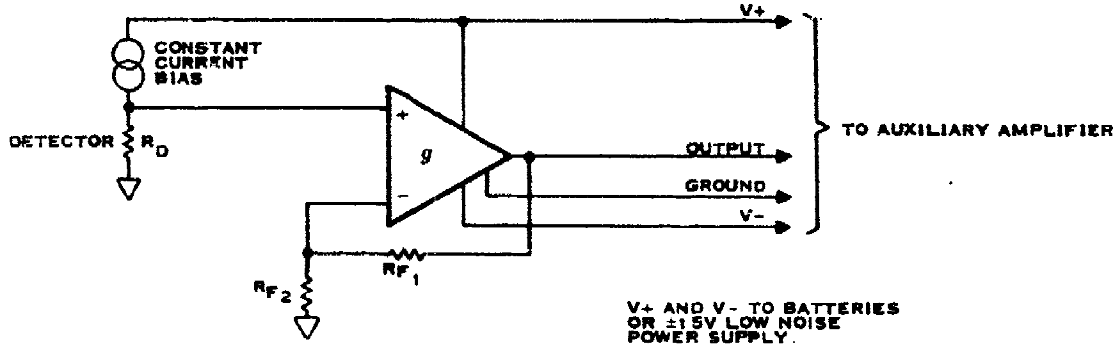

(C) $I_n S_b$ PREAMPLIFIER

147513

Figure 15. Amplifier Plan

1. Gallium Arsenide Preamplifier

This preamplifier shown schematically in Figure 16 is basically a direct coupled inverting amplifier of conventional design fed back in a transimpedance mode. The input stage, Q_1 and Q_2, uses a matched JFET pair with a constant-current emitter source, Q_7. Only the inverting input is made available externally. The positive input, gate of Q_2, is used internally to set detector bias. The second stage, Q_3 and Q_4, is also a differential stage employing bipolar transistors with a constant current source, Q_8. The second stage has a single-ended output and drives a complementary bipolar transistor output stage push-pull pair, Q_5 and Q_6.

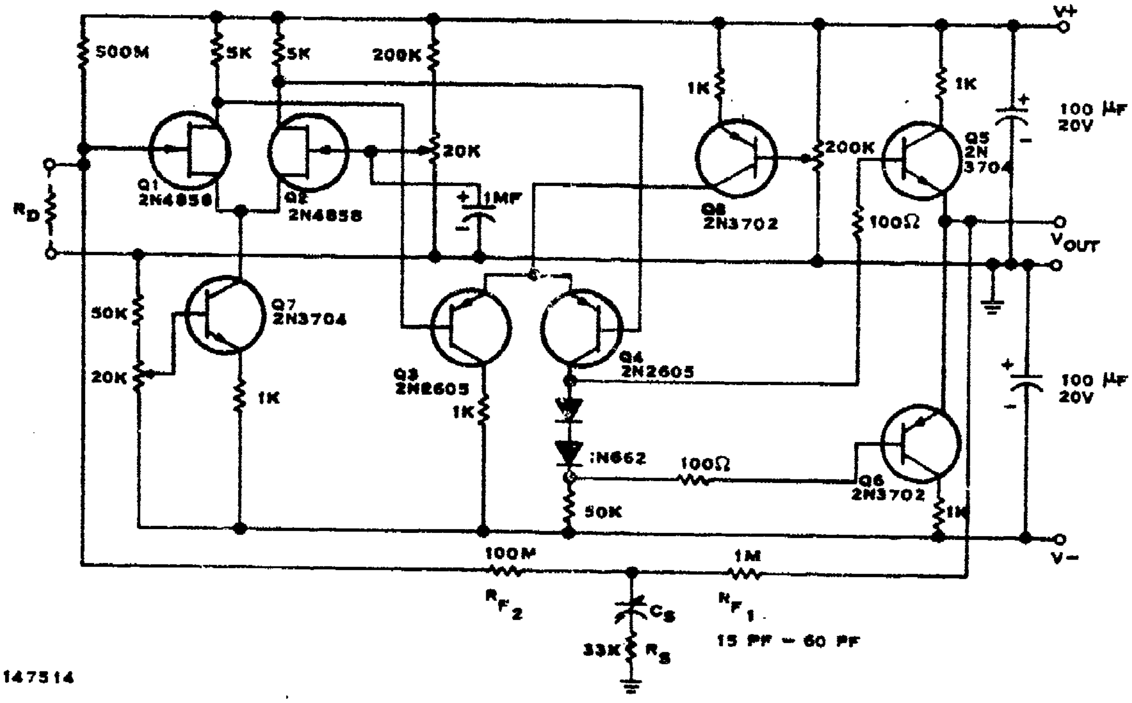

Figure 16. Gallium Arsenide Preamplifier Schematic

Operating characteristics and parameters for this preamplifier are given in Table I, where

v_{nA} = short circuit equivalent input amplifier noise voltage

i_{nA} = open circuit equivalent input amplifier noise current

R_{in} with a remark of "passive" means input resistance with Q_1 not in the circuit or with the circuit deactivated.

a. Detector Bias

The transimpedance mode preamplifier was selected for use with the GaAs detector because of the biasing and frequency response characteristics of this type amplifier. Consider detector biasing. Ideally, the transimpedance amplifier has the property that it repeats at its inverting (–) input whatever voltage is applied to its noninverting (+) input ± the amplifier input offset voltage (V_{IO}) as long as the amplifier output does not saturate. Near-optimum detector operation is achieved with constant dc voltage bias and this amplifier can achieve such operation over fairly large ranges of detector impedance, depending on circuit design.

The dc bias voltage wanted is set up at the (+) input (Q_2 gate of Figure 16) with the resistor network provided and the necessary dc voltage is repeated at the detector input [(–) input, Q_1 gate]. The 1-mF capacitor bypassing the gate of Q_2 to ground is included for noise minimization.

TABLE I. GaAs PREAMPLIFIER CHARACTERISTICS AND PARAMETERS

Characteristic/Parameter	Value	Remarks
Open Loop Gain (g)	5.6 k (v/v)	
Open Loop Frequency Response		
Low (f_l)	dc (Hz)	
High (f_h)	45 k (Hz)	$R_G = 10\Omega$
Closed Loop Gain (g_{cl})	$\frac{R_f}{R_D} \cong \frac{100\ M\Omega}{R_D}\ \frac{v}{v}$	
Closed Loop Frequency Response		
Low (f_l)	dc Hz	
High (f_h)	>50 k Hz	$R_G = 500\Omega$
Noise Characteristic		
V_{nA} (1 kHz)	3.4 nV/Hz$^{1/2}$	$R_G = 10\Omega$
(10 Hz)	13 nV/Hz$^{1/2}$	$R_G = 10\Omega$
i_{nA} (1 kHz)	$<10^{-3}$ pA/Hz$^{1/2}$ (C)	
Input Parameters	83.3 MΩ	Passive
R_{in}	~2.10^4 Ω (C)	Active
C_{in}	~60 pf (C)	
Output Parameters		
R_o	<26 Ω (C)	
Maximum Output Swing	> ±13 V(M)	
Voltage Supply		
V^+	15 V	
V^-	15 V	
Quiescent Current Drain		
I^+	2.85 mA (M)	
I^-	2.86 mA (M)	
Power	<90 mW	

NOTE:
For I drain indicate C or E for calculated or estimated, or M for measured.

The GaAs detector used exhibited a resistance of ≅2 MΩ, and an optimum dc bias range of 0.13 to 0.16 V. Detector resistance varied considerably (> ±20 percent) with background conditions which would cause a variation of $\gtrsim$±20 percent in the detector voltage responsivity and, thus, preamplifer output if a voltage mode amplifier had been employed. However, the transimpedance mode preamplifier responds only to the detector current responsivity which should remain constant with such fluctuations as long as detector voltage bias remains constant.

Detector bias was set at 0.14 V, which is in the optimum voltage range. The GaAs preamplifier employs an external bias source in addition to feedback bias. This enables the amplifier to bias a somewhat wider range of detector resistance than with only feedback bias. External bias is provided with the 500-MΩ resistor connected to the Q_1 gate. At 0.14 V bias, V_B, the detector resistance, R_D, range covered is $1\ \mathrm{M\Omega} \leqslant R_D \leqslant \infty$. For lower V_B, the range would extend to lower R_D and vice versa.

b. Frequency Response

Unloaded detector frequency response (where the detector load resistor $R_L \gg R_D$) is primarily limited by the detector-Dewar resistance-capacitance (RC) time constant. Voltage amplifier input capacity, interconnecting cable capacity, and so forth, add to this time constant and reduce detector-preamplifier frequency response. In a scanner, a flat frequency response over the spectrum of interest is necessary. The transimpedance (XZ) amplifier provides a means of accomplishing this end without frequency boost circuits or without passively loading the detector, and, thus, without the possibility of spoiling detector signal-to-noise performance. The XZ amplifier extends frequency response by loading the detector actively and if amplifier noise is sufficiently low the loading does not spoil detector signal-to-noise performance. A simple example illustrates this result. In the laboratory, a moderately high input-impedance voltage amplifier ($R_{in} \cong 67\ \mathrm{M\Omega}$, $C_{in} \cong 30$ pF), external bias box, cables, and so forth, were used to determine detector D*, voltage responsivity, impedance, and optimum bias. In this system frequency response was determined to be 500 Hz. With detector impedance at ≅2 MΩ, this response frequency indicates a system distributed capacity of 150 pF. To extend the frequency response to the required 30 kHz would necessitate that the distributed capacity be reduced to ≅2.5 pF, a near impossible feat. However, a preamplifier that reduced the input resistance to $\cong 1.7 \times 10^4$ with the same capacity, or a somewhat higher value with $C_{in} < 150$ pF, could accomplish the same response capabiltity. The GaAs preamplifier does the latter, having an $R_{in} \cong 20\ \mathrm{k\Omega}$ and a $C_{in} \cong 60$ pF, Table I. Allowing 10 pF for detector-Dewar capacity (C_D) yields a potential frequency response capability of

$$f_h = 1/2\pi R_{in}(C_{in} + C_D) \geqslant 100\ \mathrm{kHz} \tag{44}$$

which is sufficient to cover the required 30 kHz.

Figure 17 gives the results of frequency response tests on the GaAs preamplifier-auxiliary amplifier combination. Both curves (bandwidth = 3 and 30 kHz) were obtained by using a 2-MΩ wire-wound resistor as a noise source, inasmuch as a detector was not available at the time. The resistor frequency characteristics were a remarkable simulation of the detector. Noise was used as the signal source for the 30-kHz measurement because the highest speed chopper available was 5 kHz. Although the 30-kHz bandwidth goal was not attained in this test, the 15 kHz obtained was judged to be sufficient. The feedback circuit, R_{F1}, C_S, and R_S of Figure 16, can be used to adjust high frequency response when a more reliable signal source is available. Noise and chopped blackbody tests indicated the 3-kHz bandwidth was quite accurate.

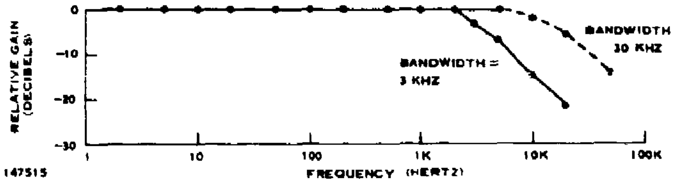

Figure 17. Gallium Arsenide Preamplifier Auxiliary Amplifier Combination Relative Frequency Response

c. Noise Considerations

Noise considerations for this preamplifier are not too stringent because of the relatively high detector-output noise voltage (200 nV/Hz$^{1/2}$). When a detector-preamplifier combination is put together, one important consideration is the relationship of preamplifier total equivalent input noise voltage (v_{nAT}) and detector output noise voltage (v_{nD}). Since detector D* (D_D*) is inversely proportional to noise, it is desirable for the preamplifier to add as little noise as possible so that system D* (D_S*) is degraded only a minimum amount from that of the detector (D_D*). For example, if

$$v_{nAT} \leqslant v_{nD}/2 \tag{45}$$

then

$$D_S{}^* \geqslant 0.87\ D_D{}^* \tag{46}$$

a barely detectable D* degradation. Further, if

$$v_{nAT} = v_{nD} \tag{47}$$

then

$$D_S{}^* = 0.707\ D_D{}^* \tag{48}$$

a usually reasonable limit to D* reduction. For the GaAs preamplifier $v_{nAT} \leqslant 53$ nV/Hz$^{1/2}$. Thus, with $v_{nD} \cong 200$ nV/Hz$^{1/2}$, this preamplifier betters the relation in Equation (45) by a factor of 2 and

$$D_S{}^* = 0.97\ D_D{}^* \tag{49}$$

v_{nAT} for this preamplifier is given by the relation,

$$v_{nAT} \overset{<}{\cong} v_{nR_{IN-P}} \cdot \frac{R_D}{R_{IN-P}} \oplus v_{nA}(1) \oplus i_{nT} \cdot R_D \ (\mathrm{nV/Hz^{1/2}}) \tag{50}$$

where

$v_{nR_{IN-P}}$ = Johnson-Nyquist (thermal) noise voltage (nV/Hz$^{1/2}$) of the amplifier passive input resistance ≅1.2 μV/Hz$^{1/2}$

R_D = detector resistance ≅2 MΩ

R_{IN-P} = preamplifier passive input resistance ≅83.3 MΩ

$v_{nA}(1)$ = preamplifier short-circuit equivalent input-noise voltage at 1 Hz ≤ 40 nV/Hz$^{1/2}$, a nearly worst case

i_{nT} = input transistor equivalent open-circuit input-noise current ≅10^{-2} pA/Hz$^{1/2}$

$\oplus$ = quadrature addition.

d. System D* Versus Detector D*

Measurements indicated no essential difference between detector D* and detector-preamplifier-auxiliary amplifier D* for the GaAs system.

2. Indium Antimonide Preamplifier

This preamplifier is shown schematically in Figure 18 and is basically an ac-coupled noninverting amplifier of simple design fed back in a conventional manner for a closed loop gain of 10^3. The input stage employs a pair of low noise voltage JFETs (Q-1) which operate in parallel for lower noise voltage performance. The second stage employs a single, low-noise voltage and current bipolar transistor (Q2). The output circuit is a complementary bipolar transistor push-pull pair (Q3 and Q4).

Operating characteristics and parameters for this preamplifier are summarized in Table II.

a. Detector Bias

Detector bias is provided by the constant-current source circuit, involving transistor QA and the IN754 zener diode as indicated in Figure 18. The constant-current technique

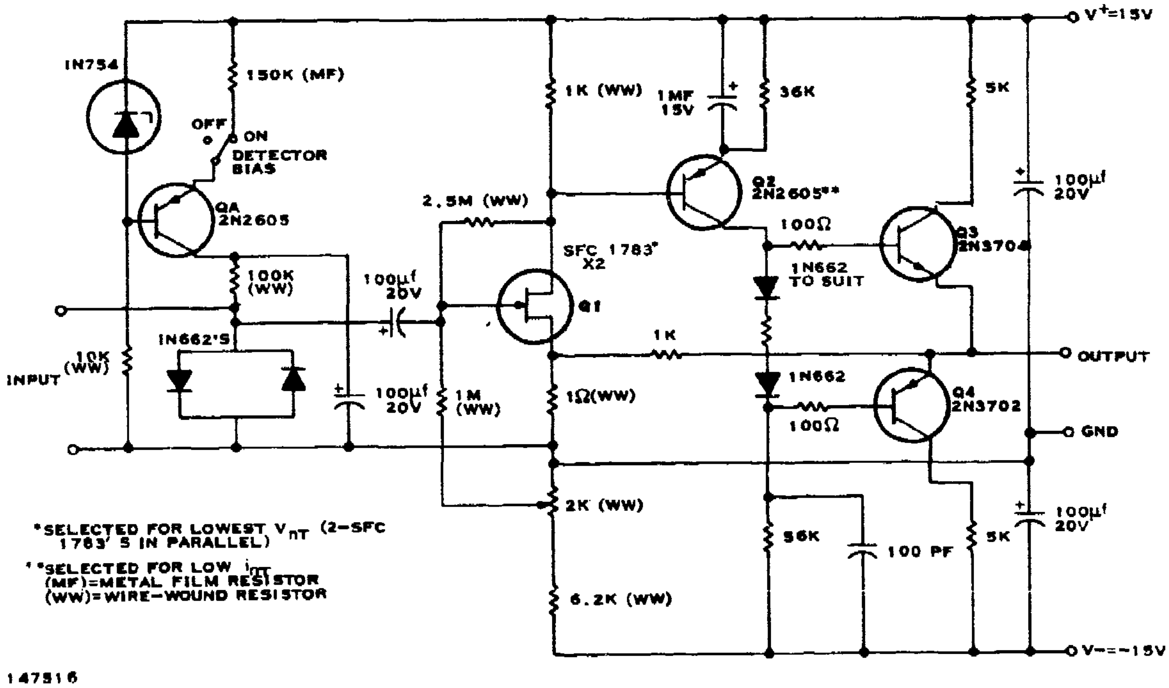

*SELECTED FOR LOWEST V_{nT} (2−SFC 1783' S IN PARALLEL)

**SELECTED FOR LOW i_{nT}

(MF)=METAL FILM RESISTOR

(WW)=WIRE−WOUND RESISTOR

Figure 18. Indium Antimonide Detector Preamplifier Schematic

of biasing was employed, since detector resistance was invariant with background. As an example one of the earlier detectors used in the system will be considered. It had an optimum bias current of ≅40 μA, yielding a bias voltage of ≅30 mV across the 750 Ω detector.

b. Frequency Response

Attaining a high end-frequency response of ⩾30 kHz with this detector-preamplifier combination was no problem because of the low detector resistance. Frequency response curves are given in Figure 19. The low-frequency, closed-loop −3-dB point of 0.05 Hz is set by the ≅1-mF capacitor bypassing the Q2 emitter resistor and the loop gain of 20 dB.

c. Noise Considerations

The moderately low InSb detector resistance poses stringent preamplifier noise requirements. This detector, beyond its 1/f region (in this instance ≅2 kHz), exhibits essentially the Johnson-Nyquist noise of a 750-Ω resistor cooled to 4.2°K. The magnitude of this noise is given by

$$v_{nD} = (4kTR_D)^{½} \cong 0.42\ \text{nV/Hz}^{½} \tag{51}$$

This means, according to relations (47) and (48), that to keep detector D* (D_D*) degradation by the preamplifier ≅30 percent, that

$$v_{nAT} \lesssim 0.42\ \text{nV/Hz}^{½} \tag{52}$$

TABLE II. InSb PREAMPLIFIER CHARACTERISTICS AND PARAMETERS

Characteristic/Parameter	Value
Open loop gain (g)	$10^4 \frac{v}{v}$
Open loop frequency response	
Low (fl)	1 Hz
High (f_h)	49 kHz
Closed loop gain (gcl)	1 k (v/v)
Closed loop frequency response	
Low (fl)	0.05 Hz
High (f_h)	308 kHz
Noise characteristic	
V_{nA} (1 kHz)	0.46 nV/Hz^{½}
(2.0 Hz)	~4.0 nV/Hz^{½}
i_{nA} (1 kHz)	≲ 0.1 pA/Hz^{½}
(2 Hz)	<4 pA/Hz^{½}
Input parameters	
R_{in}	~90 kΩ
C_{in}	– pF
Output parameters	
R_o	<26 Ω
Maximum output swing	+4V, −14V
Voltage supply	
V^+	15V
V^-	15V
Quiescent current drain	
I^+	~10.5 mA(C)
I^-	~2.5 mA(C)
Power	195 mW(C)

NOTE: For I drain indicate C or E for calculated or estimated, or M for measured.

For this preamplifier design, refer to relation (50) and its glossary.

$$v_{nR_{IN-P}} \cdot \frac{R_D}{R_{IN-P}} \simeq 0.32\ \text{nV/Hz}^{½} \tag{53}$$

Solving relation (50) for terms involving v_{nA} and i_{nT} yields

$$v_{nA} \oplus i_{nT} R_D = v_{nAT} \ominus v_{nR_{IN-P}} \frac{R_D}{R_{IN-P}} \tag{54}$$

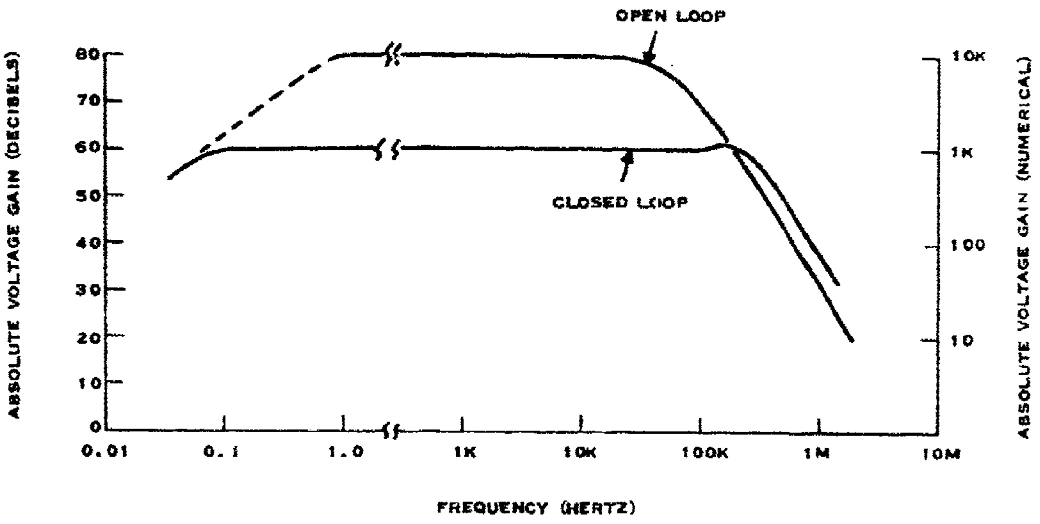

147517

Figure 19. Indium Antimonide Preamplifier Absolute Gain Versus Frequency

Substituting values from Equation (52) and (53) into Equation (54) yields the result that

$$v_{nA} \oplus i_{nT} \cdot R_D \leq 0.273 \text{ nV/Hz}^{1/2} \tag{55}$$

Equation (55) indicates the short-circuit equivalent input-noise voltage of the input active devices should be such that

$$v_{nT} \leq 0.273 \text{ nV/Hz}^{1/2} \tag{56}$$

and their open circuit equivalent input noise current should be

$$i_{nT} \leq 0.183 \text{ pA/Hz}^{1/2} \tag{57}$$

where $v_{nT} \equiv v_{nA}$ for nondifferential input stages. Many paralleled bipolar transistors could probably satisfy Equation (56), however, in so doing they could not satisfy Equation (57) within about an order of magnitude. A compromise input design using JFETs was selected in which v_{nT} would be higher than that suggested by Equation (56) but in which Equation (57) could be met.

Theoretically, beyond the 1/f region JFETs exhibit, a short-circuit equivalent input-noise voltage given by

$$v_{nT} \approx (4kT/y_{fs})^{1/2} \text{ (nV/Hz}^{1/2}) \tag{58}$$

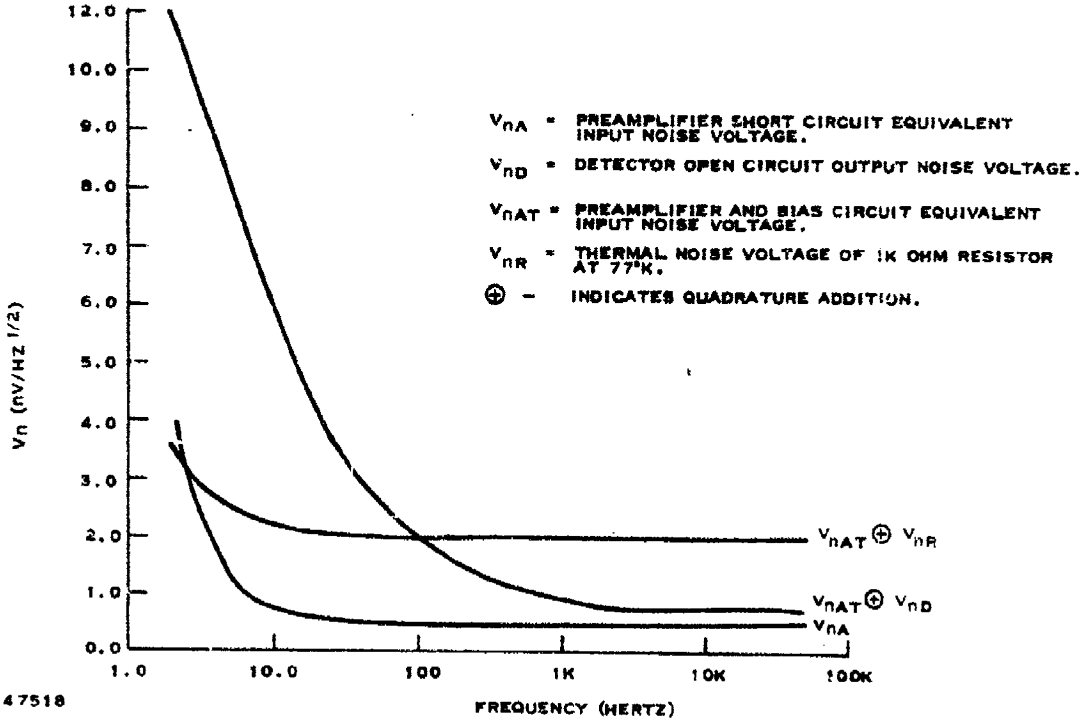

Figure 20. Indium Antimonide Detector and Preamplifier Noise Voltage Versus Frequency

Two of the JFETs (SFC-1783s) selected, operating in parallel each at 5 mA = i_D (drain current), exhibit a y_{fs} of 80 mmhos. Operation of these devices at t = 300°K should yield a $v_{nT} \approx 0.455$ nV/Hz$^{1/2}$. Operational noise test results using these devices in the InSb preamplifier are shown in Figure 20. The curve labeled v_{nA} demonstrates v_{nT} performance at 0.47 nV/Hz$^{1/2}$ at frequencies $\geqslant$1 kHz. This value is well within measurement error (±10 percent) of the theoretical value given in Equation (58). The $v_{nAT} \oplus v_{nD}$ curve gives the measured spectrum of detector and preamplifier operating together. The $v_{nAT} \oplus v_{nR}$ curve is the noise spectrum of a 1-kΩ wire-wound resistor cooled to 77°K, amplified by the preamplifier. The increased amplitude of this curve at low frequencies, that is, 3 6 nV/Hz$^{1/2}$ at 2 Hz, can be attributed to increasing i_{nA} with decreasing frequency.

d. System D* Versus Detector D*

The 30-percent detector D* degradation goal has not been met for this InSb detector with this preamplifier at frequencies beyond 2 kHz. The ratio

$$\frac{v_{nAT} \oplus v_{nD}}{v_{nD}} \approx \frac{0.77\ \mathrm{nV/Hz^{1/2}}}{0.42\ \mathrm{nV/Hz^{1/2}}} = 1.83 = 5.26\ \mathrm{dB} \tag{59}$$

indicates a degradation of 83 percent.

This degradation could be reduced to 52 percent (3.64 dB) if R_{in-P} were increased to 1 MΩ. This would require revision of the constant-current detector bias circuit. Further degradation reduction would require additional paralleled JFETs and/or operation at higher drain currents to obtain increased y_{Fs} and to reduce preamplifier noise according to Equation (58). Care must be exercised here because of increased i_{nT} with increased I_D or number of input devices. Both of these potential degradation reduction techniques require further study.

e. Supply Line Rejection

The InSb preamplifier has poor supply-line variation rejection and will not operate within its noise specifications with the present regulator circuit shown in Subsection B.3. The reason for the preamplifier "subnormal" rejection is not understood completely and needs further investigation. The preamplifier works well on batteries or a well-filtered auxiliary supply. Improved supply line decoupling, or a lower output noise regulator, or both, could be employed to render the present preamplifier compatible with the rest of the prescanner electronics.

3. Auxiliary Amplifier

The auxiliary amplifier provides

a. Voltage gain necessary to raise preamplifier signal and noise levels to that required at the scanner input

b. High-frequency limits for 2 bandwidths; 3 and 30 kHz

c. Step variable gain for the 2 bandwidths and the two detectors

d. Continuously variable gain adjust

e. Inversion circuitry to invert the inverted signal output from the GaAs preamplifier

f. A step-down (±30 to ±15 V) voltage regulator to bridge from scanner mains to those required by the pre- and auxiliary amplifiers.

The auxiliary amplifier is shown schematically in Figure 21. It is composed of two essentially identical amplifier sections (1 and 2) which are separated by an inverter circuit. Each amplifier section employs an Analog Devices Inc., Model 105C, operational amplifier fedback in a simple noninverting connection which establishes voltage gains and high-frequency bandwidth limits ($f\ell$). As mentioned, the inverter circuit is used only in the GaAs detector selection switch position to invert the inverted GaAs preamplifier output.

Table III summarizes auxiliary amplifier gains and frequency responses as a function of selector switch positions. Figure 22 graphs voltage gains versus frequency. Gains were calculated according to the equation,

$$g_{AA} = v_{noT}/v_{niT}\ g_p\ (BW)^{1/2} \qquad (60)$$

where

g_{AA} = auxiliary amplifier voltage gain (V/V)

v_{noT} = output noise voltage required at input to scanner ≈0.3-V rms

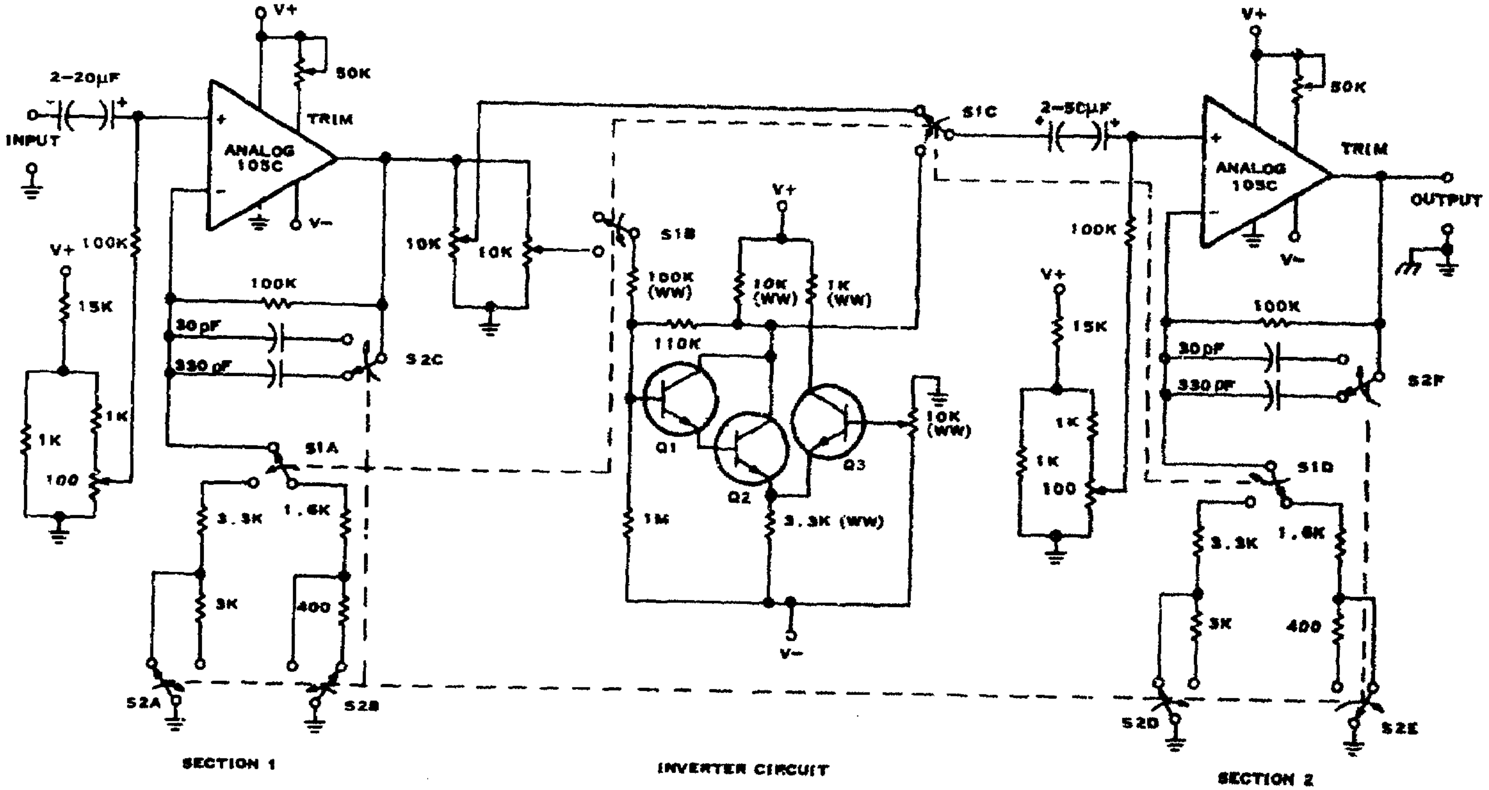

NOTES:

1. S1 SHOWN IN InSb DETECTOR POSITION.
2. S2 SHOWN IN BW = 3 KHZ POSITION.
3. CURVED ARROWS ON SWITCHBLADES INDICATE CW ROTATION
4. Q1, Q2, AND Q3 ARE 2N3704'S.
5. ALL NONGROUND SWITCH LEADS ARE SHIELDED.
6. (WW)=WIRE-WOUND RESISTOR

147519

Figure 21. Auxiliary Amplifier Schematic Diagram

TABLE III. AUXILIARY AMPLIFIER GAINS AND FREQUENCY RESPONSES VERSUS SELECTOR SWITCH POSITION

Detector Switch Position	GaAs		InSb	
Bandwidth Switch Position	3k	30k	3k	30k
Section voltage gain (V/V)	30	16.7	63.3	50
Total auxiliary amplifier voltage Gain (V/V)	900	280	$4 \cdot 10^3$	$2.5 \cdot 10^3$
Frequency response				
fℓ (Hz)	0.17	0.17	0.17	0.17
fh(Hz)	3.5	33.5	3	31.8

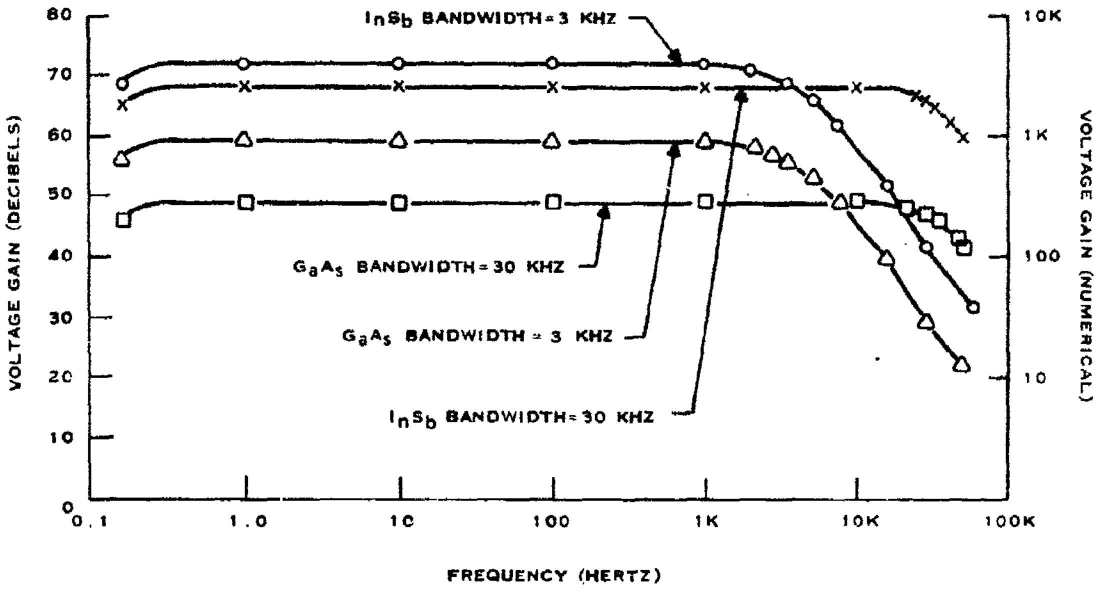

147520

Figure 22. Auxiliary Amplifier Absolute Voltage Gains Versus Frequency

v_{niT} = total input noise voltage at preamplifier input ($nV/Hz^{1/2}$) = $v_{nAT} \oplus v_{nD}$

BW = frequency bandwidth desired (Hz) = 3 or 30 kHz

g_p = preamplifier voltage gain (V/V).

Figure 23 gives the schematic diagram of the simple regulator circuit employed for the preamplifiers and auxiliary amplifier supply voltages.

C. Scanner Design

The optics and electromechanical design of the scanner were pursued with the Imaging Crowd Surveillance System objective in mind. This objective was to demonstrate the feasibility

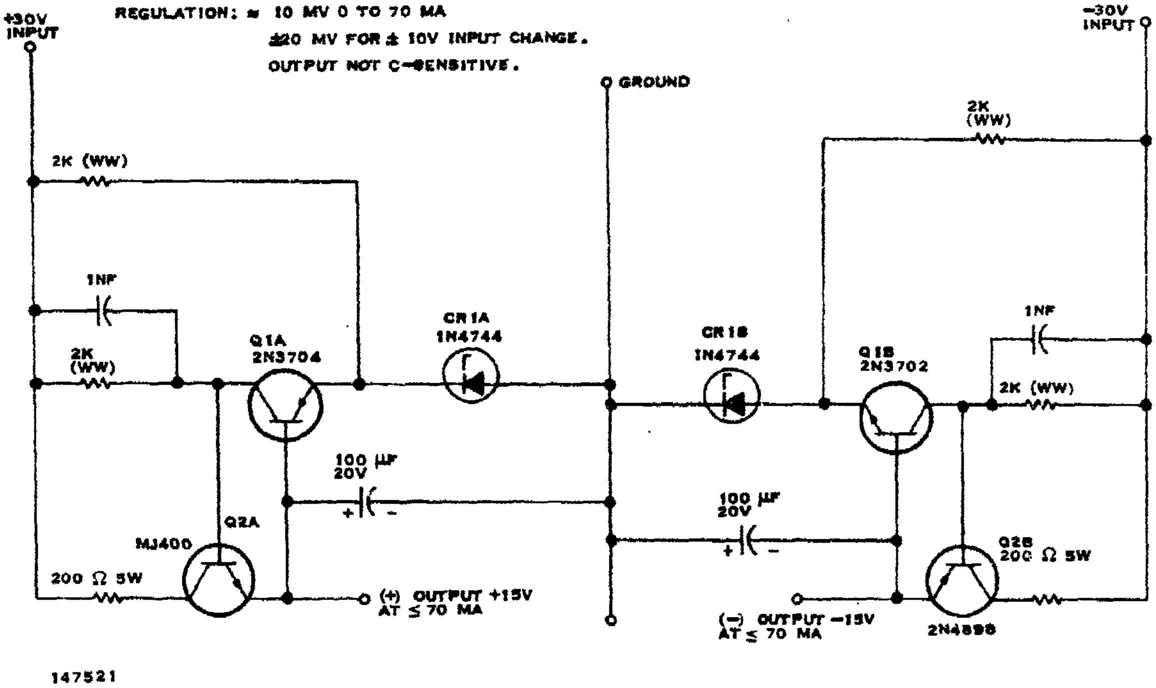

Figure 23. Regulator Circuit Schematic

of a submillimeter, infrared imaging system for use in detecting concealed handguns and to make projections about future improvements and component development possibilities. Because expediency was important, the design constraints precluded any significant investigation in innovative fabrication techniques and exotic optical systems and relied instead on tried and proven concepts and system fabrication techniques. The experimental laboratory-type hardware which was developed to achieve the overall program objective is shown in Figure 24. In the figure, the right-hand portion shows the breadboard scanner. The key components have been identified on the photograph.

Vertical scan mirror, A

Horizontal scan mirror, B

Ellipsoidal primary mirror, C

Detector/Dewar assembly, D

Blackbody reference elements, E.

The modified Thermlscope® recorder is shown in the lower left-hand portion of Figure 24. To clarify the scan action/optical configuration of the system, the optical design is discussed at length in the following subsections.

1. Optical Design

Certain restrictions were placed on the optical design as a result of earlier studies related to the feasibility of this type of system. These design goals are reflected in the system specifications as set forth in the contract.

®Texas Instruments Incorporated.

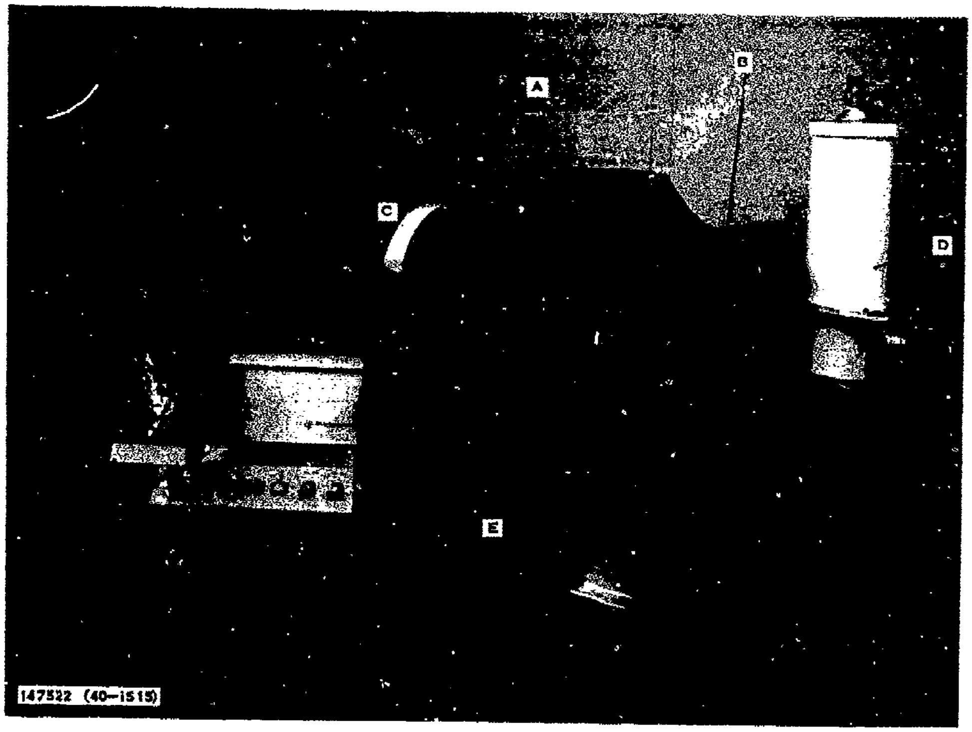

Figure 24. Imaging Crowd Surveillance System

a. Instantaneous field of view, $\Delta\theta$, 1.7 X 1.7 mrad for the GaAs 300-μm detector and approximately 2 X 2 mrad for the InSb 500-μm or greater, detector.

b. Effective aperture, D_o = 30-cm diameter (707 cm^2)

c. Equivalent optical *f*-number = 2.5

d. Total field of view, 100-mrad horizontal by 330-mrad vertical.

An abbreviated ray trace of the optical system designed to fulfill these requirements is shown in Figure 25. In the figure, the optical system is seen as viewed from above the system platform or baseplate. The radiated energy from the object plane is scanned by the six-sided vertical scan mirror which rotates about a horizontal axis. In turn, the energy is reflected from each individual face of the scan mirror onto the horizontal scan mirror which oscillates about its vertical axis and then onto the ellipsoidal primary mirror shown at the left of the figure. Finally, this energy is focused from the primary mirror onto the detector located in the image plane. With this optical configuration, the object plane is scanned from top to bottom by the vertical scan mirror and left to right by the horizontal scan mirror. This scan format is shown in Figure 26 and was chosen instead of the normal Thermlscope format of left to right and top to bottom to obtain higher scan efficiency than was originally proposed. It is more efficient to scan the longest dimension in the required object plane scene with the high-speed scanning element because this scanning element and its angular scan rate in conjunction with the required instantaneous angular field of view, $\Delta\theta$, determine the required system information bandwidth. The improved scan efficiency or scan duty cycle obtained by scanning the long dimension of the scene may be utilized to reduce the total picture frame time or to reduce the individual line-scan

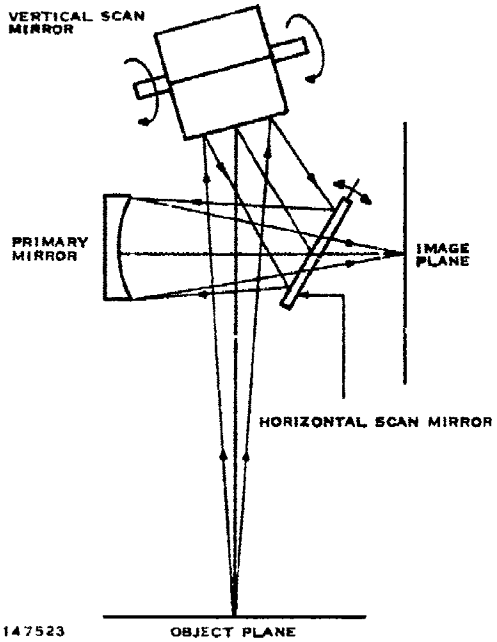

Figure 25. Optical Schematic

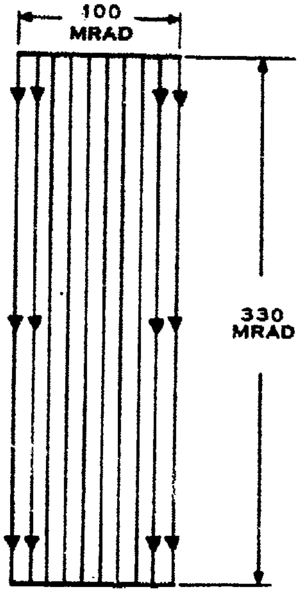

Figure 26. Scan Format

rate which, in turn, reduces the information bandwidth requirement. The square root of the bandwidth is directly proportional to the system thermal sensitivity, a relationship which indirectly indicates the advantage of utilizing the highest possible scan efficiency. In this case, the scan time for the complete picture frame was held at the proposed value and the increased scan efficiency was traded for reduced bandwidth and the attendant improvement in system sensitivity. Theoretically, this improvement would be the square root of 3.3, or a factor of 1.8.

The optical design was made with a geometrical ray trace construction on the drafting board. This is an iterative graphical-design procedure in which system optical requirements (effective aperture of 707 cm^2 and an ellipsoidal primary element having focii of 1 meter and 3 meters) and field-of-view requirements (100 mrad horizontal by 330 mrad vertical) were used to make a geometrical ray trace. In this process, an elementary ray trace diagram of a simple lens system is constructed to a convenient scale and cut out for use as a design aid as shown in Figure 27. The basic design aid is shown as a simple lens focused at a finite object distance in Figure 27A. In Figure 27B, this same ray trace is shown folded back upon itself at the plane of the primary optical element, that is, a reflective primary element. In the final portion of the figure, the ray trace is shown folded at the plane of the horizontal and vertical scanning (folding) mirrors. By manipulating the optical axis of the ray trace design aid through the extremes of the required scan angles and by refolding the model at the respective scan mirror planes the minimum size limits of the scan mirror surface may be determined. Although the figure illustrates the procedure for the horizontal scan direction, the procedure for the vertical scan direction is essentially the same.

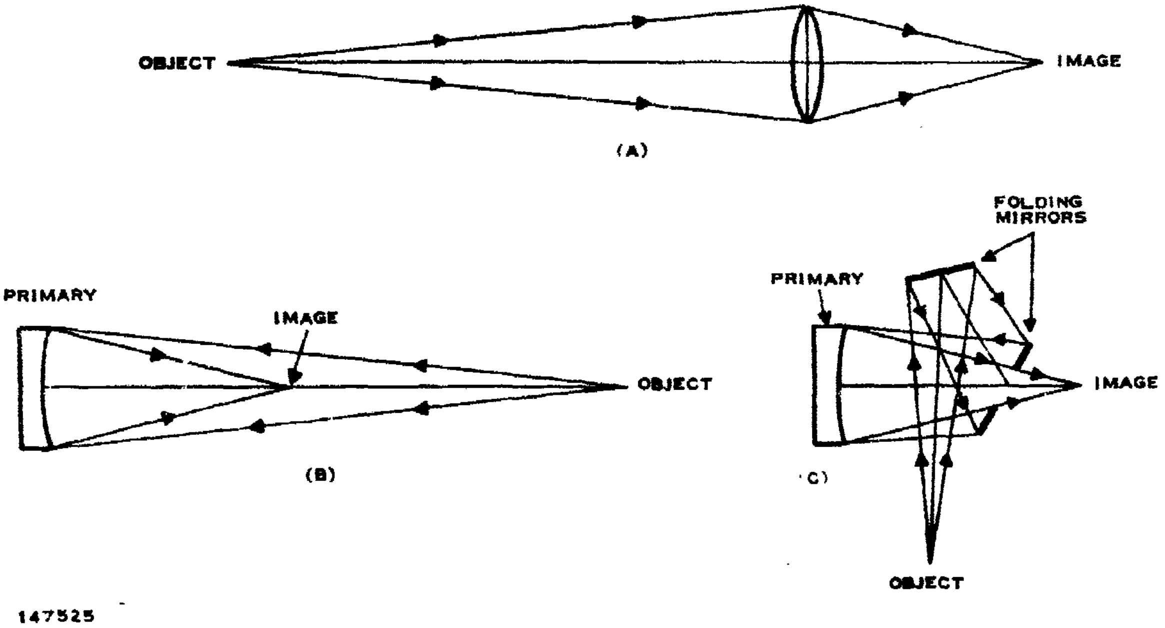

Figure 27. Example of Preliminary Optical Layout Design

After the basic design aid is used to obtain a configuration that is feasible, a formal, large-scale ray-trace layout is completed to more accurately define and locate the various mirror surfaces. When this is done and any minor adjustments are made to the ray trace diagram, verification is made of the various constraints placed on the optics system such as the field of view and effective aperture. A reasonable minimum diameter of the aperture stop, which in this case is defined by the primary mirror, is determined primarily by diffraction limit considerations. In the original ray-trace layout of the optics system, the minimum aperture diameter is used and then at this point the area is calculated to verify that the minimum aperture is achieved. If it is not, then the diameter would be adjusted upward and further adjustments made in the ray trace to provide the required scanned field of view for the system. For this system, the ray trace revealed that a 4.5-inch diameter obscuration is required in the horizontal scan mirror to allow the extreme rays of the optics system on the image side of the primary to illuminate the detector. To determine the actual area of the optical aperture, this 4.5-inch diameter obscuration which lies between the primary optical element and an object plane located at a finite distance, must be projected onto the plane of the primary element. The projected obscuration obtained from the ray trace was used in conjunction with the overall diameter of the primary mirror to obtain the total area of the aperture, in this case 707 cm^2.

Another important consideration of the optics design is the determination of the optical modulation transfer function (MTF). It was recognized from the outset that the system would be diffraction limited. To determine the extent of this limitation, a brief study was made of the MTF for the optics. This investigation included operation at a wavelength of 300 μm for the GaAs detector and 500 μm for the InSb detector. The actual InSb detector used in the breadboard system had a peak spectral response near 800 μm and so the MTF at this point in

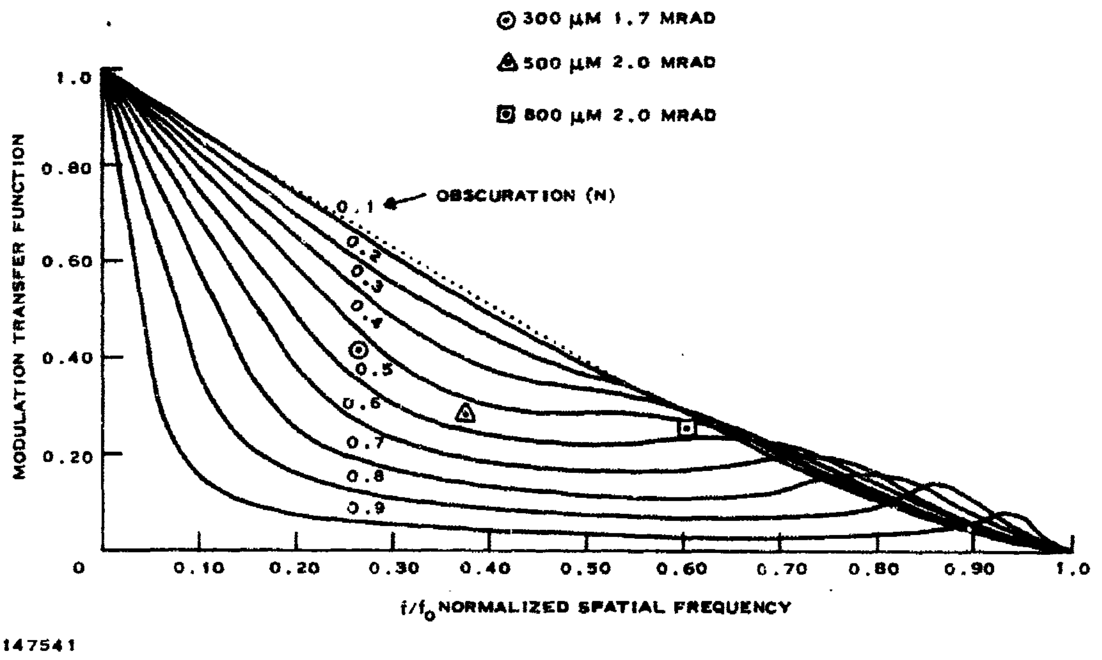

Figure 28. Modulation Transfer Function for a Perfect Lens With a Central, Circular Obscuration

the spectrum was also calculated. There are a number of mathematically rigorous approaches available for determining the MTF of an optical system the results of which appear in references.[13] Figure 28 graphically presents the MTF for various values of normalized spatial frequency, f/f_0. Curves are presented for various values of n, which is the ratio of the diameter of the central obscuration to the overall diameter of the lens or mirror. To use the chart, the cutoff spatial frequency, f_0, and the spatial frequency of interest, f, must be computed. The cutoff frequency is defined as

$$f_0 = \frac{D_0}{\lambda}$$

where D_0 is the diameter of the aperture defined by the mirror, and λ is the wavelength of interest. The operating frequency is defined as

$$f = \frac{1}{2\Delta\theta}$$

where $\Delta\theta$ is the instantaneous field of view. The calculation of these parameters for the present system is shown in Table IV. The chart is entered with these values of normalized spatial frequency and the diffraction MTF for the optics systems is determined. As seen in Figure 28, at 300 μm with an instantaneous field of view, $\Delta\theta$, of 1.7 mrad, the normalized spatial frequency is 0.265 of cutoff. At the obscuration ratio of 0.442 which exists in this system, the MTF is seen to be 42 percent. At 500 μm, with a $\Delta\theta$ of 2 mrad, the MTF is 28 percent. It is interesting to

TABLE IV. MODULATION TRANSFER FUNCTION CALCULATIONS

GaAs – 300 μm – 1.7 mrad

$$f = \frac{1}{2\Delta\theta} = \frac{1}{2(1.7 \times 10^{-3})\text{rad}} = 0.294 \times 10^{3}$$

$$f_o = \frac{D_o}{\lambda} = \frac{33.3 \text{ cm}}{3 \times 10^{-2} \text{ cm}} = 11.1 \times 10^{2}$$

$$\frac{f}{f_o} = \frac{0.294 \times 10^{3}}{11.1 \times 10^{2}} = 0.265$$

$$n = \frac{d_x}{D_o} = \frac{5.82 \text{ in}}{13.125 \text{ in}} = 0.442 \text{ in}$$

InSb – 500 μm – 2.0 mrad

$$f = \frac{1}{2\Delta\theta} = \frac{1}{2(2 \times 10^{-3})\text{rad}} = 0.250 \times 10^{3}$$

$$f_o = \frac{D_o}{\lambda} = \frac{33.3 \text{ cm}}{5 \times 10^{-2} \text{ cm}} = 6.67 \times 10^{2}$$

$$\frac{f}{f_o} = \frac{0.250 \times 10^{3}}{6.67 \times 10^{2}} = 0.375$$

InSb – 800 μm – 2.0 mrad

$$f_o = \frac{D_o}{\lambda} = \frac{33.3 \text{ cm}}{8 \times 10^{-2} \text{ cm}} = 4.17 \times 10^{2}$$

$$\frac{f}{f_o} = \frac{0.250 \times 10^{3}}{4.17 \times 10^{2}} = 0.6$$

note that only a small variation in diffraction MTF occurs when the system is operated with a detector responding at 800 μm. As seen in the figure, the MTF at this point is 25 percent. This is within 10 percent of the modulation to be expected with operation at 500 μm with a similar size detector. This would indicate that the system, as it is now configured, could be operated at even longer wavelengths (to the order of 1 mm) without experiencing prohibitive modulation degradation.

Another consideration of importance in determining the overall optics MTF is the degradation due to geometric blur and other aberrations associated with a given optical system. There is no readily available means of determining the MTF degradation due to these effects; however, for an ellipsoidal primary and a fixed focal distance on the optical axis the theoretical aberrations are minimal and any significant aberrations present would be due primarily to fabrication defects. The actual surface finish on the optical surfaces is within 0.1 wavelength at 300 μm which compares favorably with the tolerances allowed for high-quality optics utilized in the near infrared. In view of this, diffraction effects are greater than those associated with geometric blur and inherent, as well as induced, aberrations.

The three optical-fabrication design considerations related to this system are surface finish, strength, and material selection. These considerations are discussed briefly.

To save time while assuring adequate precision and rigidity, a decision was made early in the program that the basic principles utilized in designing shorter wavelength infrared optics would be applied to this system. A reasonably high-quality optical system can be achieved by holding the tolerance of the optical surface finish within 0.1 wavelength flatness in the case of a relay mirror, or within 0.1 wavelength of the desired curve for a surface of revolution. At the shorter wavelength mode of operation, the wavelength is nominally 300 μm or 0.012 inch. For this reason, all fabrication drawings for the optical elements specified at least a 32-surface finish and held the flatness or curve tolerance to within 0.001 inch. Measurements of the completed parts indicated that these tolerances were achieved.

The strength considerations related to the optical design were those of dynamic loading in the case of the rotating vertical scan mirror and static loading in the case of the primary mirror and the horizontal scan mirror. Stress calculations which considered the size, as well as the rotational speed required for the vertical scan mirror, revealed that 3/8-inch aluminum alloy, when properly supported, would be sufficiently rigid to achieve the required optical tolerances. The entire scan mirror assembly, which consisted of six mirror faces, the three hexagonal supporting webs, and the shaft, was fabricated on a piece-part basis and then was assembled as a weldment. This assembly was machined to the optical tolerances required by the system. To preclude the possibility that the weight of the remaining optical elements would distort the optical surface profile, the thickness of these elements was designed to be nominally 10 percent of their largest dimension in accordance with the optical rule of thumb.

The material selected for fabrication of the optical elements was 6061 aluminum alloy. This material met the strength requirements as previously discussed and had the advantage of being easily machined to the surface finishes required by the system. Other materials such as honeycomb and fiberglass could have been used for optical fabrication and would have reduced overall system weight. It was believed, however, that program schedule constraints as well as uncertainties in new fabrication techniques should preclude any major attempt to advance the state-of-the-art in optical fabrication techniques. This is in keeping with the original program objective which was to demonstrate the feasibility of a submillimeter (or long wavelength infrared) imaging system. Now that the feasibility of this type system has been demonstrated, it would be worth while to study other optical fabrication techniques.

2. Electromechanical Design

Electromechanical design includes scanner configuration and overall packaging. In addition, the Thermlscope interface was modified to ensure compatibility with the recorder.

The frame time, T_f, is given by

$$T_f = T_v \times N_h$$

The vertical scan time, T_v, is given by

$$T_v = \frac{1}{SK}$$

where S is the scanner rotational speed and K is the number of scans per revolution (6). The number of horizontal picture elements, N_h, is given by

$$N_h = \frac{F_h}{\Delta\theta}$$

where F_h, the horizontal field of view = 100 mrad and $\Delta\theta$, the instantaneous field of view = 1.7 mrad.

Substituting these parameters into the original equation and solving for scan speed yields

$$S = \frac{F_h}{KT_f\Delta\theta}$$

which for the 24-second frame time is

$$S = 0.407 \text{ rev/s (24.4 rpm)}$$

An alternate frame time one-tenth that of the 24.1-second primary frame time was also provided. The scanner must therefore be capable of 244 r/min in the fast scan mode and 24.4 r/min in the slow scan mode. These speeds would require a speed reducer (gear train, and so on) if a standard type of synchronous ac machine were to be used for the prime mover. To avoid some of the problems associated with gears, such as backlash and irregular angular motion, a direct drive which utilizes a dc machine as the prime mover was investigated. A cardboard mockup of the scan mirror was constructed, attached to the shaft of a dc machine, and run at various speeds up to and including the maximum required system scan speed. Power input data revealed that the mechanical load consisted primarily of mirror windage loading at the maximum required speed. At this speed, the dc machine was operating well within its rated load capability.

A brief investigation of a closed loop speed control was conducted. It was hoped that a similar motor could be used as a tachometer for the feedback element. It was found, however, that at the primary or low scan speed commutator noise from the proposed tachometer would be prohibitive. One logical alternative would have been an electro-optical pulse-wheel type of tachometer which would require additional development time and expense. To avoid this, the speed characteristics of a dc motor driving a high inertial load (large scan mirror) and running with a constant voltage impressed on the armature was investigated. The results showed sufficiently stable speed characteristics, thereby allowing the relatively simple and inexpensive approach of using a regulated dc supply to define the scan mirror rotational speed. This approach lends itself to greater system flexibility for future experiments which may require alteration of the basic scan speeds up to a maximum of approximately 450 r/min.

The electronic bandwidth necessary to process the detector video information is dependent upon the scan speed and the system instantaneous field of view.

$$BW = \frac{2\pi S}{\Delta\theta}$$

where

BW = the information bandwidth in hertz

S = the scan speed in revolutions/s

$\Delta\theta$ = the instantaneous field of view in radians

In the slow scan mode of operation, the bandwidth is

$$BW = \frac{2\pi(0.407)}{1.7 \times 10^{-3}} = 1.5 \times 10^{3} \text{ Hz}$$

The bandwidth required for the fast scan mode would therefore be 10 times greater than that required for slow scan, or 15 kilohertz. The recorder bandwidth is far in excess of this value (nominally 100 kHz); therefore, the preamplifier/postamplifier combination bandwidth was tailored to set the overall system bandwidth. It should be noted that the preamplifier/postamplifier gain is so large that it sets the system noise figure performance regardless of the recorder bandwidth.

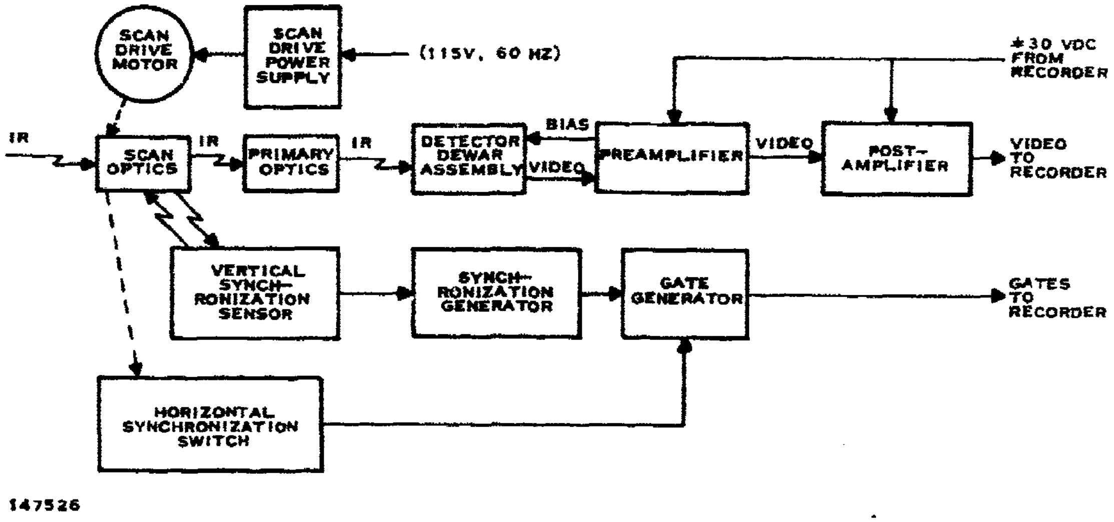

Figure 29. Scanner Block Diagram

Various synchronization and gate pulses normally derived from the Thermlscope scanner unit were needed. The normal synchronizing pulse generation consists of illuminating the Thermlscope scan mirror with focused 0.9-μm radiation from a light-emitting diode (LED). As the scan mirror rotates through the angular position where a synchronizing pulse is desired, the energy from the LED is focused on a phototransistor, the output of which is amplified and used to drive the gate generator circuitry. It was necessary to modify this scheme somewhat because the system optical surfaces for use at 300 to 500 μm are not finely enough polished to permit operation at 0.9 μm. For this reason, the scan mirror was constructed with 6 mounting recesses machined in the end of the mirror to provide a means of incorporating mirror surfaces of sufficient optical quality for the use of 0.9-μm radiation from the LED source. These six mirrors were held in place by slotted masks which were adjustable with respect to the individual scan mirror faces. When the system was operating, a long bar-type target could be observed. Adjustments were made in the individual mirror masks to provide line-to-line correlation and registration for the video signal presented by the recorder.

An overall understanding of the scanner operation may be obtained with the aid of the functional block diagram shown in Figure 29. The scene is scanned by the scan optics consisting of the hexagonal vertical scan mirror which is directly driven by the dc scan drive motor. A belt drive is provided from the scan motor to a gear reducer, the output of which drives the horizontal scan cam. The cam follower then drives the horizontal scan mirror through the horizontal scan cycle. A secondary horizontal timing cam is attached to the position cam to actuate the horizontal synchronizing switch and to provide the horizontal gate timing logic. The

TABLE V. SCANNER DESIGN PARAMETERS

Effective aperture area	=	707 cm^2	
Image distance	=	100 cm	
Object distance	=	300 cm	
Detector size	≃	0.17 cm X 0.17 cm	
Instantaneous field of view	=	1.7 mrad	
Total field of view	=	100 mrad X 330 mrad	
Duty cycle	=	15.6 percent	
Scan speed, S	=	24.4 r/min	244 r/min
Vertical scan period	=	62.5 ms	6.25 ms
Frame time	=	24.1 s	2.41 s
Information bandwidth	=	1.5 kHz	15 kHz

vertical synchronization is derived from the vertical synchronizing sensor assembly, the output of which is used to generate the various synchronous pulses necessary for operation of the gate generator. Horizontal and vertical synchronizing are utilized by the gate generator to produce the gate outputs required by the sweep circuitry in the recorder.

The infrared energy in the scanned scene is reflected by the elliptical primary mirror and focused upon the detector which is located on the cold surface in the Dewar assembly. The detector receives dc bias from the preamplifier and converts the variations in incident infrared radiation into an electrical signal which is amplified by the preamplifier located on the side of the detector Dewar assembly. The postamplifier contains bandwidth-limiting circuitry and variable gain functions as well as sufficient additional gain to interface with the recorder video circuitry.

Although not specifically shown in the block diagram, blackbody reference elements are included in the system so that the detector is illuminated by the element during a portion of each scan. In this manner, a constant video signal level is present to enable dc restoration by the synchronous clamp circuitry in the recorder.

The performance parameters for the scanner are summarized in Table V. Since these parameters are discussed in detail in other sections of this report, they are not discussed at this point but are presented only as a summary of the scanner design.

D. Recorder Design and Operation

The recorder used with the system was a standard Thermlscope® cathode-ray tube (CRT) recorder which was equipped with a Polaroid oscilloscope camera. The imagery was recorded on Polaroid Type-52 film. This recorder was incorporated into the overall system design by means of a few relatively minor design modifications.

As shown in the block diagram, Figure 30, the Thermlscope recorder contains all of the functions necessary to process the scanner output into a photographic image. In addition to the video processing electronics and sweep circuitry, a power supply with ±30 Vdc, +5 Vdc, and +150 Vdc is provided in the recorder. The design concept which was followed for this system was to utilize as much of the existing recorder as possible and make only those modifications required to attain the specified system performance.

The CRT sweep function in the recorder is derived from the vertical and horizontal sweep generator circuitry which are driven by the gate generator outputs of the scanner. The sweep generators were able to operate at rates necessary for this system. The only changes necessary, since the generators are triggered and not free-running, were those of increasing the RC time constants of the individual sweep circuits. The space allocated on the original boards was

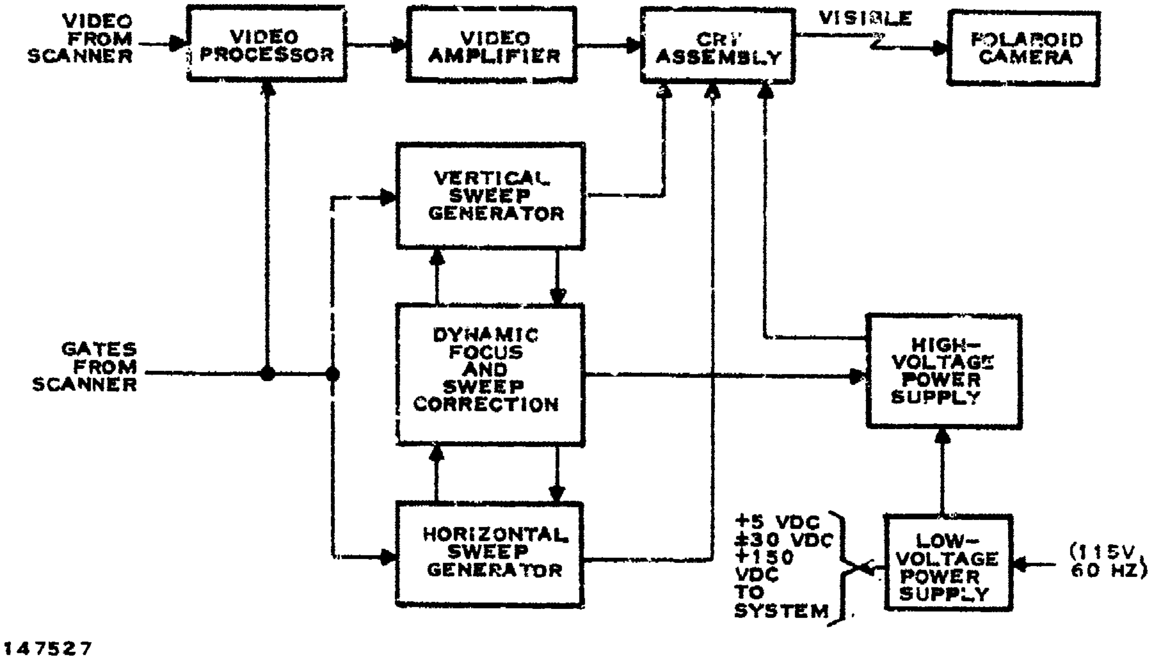

Figure 30. Recorder Block Diagram

sufficient to accommodate the mounting of the larger timing capacitors, thereby eliminating the need for a new printed circuit board layout and fabrication. The resulting sweep outputs are used to drive the deflection yoke windings as well as the dynamic focus and sweep correction circuitry which is located on a separate board.

Alteration of the basic sweep waveforms necessary to provide optimum linearity and geometrical fidelity of the CRT raster scan is obtained by means of nonlinear (multiplier) circuitry on the dynamic focus and sweep correction board. The horizontal and vertical sweep waveforms are fed to this board which generates the necessary correction signals to dynamically control the output of the individual sweep boards. This board also generates a focus control signal which is a function of the CRT spot position relative to the overall CRT raster. This signal is used to modulate the focus anode voltage regulator in the high-voltage power supply. In this manner, dynamic focus of the CRT spot on the face of the tube is achieved.

The power supply circuitry in the recorder consists of the high-voltage supply for the CRT as well as the low-voltage supply previously mentioned. The current ratings of the ±30 and +5 Vdc supplies are in excess of the recorder current requirements. For this reason, the ±30 Vdc was made available at the scanner for use in the video preamplifier and postamplifiers. It was also used in conjunction with the +5 Vdc supply to power the synchronizing generator and gate generator circuitry.

The video chain in the recorder consists of the video processor and video amplifier boards as well as the CRT assembly. As shown in the block diagram the video interface consists of the video input from the scanner which accepts a nominal 1-V peak-to-peak video level. In addition, the video and clamp gates from the scanner gate generator circuitry are required to define the active video interval and to actuate the synchronous clamp circuitry for dc restoration. The composite video consists of an on-time, or active portion, followed by a dead, or inactive portion, where the incoming video from the postamplifier is blanked out. During the portion of the dead time when the scanner is receiving energy from the blackbody reference sources the signal level is synchronously clamped to an arbitrary reference voltage level to provide dc restoration. This reference voltage level is determined by a front panel control which enables the operator to center the average level of any portion or slice of the incoming signal within the dynamic operating range of the CRT display and recording camera. The relative size of this video level or slice with respect to the infrared radiation in the scanned scene is determined by a sensitivity control which is located on the front panel. It is by means of this sensitivity, or gain adjustment, in conjunction with the level adjustment that all, or just a small portion, of the radiation variations in the scanned scene may be displayed on the CRT output.

The composite video from the video processor is used to drive the video amplifier circuitry. This circuitry provides video gain and dc level shifting functions as required to make the video signal compatible with the CRT modulation and biasing requirements. Nonlinear circuitry is provided in the video amplifier to provide gamma correction for the nonlinearities in the CRT modulation transfer function. The output of the video amplifier is coupled directly into the CRT cathode in order to modulate the intensity of the CRT spot.

The 5-inch CRT used in the recorder is a precision tube designed for recording instrument applications. In normal Thermlscope operations the tube consistently prints out 450 lines at better than 70-percent modulation. Therefore, the CRT resolution or spot size did not require modification for operation with the present system. In fact, the spot size was set somewhat larger than normal to provide more uniform raster illumination. Although it is not specifically shown in the block diagram, protective circuitry is incorporated in the recorder circuitry to prevent phosphor burns in the tube face should there be a loss of either of the sweeps or critical bias voltages.

The more common definition of dynamic range is the maximum signal excursion capability compared with the minimum signal level encountered, that is, one noise level. To determine the dynamic range of the existing system, measurements of system noise were made using the GaAs detector. The noise voltage was 0.7×10^{-3} V rms at the postamplifier output. Normally, adjustment of the recorder video gains requires a 0.7-V peak-to-peak video signal excursion at the recorder input to drive the CRT from cutoff to saturation. The relationship of these maximum and minimum signals expressed in decibels is given as

$$D_{(db)} = 20 \log \frac{V_{b-w}}{V_n} = 20 \log \frac{0.7}{0.7 \times 10^{-3}} = 20 \log 10^3$$

$$D = 60 \text{ dB}$$

where D is the dynamic range.

This is the ratio of a peak-to-peak signal voltage to an rms noise voltage. This same form of voltage ratio, (p-p volts)/(rms volts), is used in calculating the thermal sensitivity or noise equivalent temperatures of an infrared system because the minimum detectable signal from a statistical standpoint approaches the rms value of the broadband noise rather than the peak-to-peak value. It is for this reason that the rms noise voltage is also used in determining the overall video dynamic range.

SECTION III
SYSTEM PERFORMANCE

A. Imagery

Hundreds of pictures have been taken with this system since it was first placed in operation. As improvements were made, the pictures became better. On the following pages some of the more recent images are shown. They have been selected to illustrate certain features of the system and the relative performance of the two sensors.

1. Thermlscope Pictures

Several pictures were taken with a Thermlscope to show imagery made entirely from emission from the clothing surfaces. The inadequacy of the standard infrared thermoscope for use as a concealed weapons detector is demonstrated with the series of varying contrast photographs in Figures 31 and 32. The weapon is clearly visible in each pose when it is not covered by clothing. However, when under the shirt or suit coat, the pistol can no longer be seen in the image. In the few instances that a partial image of the pistol was seen, the effect was directly traceable to a change in fabric temperature immediately over the weapon. This temperature change was caused by the increased thermal conduction of the body heat to the fabric by means of the metal gun. Since this effect depends so strongly on the tightness of the clothing over the gun, it could not be used as a reliable means of weapon detection.

2. Weapons Concealed on Persons

Figures 33 and 34 show the two most frequently used poses for making the submillimeter imagery. Photographs A and B of these two figures are included to show the concealment of the weapon to ordinary vision. The first set uses a standard suit coat. In the second, a light shirt and suit trousers conceal a pistol. Images C and D of each picture were made with the GaAs detector and the fast, 2.4-s scan. Figures 35 and 36 show similar poses made with the InSb detector and fast scan.

The image quality of the GaAs pictures consistently was better than that of the InSb pictures. However, the InSb detector may hold more promise because of the greater transmission of cloth at the longer wavelengths. Its performance was poorer because the system optics were much better suited to the GaAs wavelength, 0.285 mm, than to that for InSb, 0.75 mm. In addition, InSb detector noise at lower frequencies was greater than for the GaAs detectors. In effect, the GaAs sensor was more nearly optimized than the InSb.

The slow scan did not improve the imagery as much as expected, probably due to system 1/f noise. Surface temperature effects did play a role in the pictures made with the 0.285-mm radiation as illustrated in Figure 37A, B, and C as might be expected, considering the relatively low transmissivity of cloth at this wavelength. Figure 37C was taken immediately after the hand was removed from the coat and shows the fading handprint. Figure 37D is the image of a small (about 3 inches) 22-caliber pistol carried in a shirt pocket. This same pose was taken with a reversed polarity (dark is hot, white cold) in Figure 38D. At no time was imagery improved by using reversed polarity. The pronounced contrast of the tie and shirt collars compared with the

A. .45—CALIBER PISTOL EXPOSED

B. .45—CALIBER PISTOL COVERED BY LIGHT SHIRT

162364

Figure 31. 45-Caliber Pistol at Waist, Thermlscope

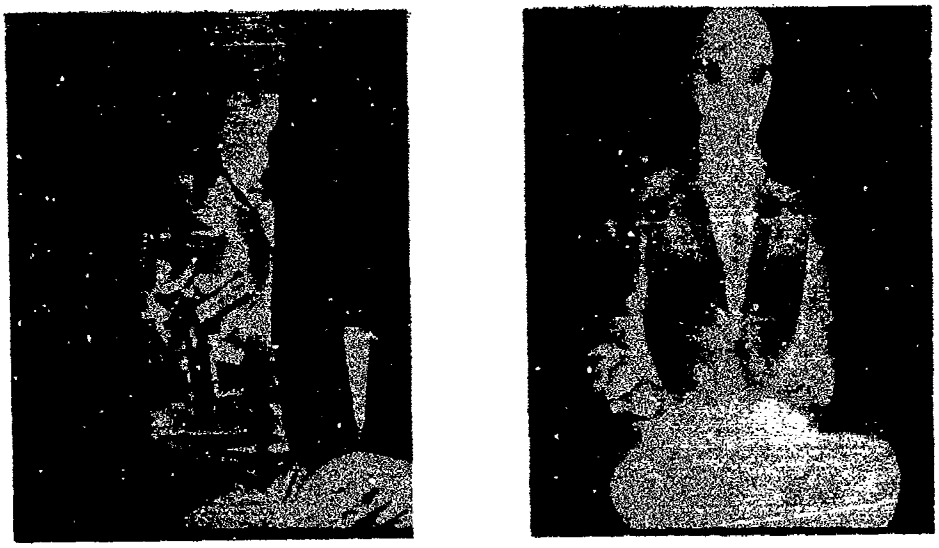

A. COAT OPEN SHOWING PISTOL

B. NORMAL THERMISCOPE CONTRAST

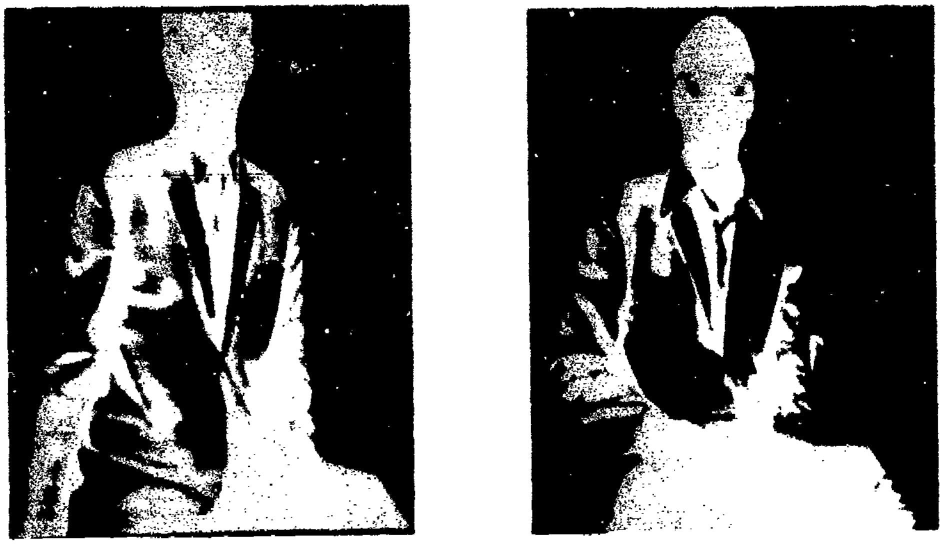

C. HIGH CONTRAST (BRIGHT)

D. HIGH CONTRAST (DARK)

162365

Figure 32. 45-Caliber Pistol Under Suit Coat, Thermiscope

A. NO WEAPONS

B. .45-CALIBER PISTOL IN RIGHT CHEST SUIT POCKET

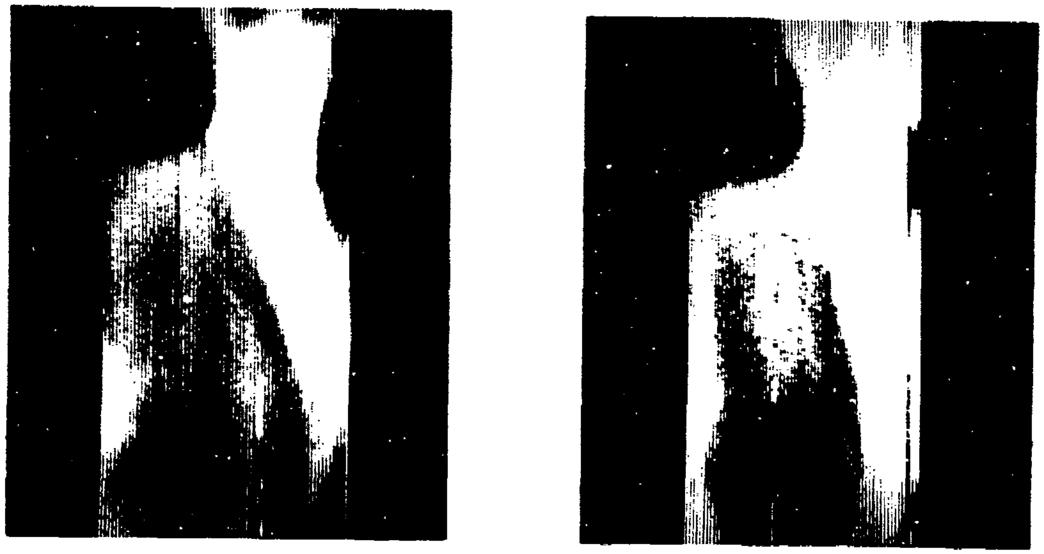

C. SUIT COAT, NO WEAPONS, GaAs, FAST SCAN

D. .45-CALIBER PISTOL IN RIGHT CHEST SUIT POCKET GaAs FAST SCAN

147528

Figure 33. 45-Caliber Pistol Under Suit Coat, GaAs Detector

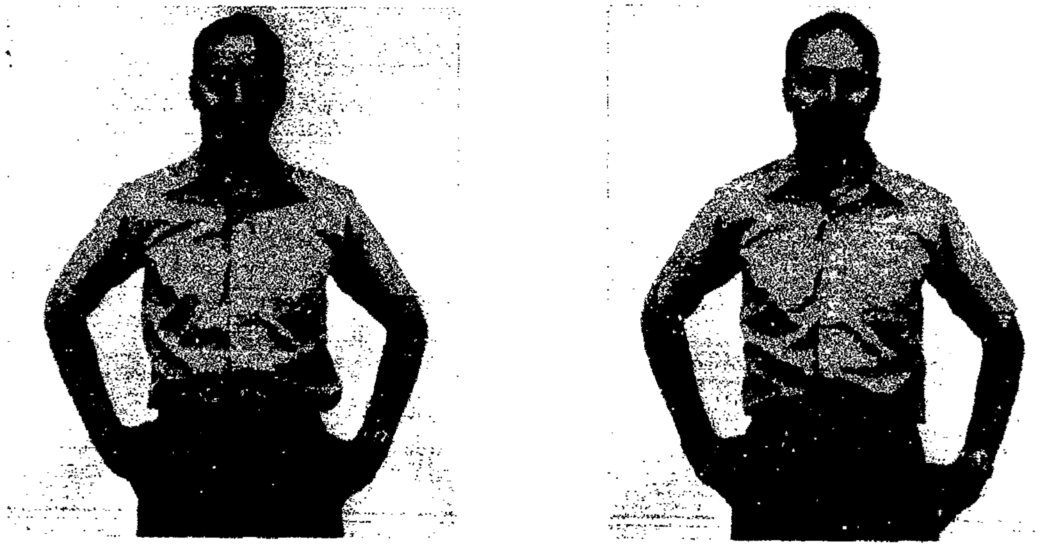

A. NO WEAPONS

B. .45- CALIBER PISTOL IN BELT AT RIGHT WAIST, COVERED BY SHIRT AND TROUSERS

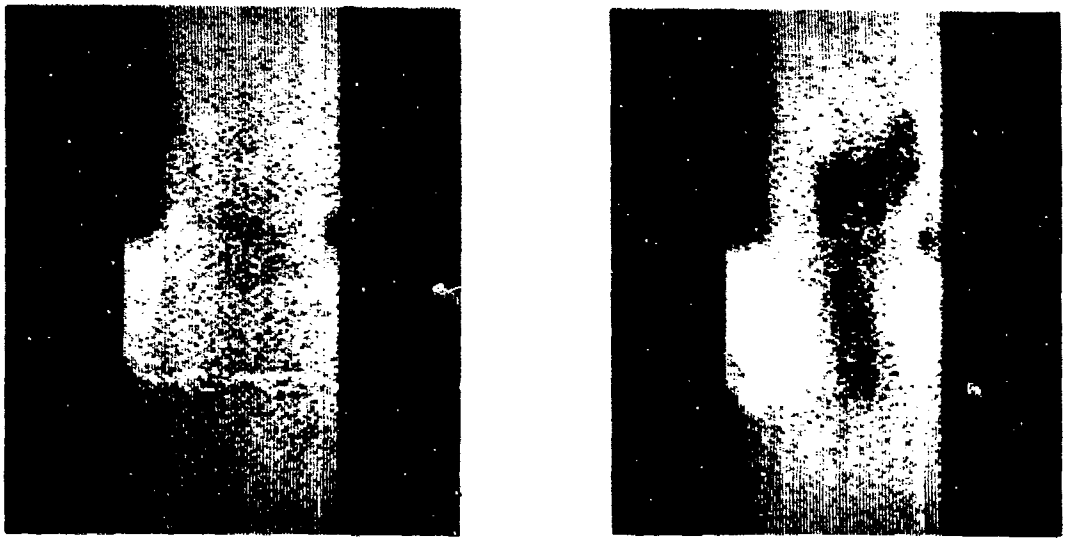

C. WAIST VIEW, NO WEAPON, GaAs, FAST SCAN

D. WAIST VIEW SHOWING .45-CALIBER PISTOL COVERED WITH SHIRT AND TROUSERS. GaAs, FAST SCAN

147529

Figure 34. 45-Caliber Pistol Under Shirt and Trousers, GaAs Detector

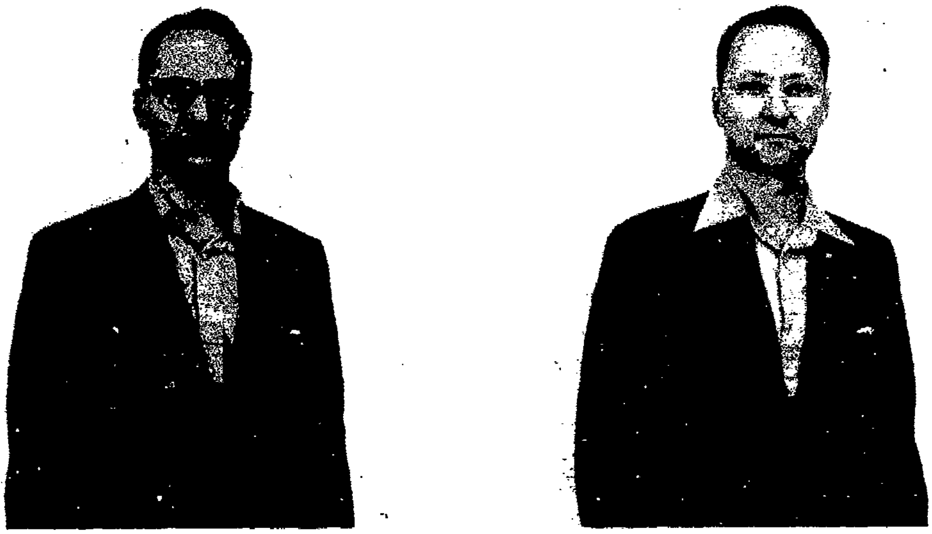

A. NO WEAPONS

B. .45 CALIBER PISTOL IN RIGHT CHEST SUIT POCKET

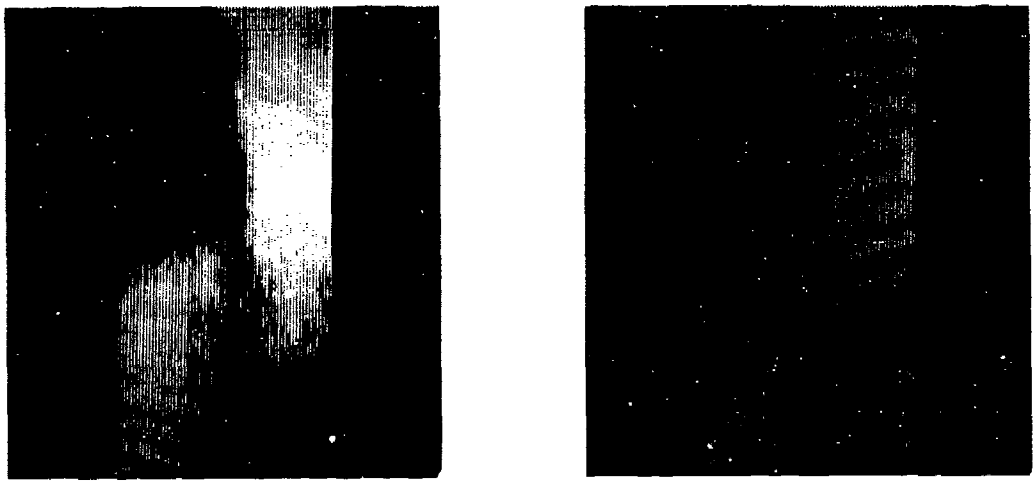

C. SHOULDER VIEW WITH NO WEAPON

D. .45 CALIBER PISTOL UNDER SUIT COAT

1 52366

Figure 35. .45-Caliber Pistol under Suit Coat InSb Detector

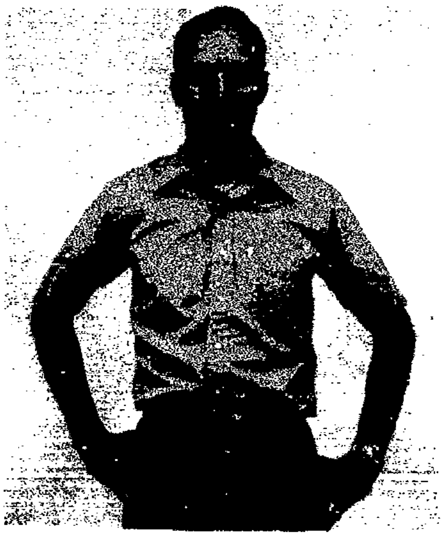

A. .45–CALIBER PISTOL IN BELT AT RIGHT WAIST, COVERED BY SHIRT AND TROUSERS

B. WAIST VIEW SHOWING .45–CALIBER PISTOL COVERED WITH SHIRT AND TROUSERS InSb

162367

Figure 36. 45-Caliber Pistol Under Shirt and Trousers, InSb Detector

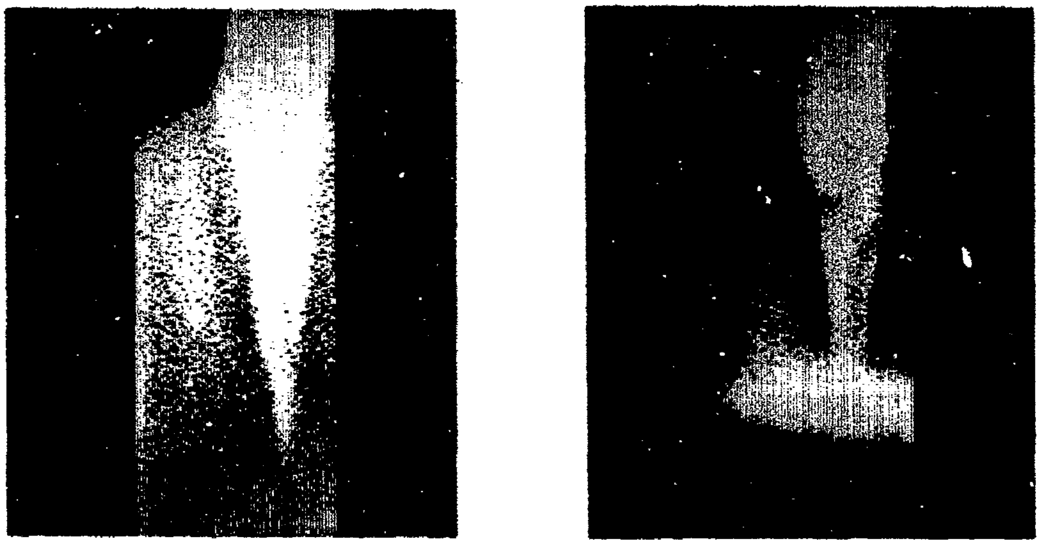

A. IMAGE OF SUIT COAT, GaAs SENSOR

B. IMAGE OF HAND IN FRONT OF SUIT COAT, GaAs SENSOR

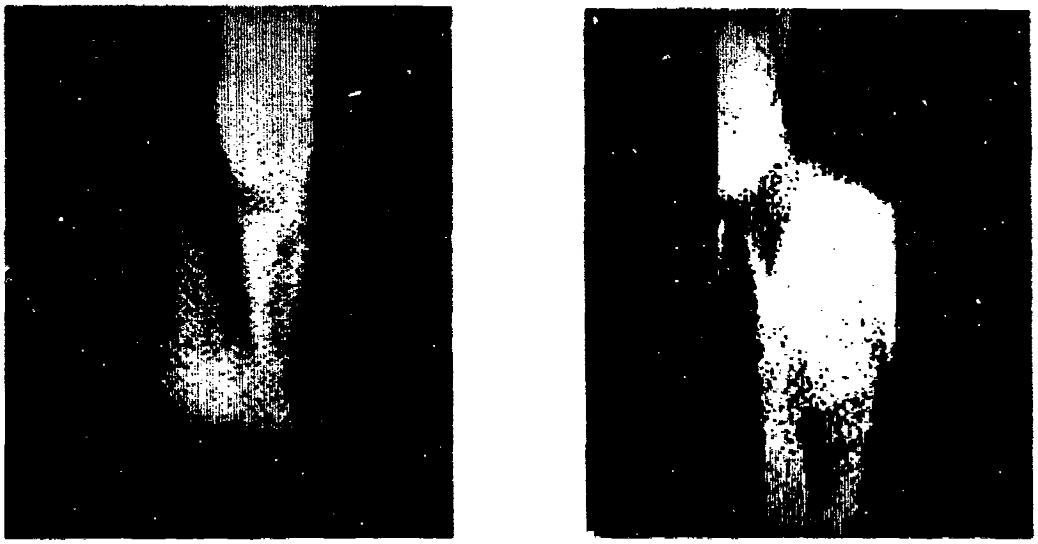

C. IMAGE IMMEDIATELY AFTER REMOVAL OF HAND, SHOWING HAND PRINT ON SUIT COAT, GaAs SENSOR

D. .22-CALIBER PISTOL IN SHIRT POCKET, GaAs SENSOR

147532

Figure 37. Thermal Effects of GaAs Detector

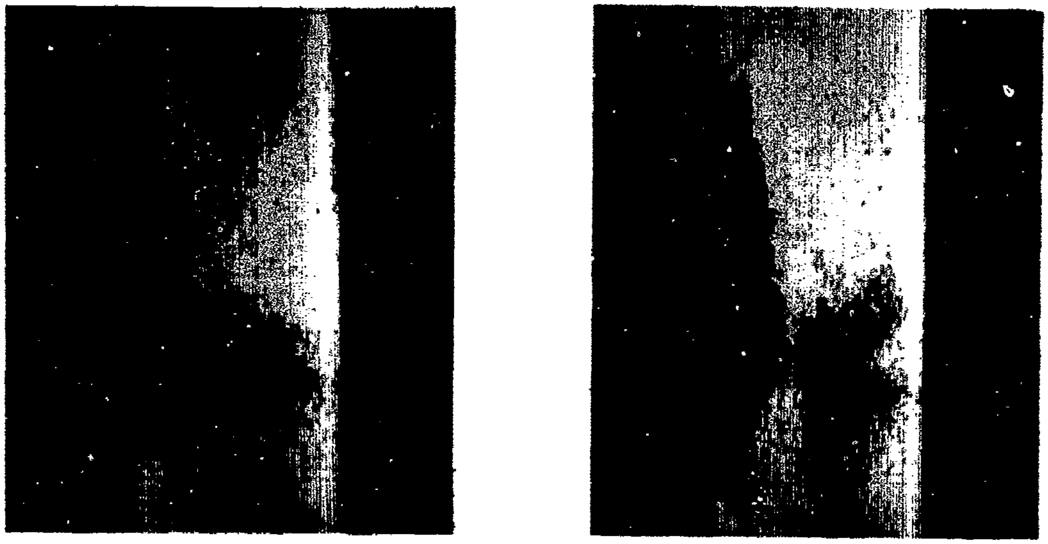

A. WAIST VIEW, NO WEAPON

B. WAIST VIEW SHOWING .45–CALIBER PISTOL COVERED BY SHIRT AND TROUSERS, GaAs SENSOR

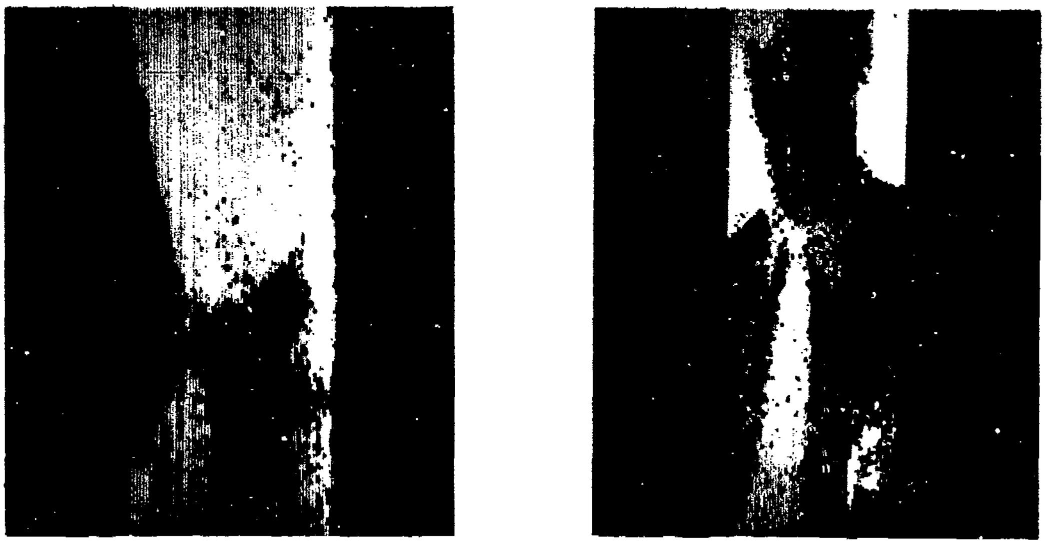

C. WAIST VIEW SHOWING .45–CALIBER PISTOL COVERED BY SHIRT AND TROUSERS, GaAs SENSOR

D. .22–CALIBER PISTOL IN LEFT SHIRT POCKET, GaAs SENSOR

147533

Figure 38. Concealed Weapon Photographs Taken with GaAs Detector

shirt are further evidence of the relatively low transmissivity of multiple layers of cloth at 0.285 millimeter. Images 38A, B, and C show how the contrast and sensitivity can be changed to produce a different picture of the same object.

The pictures of Figure 39 are self-explanatory except 39D which was made with an early InSb detector where signal to noise is poor. The gun is at an angle with the handgrip pointed toward the shoulder.

3. Enhanced Background

Some images were made with objects placed against a heated pad as a background instead of against a person. When the electric pad was set at about 25°C above room temperature, the temperature contrast was about twice that of a person in room temperature surroundings. This would simulate the effect of improving the NET of the sensors by about a factor of two. The picture sequences in Figures 40 (GaAs sensor) and 41 (InSb sensor) were repeated as a standard check of performance after changes were made in the sensors. The cloth layers used were

100 percent rayon suit lining

100 percent wool, 6.7 oz/yd^2, dark brown suit material

100 percent wool, 15.9 oz/yd^2, black overcoat material.

The image quality produced by the InSb detector is still not as good as that of the GaAs and the resolution is not as good by about the ratio of the wavelengths. However, as would be expected, the transmission through multiple layers of cloth degrades the image much more rapidly at the short wavelength of GaAs (0.285 mm) than at the longer InSb wavelength (>0.6 mm).

The images of Figure 42A and B were made to show the transparency of some plastics. Unfortunately, leather is relatively opaque at 0.285 millimeter. Figure 42C shows the heating effect on the composition pistol grip and the reflection of the heating pad by the rounded sides of the grip making it appear narrower in relation to the rest of the weapon. The handgun in Figure 42D was wrapped completely in a cardboard box and wrapping paper.

4. Illumination Tests

A few tests were conducted to determine the effects of target area illumination with very weak, broadband, submillimeter radiation. Since no coherent sources were available, a filtered blackbody source was devised by reflecting the energy from an incandescent 1,000-watt heater coil onto the target area with a 100-mesh copper screen. This screen effectively eliminated radiation with wavelengths less than about 400 μm by transmission or by diffuse reflection. Only tens of microwatts of longer wavelength radiation were specularly reflected onto the target area. The heater was completely shielded from any straight line path to the target.

As expected, only metal target surfaces that were so oriented as to specularly reflect radiation into the imaging system could be detected. In effect, these surfaces and the copper screen formed a double-mirror reflection of the submillimeter radiation from the heater into the imaging system.

Usually, only two or three bright spots could be seen for each gun orientation (Figure 43A). Sometimes, the pistol could be oriented in such a way that larger areas reflected

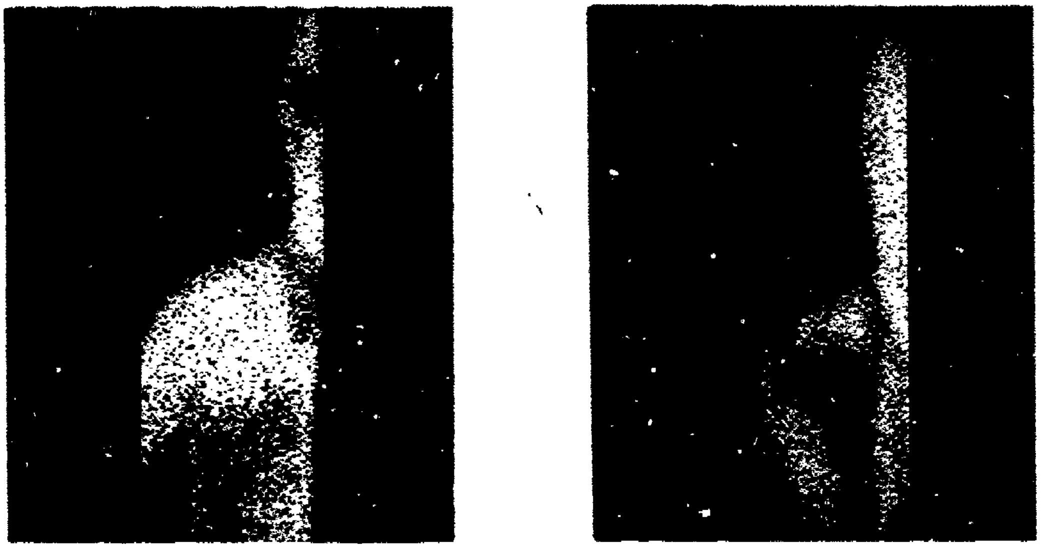

A. .45-CALIBER PISTOL COVERED BY SHIRT AND T-SHIRT, GaAs SENSOR

B. .45-CALIBER PISTOL BETWEEN SHIRT AND T-SHIRT (ARM IN COAT SLEEVE), GaAs SENSOR

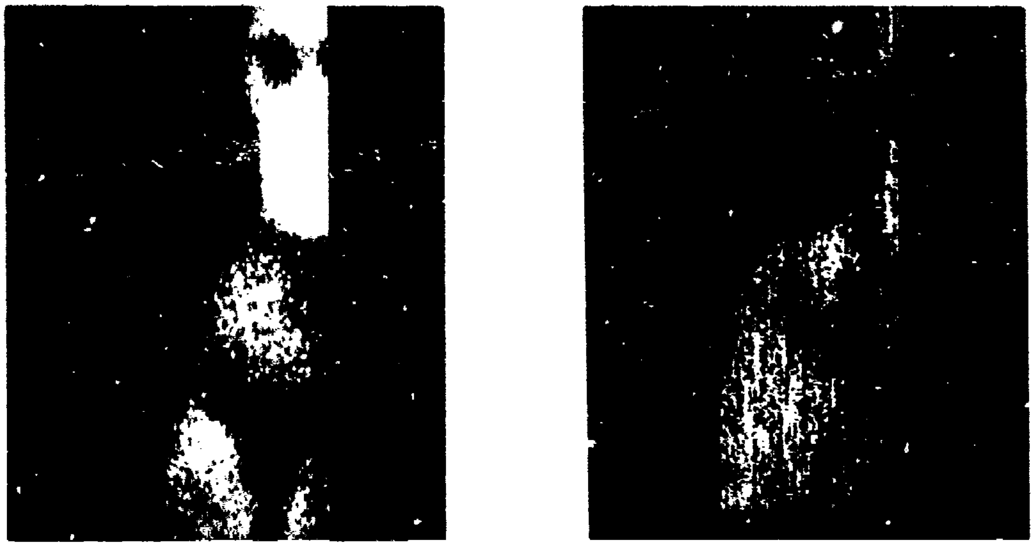

C. .45-CALIBER PISTOL COVERED WITH SINGLE LAYER OF SUIT COAT PLUS LINING, GaAs SENSOR

D. .45-CALIBER PISTOL COVERED BY CORDUROY JACKET, TAKEN OUT OF DOORS, InSb FAST SCAN

147534

Figure 39. Miscellaneous Photographs of Concealed Weapons

A. .45-CALIBER PISTOL ON HEATING PAD (25°C ABOVE AMBIENT) NO COVER, GaAs SENSOR

B. SAME AS A, BUT COVERED BY ONE LAYER OF SUIT CLOTH AND ONE LAYER OF LINING, GaAs SENSOR

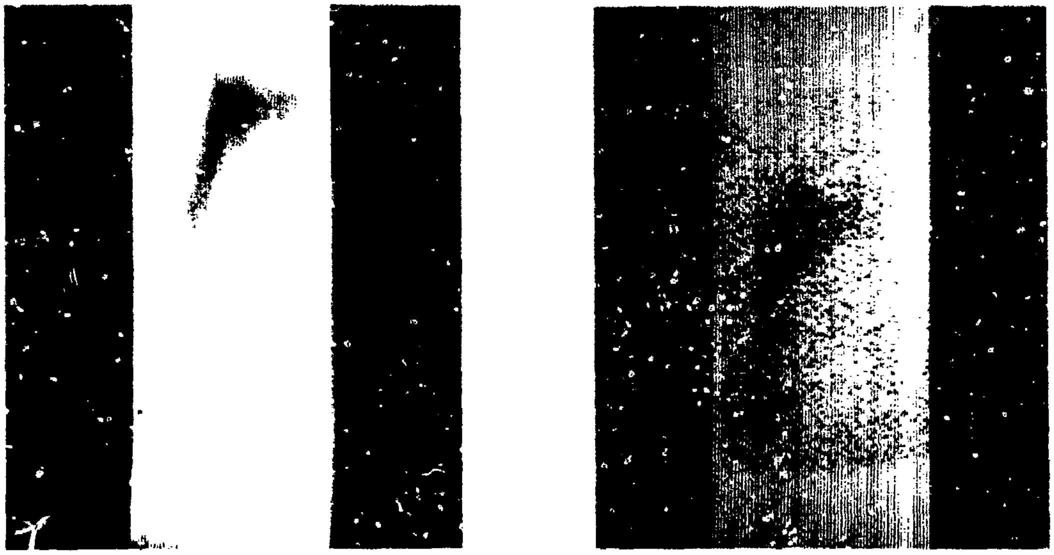

C. SAME AS A, BUT COVERED BY TWO LAYERS OF SUIT CLOTH AND ONE LAYER OF LINING

D. SAME AS A, BUT COVERED BY TWO LAYERS OF SUIT CLOTH, ONE LAYER OF OVERCOAT CLOTH, AND ONE LAYER OF LINING, GaAs SENSOR

147535

Figure 40. GaAs Detector Photographs Showing Concealed Weapon Covered by Various Layers of Clothing

A. .45-CALIBER PISTOL ON HEATING PAD (25°C ABOVE AMBIENT) NO COVER, InSb SENSOR

B. SAME AS A. BUT COVERED BY ONE LAYER OF SUIT CLOTH AND ONE LAYER OF LINING, InSb SENSOR

C. SAME AS A. BUT COVERED BY TWO LAYERS OF SUIT CLOTH AND ONE LAYER OF LINING, InSb SENSOR

D. SAME AS A. BUT COVERED BY TWO LAYERS OF SUIT CLOTH, ONE LAYER OF OVERCOAT CLOTH, AND ONE LAYER OF LINING, InSb SENSOR

147536

Figure 41. InSb Detector Photographs Showing Concealed Weapon Covered by Various Layers of Clothing

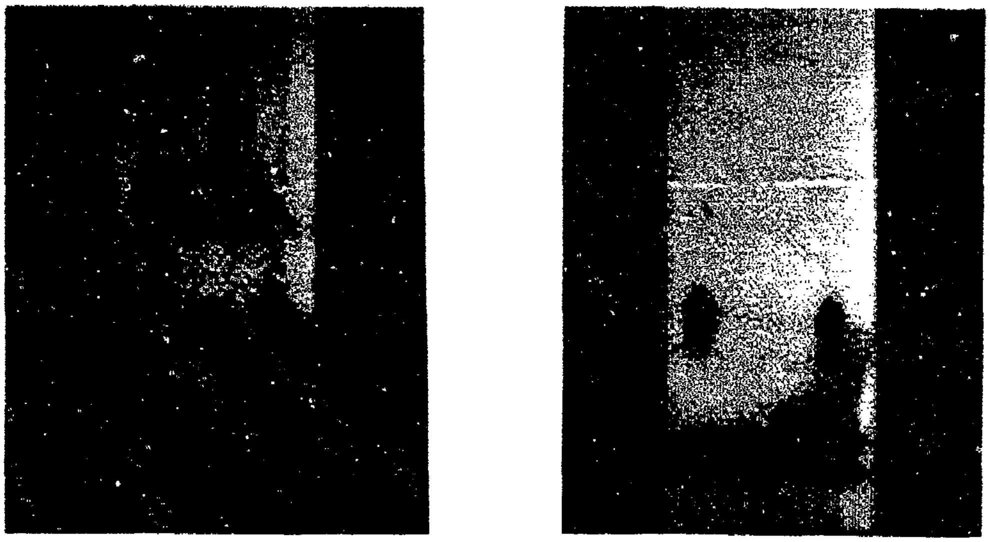

A. .45–CALIBER PISTOL IN PLASTIC LUNCH BOX AGAINST HEATED PAD, GaAs SENSOR

B. .45–CALIBER PISTOL IN PLASTIC LUNCH BOX AGAINST HEATED PAD, GaAs SENSOR

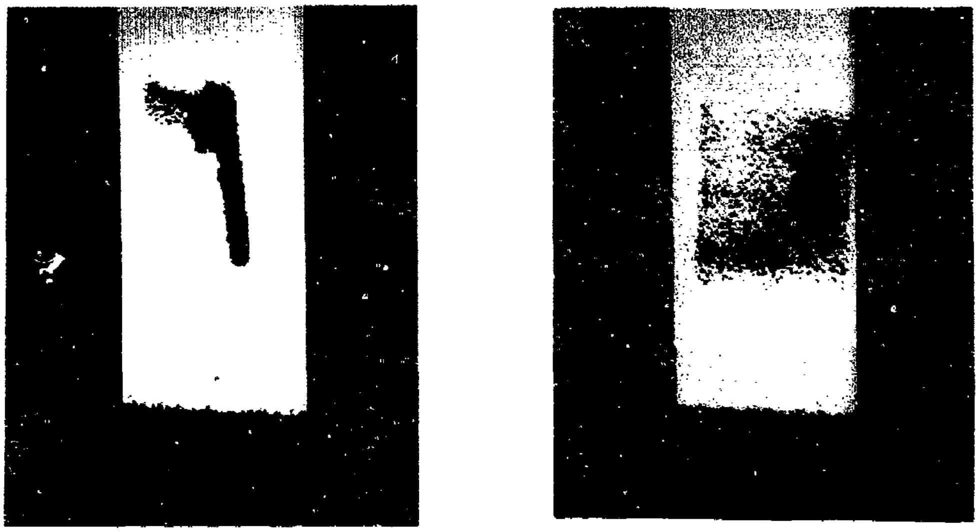

C. .45–CALIBER PISTOL ON HEATED PAD WITH NO COVER, GaAs SENSOR

D. .45–CAL PISTOL WRAPPED IN CORRUGATED CARDBOARD BOX AGAINST HEATED PAD, GaAs SENSOR

147537

Figure 42. Miscellaneous Photographs Taken with a GaAs Detector

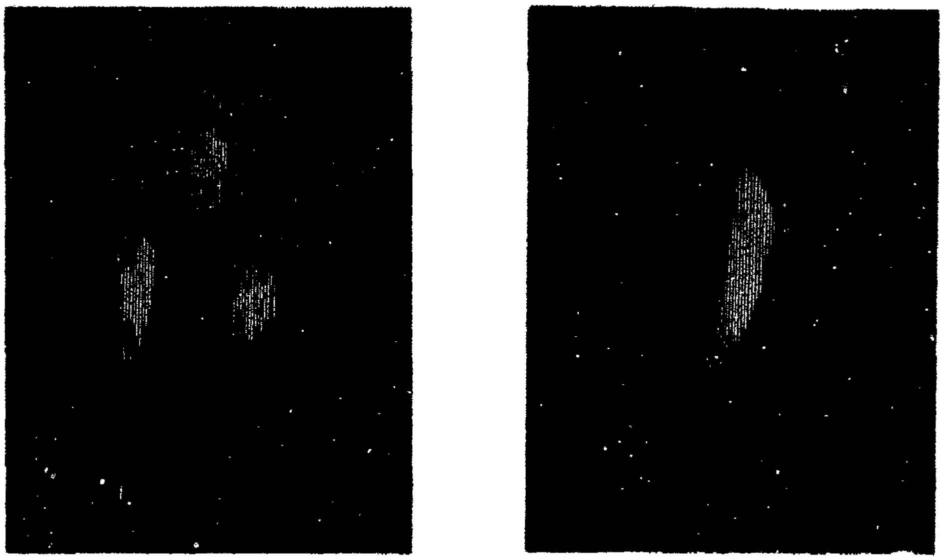

A. SPECULAR REFLECTIONS FROM SEVERAL SPOTS ON A PISTOL CONCEALED BY A COAT

B. REFLECTION OF RADIATION FROM A LARGER AREA OF PISTOL AGAINST WOOD PANEL

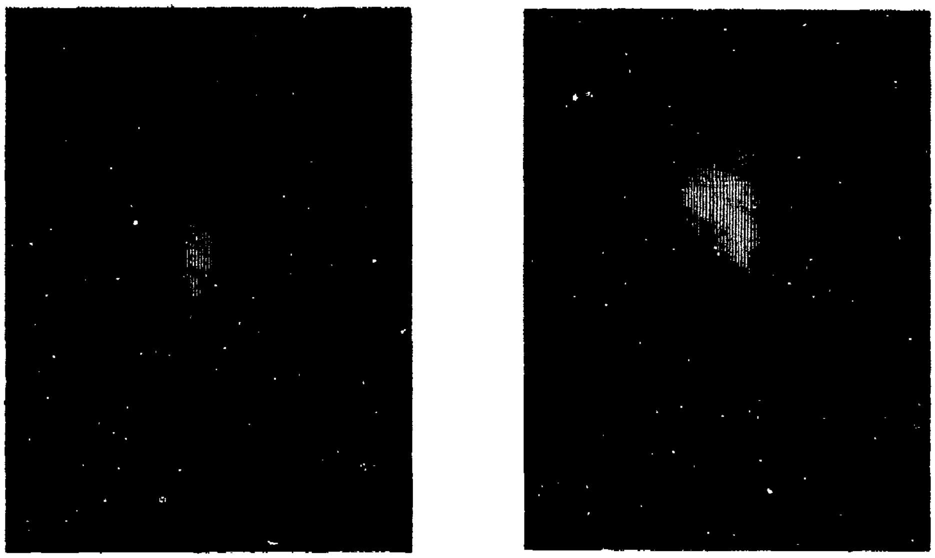

C. SAME AS B BUT WITH SUIT COAT COVERING PISTOL

D. REFLECTION FROM PISTOL IN WHICH COMPOSITION PISTOL HANDLE HAS BEEN REPLACED BY FLAT METAL PLATE AND COVERED WITH SUIT COAT. ORIENTATION WAS CAREFULLY SET TO PRODUCE MAXIMUM SPECULAR RETURN

162368

Figure 43. Active System Imagery Made with Illumination from a Filtered Blackbody

specularly as in Figure 43B, C, and D. In a real-time system with movement of the target, the transmitter, or the source, the metallic object would "scintillate" with many bright spots appearing over much of the surface.

It is significant that even with the small amounts of power available, no difficulty was experienced in penetrating cloth. The same pattern could be detected through two coats, plus several additional layers of cloth. Each additional cover reduced the "bloom" of the spots but the pattern could be restored by increasing contrast and sensitivity.

B. Performance Characteristics

The optical system was designed to be diffraction-limited for a wavelength near 0.5 millimeter. Since the InSb detectors available happened to have peak response between 0.7 and 0.8 mm, the resolution was necessarily less than anticipated. The Airy disc was now larger than the detector and there was a significant loss in sensitivity. The optics were altered to focus the lost energy on the detector. Tests were conducted to determine the actual system resolution and temperature sensitivity with each of the sensors.

1. Improved Optics for InSb Detector

Since the detector wavelength response and the collecting mirror diameter determine system resolution, this could not be easily improved. However, the collection efficiency was more than doubled by moving the detector closer to the Dewar window and by using lenses to reduce the effective system focal length.

Teflon and polyethylene are highly transparent to submillimeter radiation and have refraction indices of 1.36 and 1.5, respectively. Therefore aplanatic lenses can be conveniently made from these materials. The cone of rays created by the collector may be further converged by aplanatic lenses without introducing any additional aberration.

The final configuration used for the InSb detector is very similar to the GaAs sensor design (Figure 7) except that the detector is closer to the window and an aplanatic Teflon lens has been placed where the filter is. In addition, another aplanatic lens, made of polyethylene and about 3 inches in diameter, has been placed outside the window. This combination of lenses should have reduced the blur circle by a factor of 2.3. The sensitivity of the InSb system was improved by more than a factor of 2.

2. Resolution

The system resolution, α, with the GaAs sensor should depend upon the detector size, d, and the distance between the detector and collector, L; $\alpha = d/L$. The spatial resolution on the target would be

$$\delta = \alpha R = dR/L$$

where R is the object distance. Both detectors are about 0.17 cm square, L = 100 cm, and R = 300 cm. Therefore, δ ideally should be 0.5 cm. However, considering that this is near the diffraction limit and that the diagonal dimension of the detector is near 0.24 cm, δ would be expected to be slightly larger. The images in Figure 44A and B are metal strips on a heating pad.

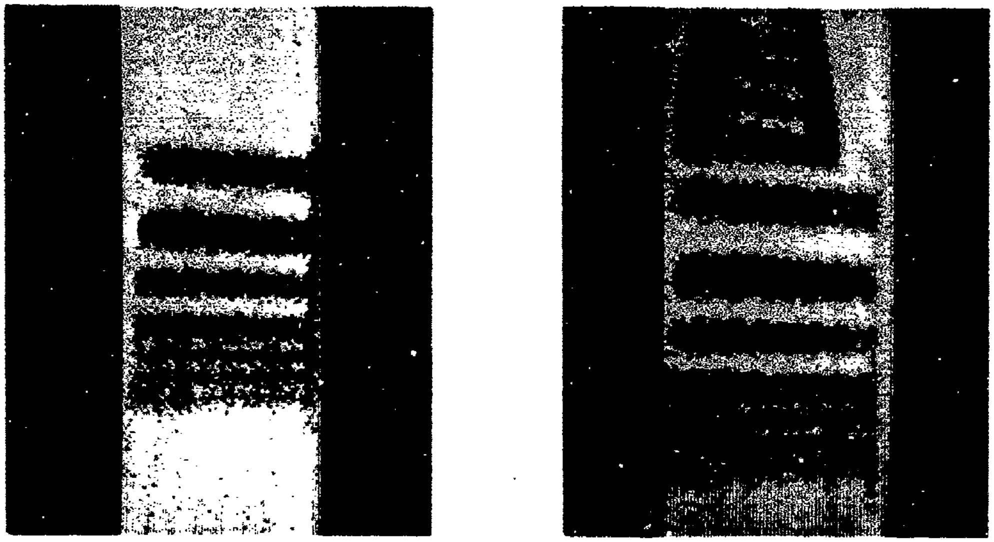

A. METAL STRIPS ON HEATED PAD, GaAs SENSOR

B. METAL STRIPS ON HEATED PAD, GaAs SENSOR

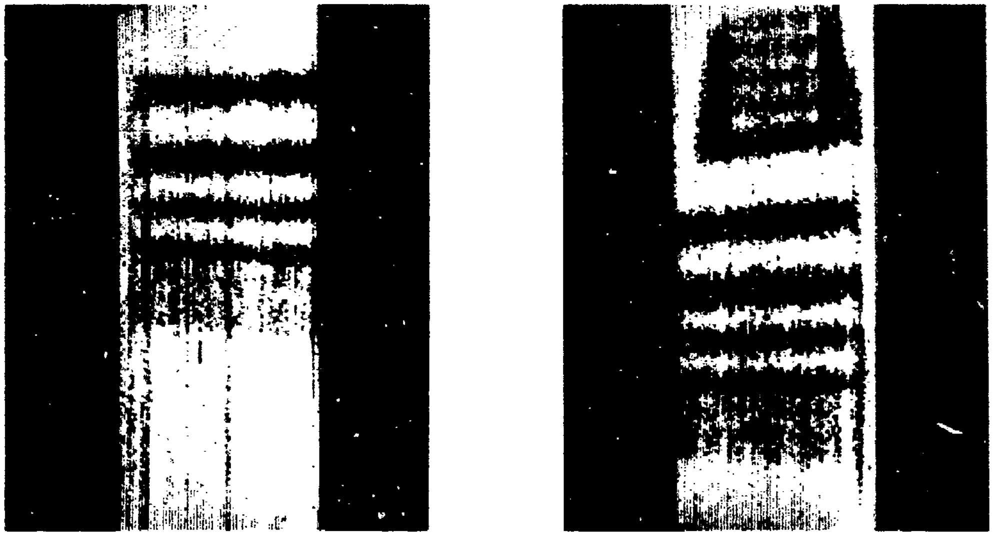

C. METAL STRIPS ON HEATED PAD, InSb SENSOR

D. METAL STRIPS ON HEATED PAD, InSb SENSOR

147538

Figure 44. System Resolution for Each Detector

The long strips, from top to bottom, are pairs 3 cm, 2 cm, 1 cm, and 0.5 cm in width, separated by distances equal to their widths. The 0.5-cm strips on the bottom are unresolved and appear as a single strip similar to the two 1-cm strips immediately above. The top pattern in Figure 44 is a metal foil with 1.2-cm slots which are separated by 1.2 cm. It appears, then, that the limit of resolution for the GaAs sensor is between 0.5 cm and 1.0 cm at a distance of 300 cm, or the angular resolution is between 1.7 and 3.3 mrad.

With the InSb detector, the system is strictly diffraction-limited. The angular size of the first dark ring of the Airy disc is

$$\alpha = 2.44\ \lambda/D \text{ radians}$$

Eighty-four percent of the energy of the diffraction pattern falls in this cone, so this should be a conservative value for resolution. About 63 percent of the energy falls in one-half of this cone and should be the limit for resolution of two objects, even with good contrast. Therefore, at a wavelength of 0.75 mm and the system aperture, $D = 33.5$ cm, the angular resolution should be between 2.7 and 5.5 mrad. At 3 meters, the spatial resolution would be between 0.8 and 1.6 cm. Figure 44C and D are images of the same objects as in A and B. The 1.2-cm slots in the metal foil are resolved, but the 1.0-cm strips are not distinguishable in the noise. The system resolution with the InSb sensor would appear to be about 4 mrads or a little more than a centimeter at 3 meters.

3. Atmospheric Transmission

Atmospheric absorption in the submillimeter portion of the spectrum is dominated by the water vapor rotational transitions. Water vapor content in the air can vary from near zero to 30 gm/m^3, however, the usual concentration is in the range of 5 to 20 gm/m^3. For instance, if the relative humidity is 50 percent and the temperature 72°F, the water vapor content is about 10 gm/m^3. A recent measurement[14] of water vapor absorption in the submillimeter is shown in Figure 45. Data from Sheppard and others has been replotted in terms of the absorption coefficient, α, where the intensity of radiation at a distance x in the vapor is

$$I = I_o e^{-\alpha \rho x}$$

where ρ is the density of the water vapor in the path. For $\alpha = 10^{-2}$ m^2/gm, the radiation would be reduced to approximately 37 percent of its initial value after passing through 10 meters of an atmosphere with a water vapor content of 10 gm/m^3.

Except for three relatively narrow absorption peaks, the absorption is somewhat less than this at wavelengths longer than 280 μm. To the extent that radiation in the 240- to 280-μm band is included in the acceptance band of any system, there will be a reduced signal-to-background ratio. For a system operating in any portion of the submillimeter, the importance of sharp cutoff filters on the short wavelength side of the operating bandpass is obvious. Figure 46 shows the water vapor absorption coefficient to longer wavelengths for a typical atmosphere with 7.5 g/m^3 of dissolved water. The agreement between these measurements and those of Figure 45 is good, with slightly better resolution in the data of Sheppard. Therefore, the windows are a little clearer in the Sheppard absorption measurements.

The range through the atmosphere should be considerably greater for the spectral band of the InSb detector than for the GaAs detector. Several tests were made using a parabolic lens

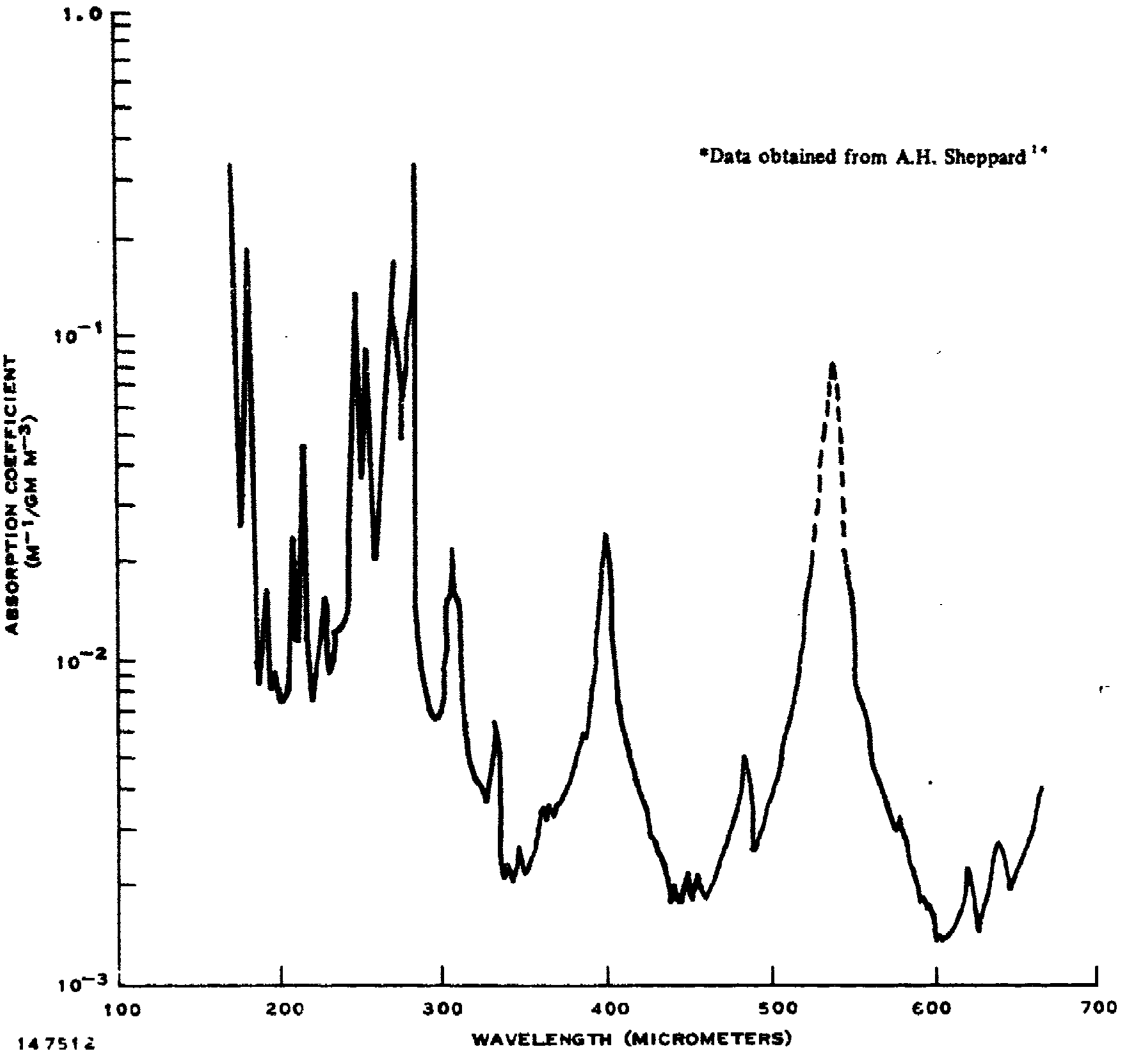

Figure 45. Water Vapor Absorption

in place of the usual ellipse. Images were taken as a function of distance. For GaAs, the image of a person disappeared at a range of about 40 feet. However, no limit could be established for the InSb detector. The images shown in Figures 47 and 48 were taken using InSb. System resolution was only about 4 milliradians so that the spacial resolution was almost ½ foot at 100 feet and about 4 feet at 1,000 feet, making object recognition difficult in this narrow field of view. However, by blocking portions of the field of view and by adding warm targets, the viewed objects could be clearly established.

Notice that the metal parts of the truck cab in Figures 48A and B appear very cold because, even though painted and dirty, they are very good reflectors of the cold sky at these wavelengths. The windows of the cab appear as hot spots since they have relatively high emissivity and were warm. The rear tire in the picture was still hot from running.

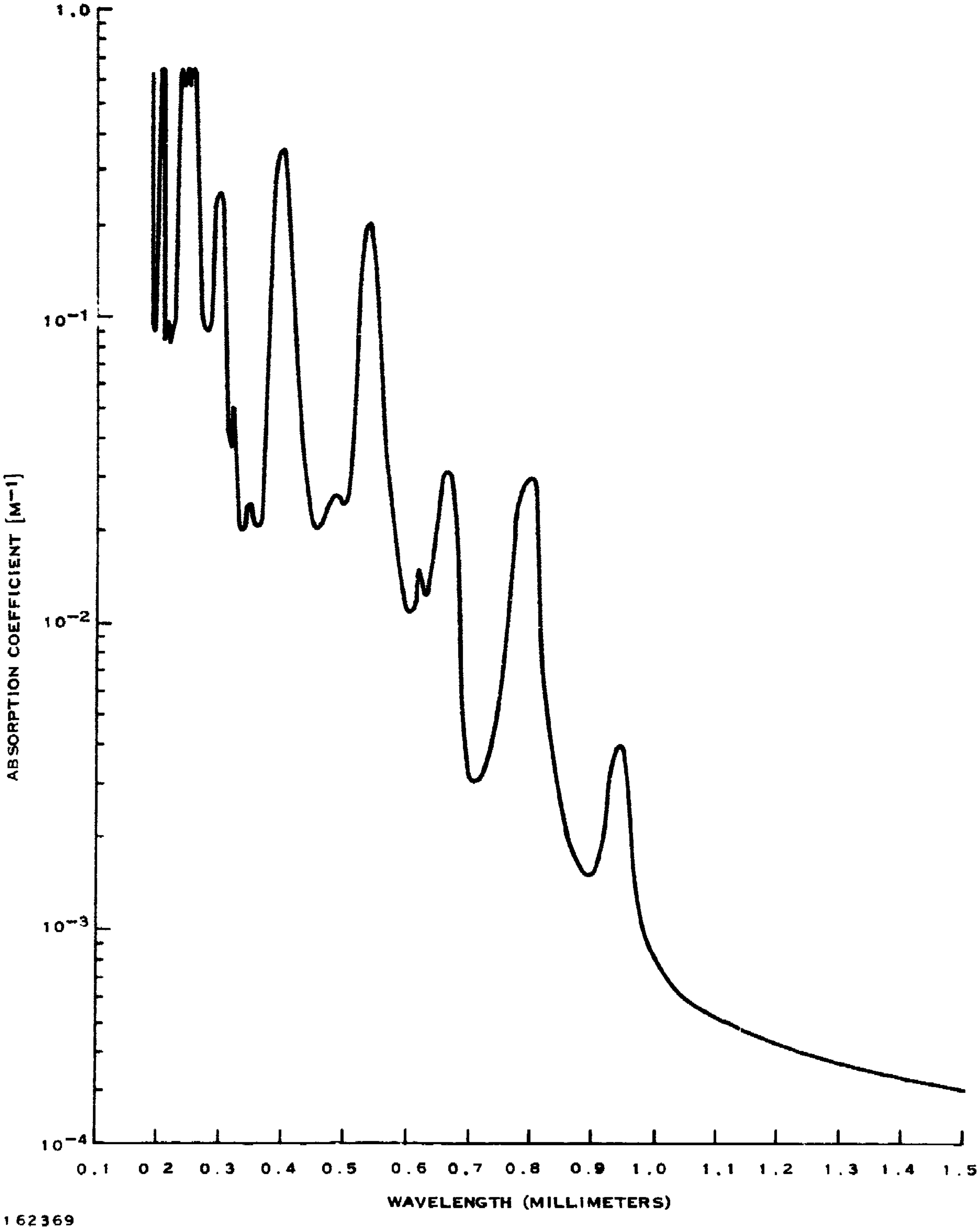

162369

Figure 46. Water Vapor Absorption Coefficient for 7.5 g/m³ Humidity at 760-mm Hg and 20°C

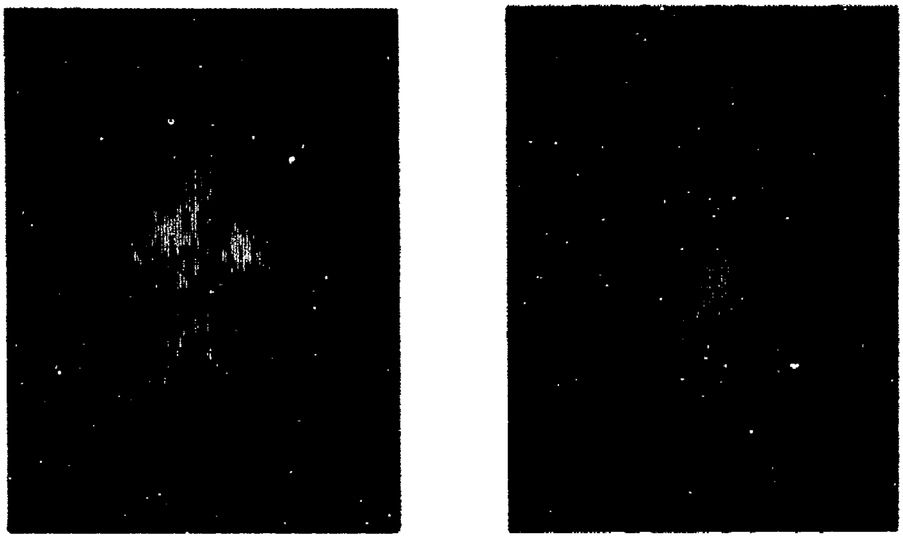

A. MAN AT 20 FEET

B. MAN AT 36 FEET

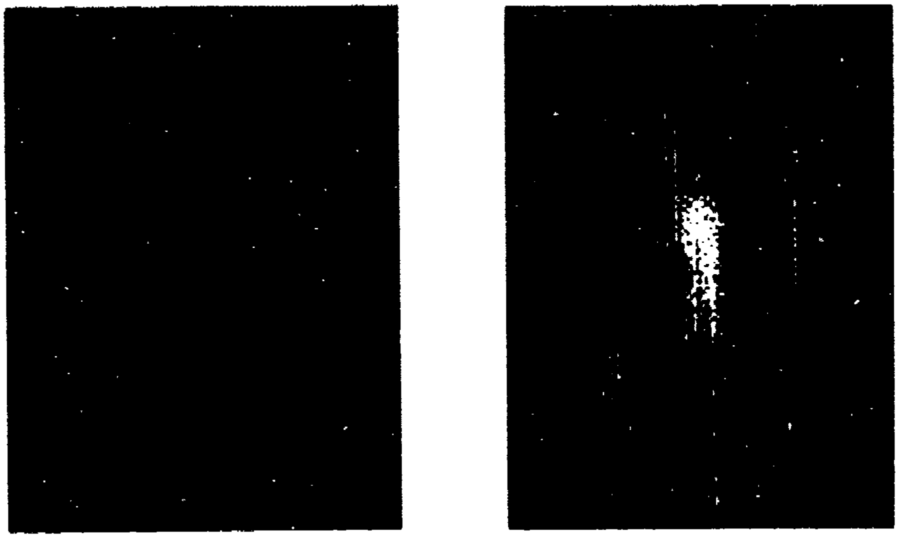

C. MAN AT 48 FEET

D. MAN AT 80 FEET

162370

Figure 47. Photographs of a Man Taken with the InSb Detector, 4-mrad Resolution

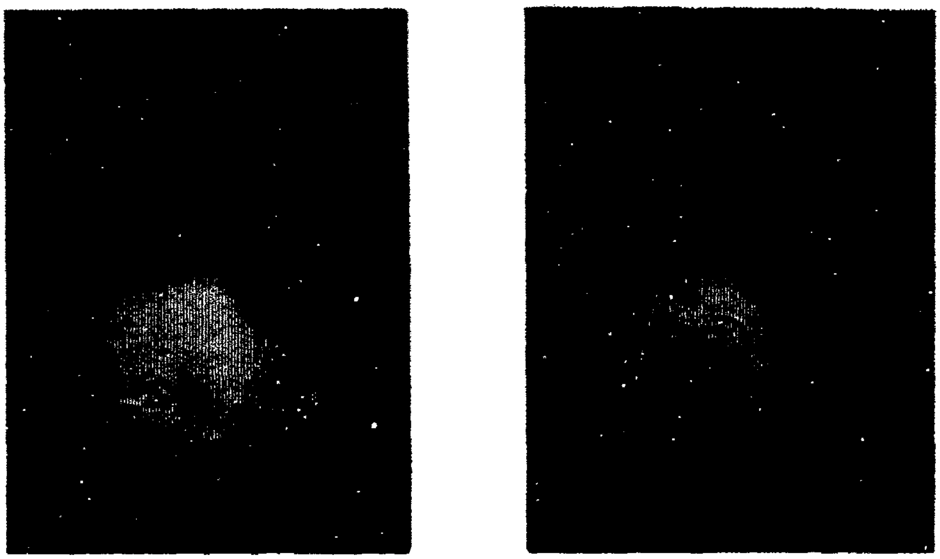

A. BACK OF TRUCK CAB AND REAR TIRE (TWO BACK WINDOWS AND PART OF FLATBED SHOW OVER TIRE)

B. BACK OF TRUCK CAB AND TIRE WITH LESS SENSITIVITY (DISTANCE IS ABOUT 65 FEET)

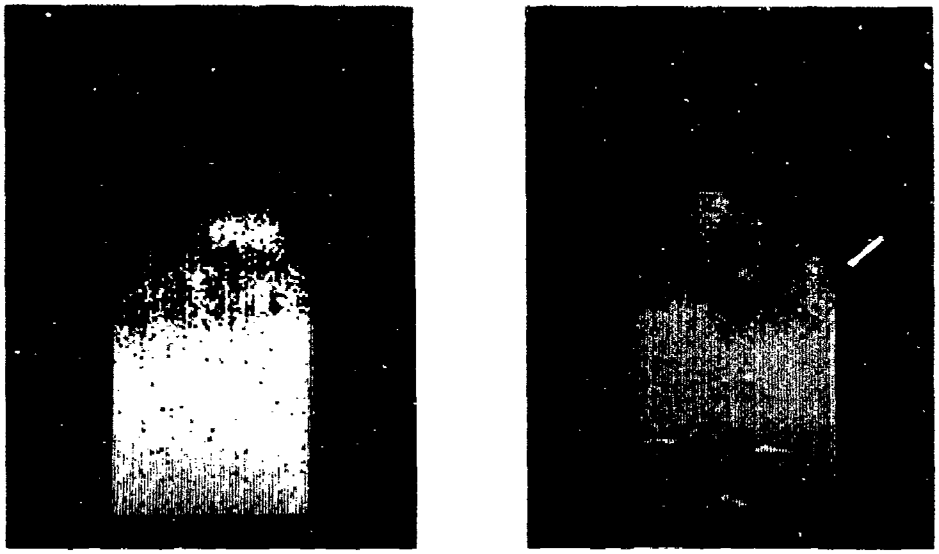

C. SIDE OF BUILDING AT ABOUT 1,200 FEET

D. GABLE END OF BUILDING AT 1,200 FEET

162371

Figure 48. Photographs Taken with InSb Detector, 4-mrad Resolution

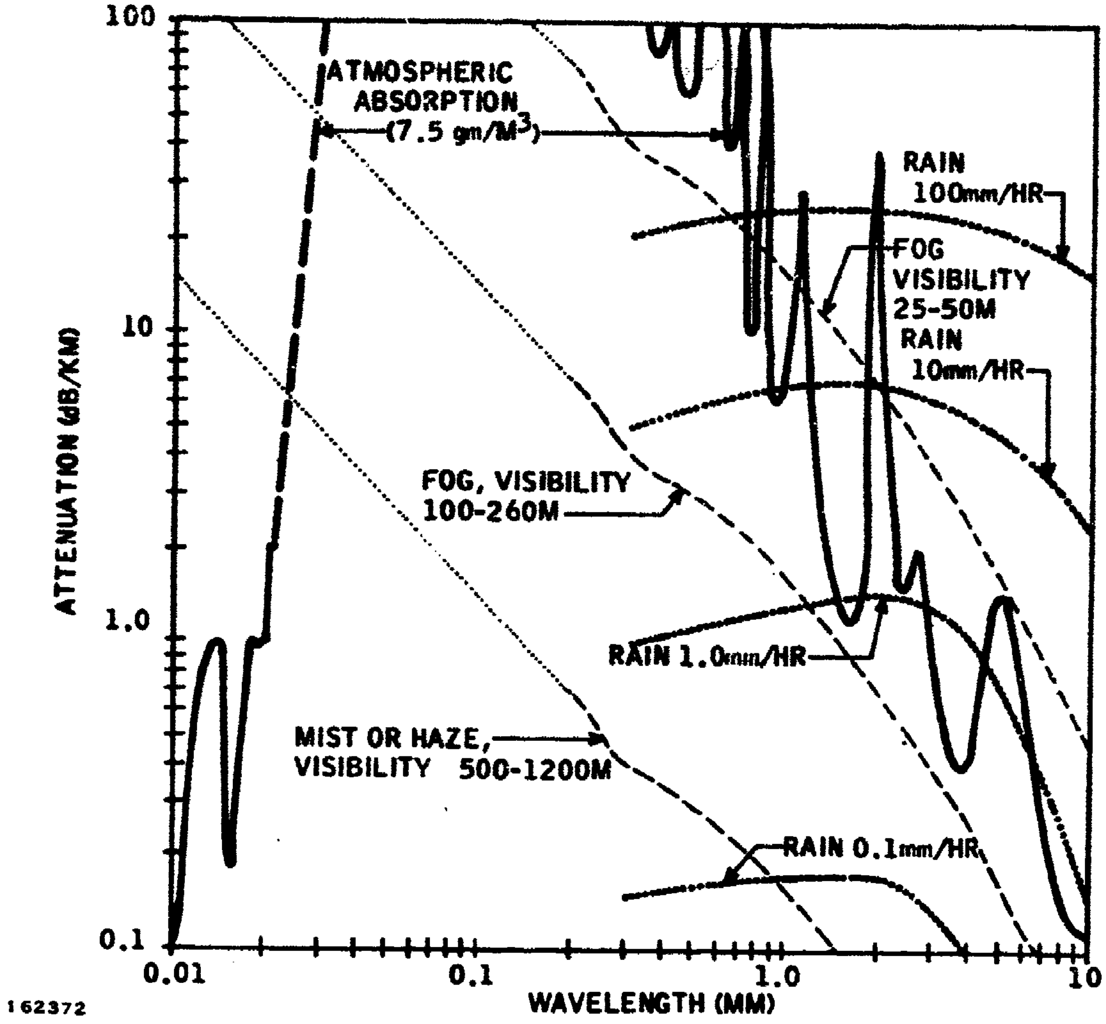

Figure 49. Scattering and Attenuation in Fog and Rain

The lower portion of the pictures of the distant building in Figures 48C and D is part of a hot black asphalt road and parking lot. The cooler spots across the middle of the pictures are the metal parts of cars in a parking lot and only the top portion of buildings 1,200 feet away could be seen above the cars.

Atmospheric transmission varies considerably with particulate matter in the air. Under conditions of fog or haze that severely limit visibility even in the infrared, the submillimeter range may be affected very little (Figure 49). The range-limiting factor in this portion of the spectrum remains absorption except for fairly dense particulates. The absorption is taken from Furoshov,[7] the rain scattering from Rozenberg,[15] and the fog and mist scattering from Platt.[16] These were extrapolated to the infrared and visible on the basis of measurements made by Johnston and Burch.[17]

It is apparent from the figure that where the range allowed by water vapor absorption in the atmosphere is adequate, and resolution for a given aperture is important. submillimeter or millimeter wavelength systems may be the most effective and should show relatively little degradation in low-visibility conditions.

SECTION IV

PERFORMANCE IMPROVEMENT

A. Basic System Concept

The transition from a laboratory instrument for testing feasibility to a piece of useful equipment in the field requires two major operational improvements. The system must give real-time images and it must have an adjustable focus for useful ranges out to 30 meters, or more.

Since the feasibility system uses a single detector, has only a 15-percent duty cycle, and takes a picture in less than 2.4 s, it should not be difficult in principle to extend this to a real-time system approximately 80 times faster. The frame time is reduced in direct proportion to the number of detectors and to the increase in duty cycle. For instance, a system with 25 detectors and a 50-percent duty cycle could present a real-time image with an even narrower electronic bandwidth than is now used. Some of the special problems that must be solved in a real-time system will be discussed in Subsection IV.B.

The question of what constitutes a useful range is more difficult because of the tradeoff between resolution and the physical size of the scanner. If the sensor was made to have peak response at 0.75 mm, then a 1-m collector could have a 1-mrad resolution. At a 10-m distance, the spatial resolution would be 1 cm and sufficient detail would exist to recognize the presence of most weapons. However at 30 m, with a resolution of 3 cm, most objects of interest would show only a fuzzy outline. However, some judgement would still be possible based on the approximate size and location in which it was carried. Illumination of this spot with radiation in the sensor bandpass would highlight a metal object relative to other materials. This is valuable additional information.

Operationally, it appears that such a system would aid a trained observer whose purpose was to determine the probability of a threat from suspicious individuals in a group. The ability to determine from a distance the presence, approximate size, and location of objects concealed in the clothing of a person provides information that cannot be obtained by other means without coming into close proximity to that person.

A similar real-time system focused for a 5-m range would have a spatial resolution of about ½ cm. This could be used in monitoring people passing through a controlled access. In this case, the imaging system would probably be used in conjunction with metal detectors. Again, an operator would interpret the images appearing on the screen whenever a detector indicated the presence of metal objects. As an individual moved through the access corridor, he could be seen from different sides by the use of mirrors. The "mirrors" would need to be no more than metal plates which could be painted. Since the environment can be controlled, it should be possible to enhance the images by placing cold surfaces in appropriate locations or by the use of submillimeter illuminators.

The development of a practical imaging system using submillimeter radiation requires careful consideration of design techniques and material properties from infrared and microwave technologies. The detailed study and design of a real-time imaging system is beyond the scope of this study. However, the subsections which follow will outline some of the problems and potential solutions in such a development.

B. Imaging in Real Time

A general summary of different approaches to a real-time imaging system is given in Table VI. The most practical method appears at this time to be some type of scanned array of detectors. Single-detector systems require very broad electronic bandwidths and usually have lower scan efficiencies. A staring system has high efficiency, low electronic bandwidth, and consequently, an improved sensitivity that might even allow use of higher temperature detectors. The complexity of processing signals from over 10,000 detectors remains a major hurdle in implementing the staring concept. However, studies and development efforts on considerably larger staring systems continue, so that the concept should be reexamined periodically.

TABLE VI. REAL-TIME IMAGING SYSTEMS *

Type	Number of Detectors	Approximate Scan Efficiency (percent)	Maximum Frequency Response	NEP for 10^{-13} W/Hz$^{1/2}$ Detectors	Detector Temperature (Kelvin)
Scanned single detector	1	≈20	3×10^{6} Hz	3×10^{-10} W	<5°
Scanned array	100	25 to 75	1.2×10^{4} Hz	1.1×10^{-11} W	<5°
Scanned array, 2:1 interlace	50	25 to 75	2.4×10^{4} Hz	1.5×10^{-11} W	<5°
Staring	20,000	100	30 Hz	5.5×10^{-13} W	**

*Resolution = 1-mrad, field of view = 5.7° × 11.4°

**May be able to use slower or less sensitive detectors, such as Bolometers (20 to 25°K) or pyroelectric detectors at room temperature.

To demonstrate the feasibility of a real-time imaging system, some of the principle features of one scanner concept will be considered. The parameters of the system are chosen to be

Primary Collecting Mirror, off-axis parabola	
Collector diameter	1.2 m
Effective aperture diameter	1.0 m
Resolution	1.2×10^{-3} radian
Field of view	4 × 8 degrees
Focusing range	7 m to ∞
Image distance	170 cm to 225 cm
F number	1.7
Number of detectors	60
Detector size	2 mm
System bandwidth	4.5 kHz

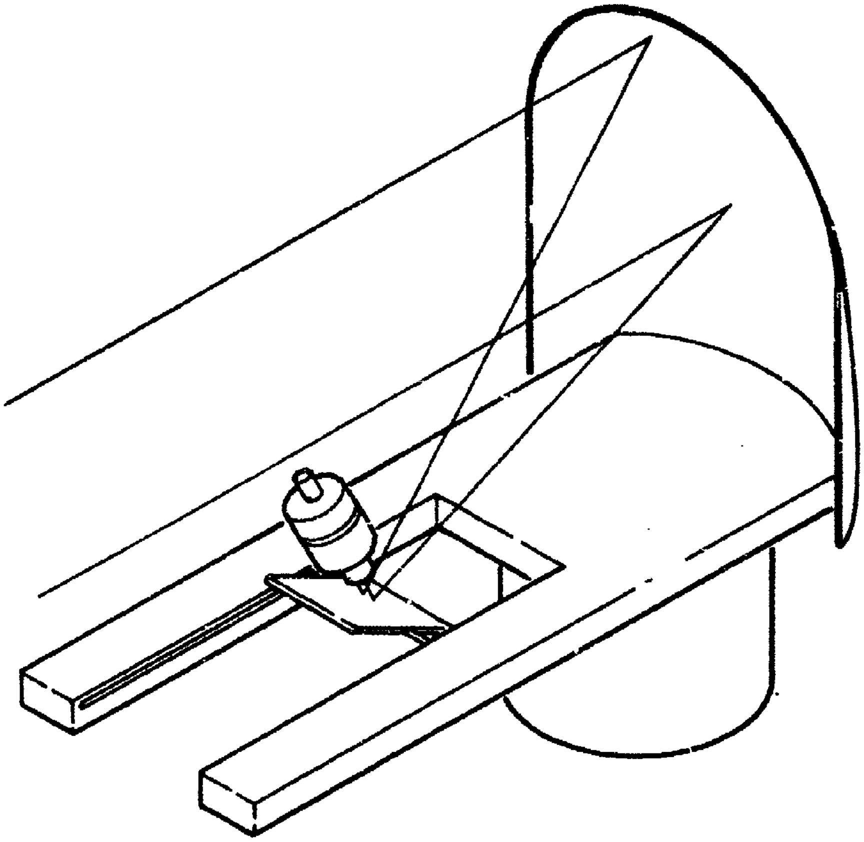

162373

Figure 50. Scanner Using Off-Axis Parabola

Spectral bandpass	0.6 mm to 1.0 mm
Scanning mirror: length	30 cm
width	20 cm
Oscillating frequency	15 Hz
Scan efficiency	80 percent

Figure 50 shows a schematic of the system and Figure 51 is a ray trace showing the oscillating scan mirror and detector array in the two extreme focus positions. Several elements of this scanner present special problems related to the size and operating spectral bandwidth.

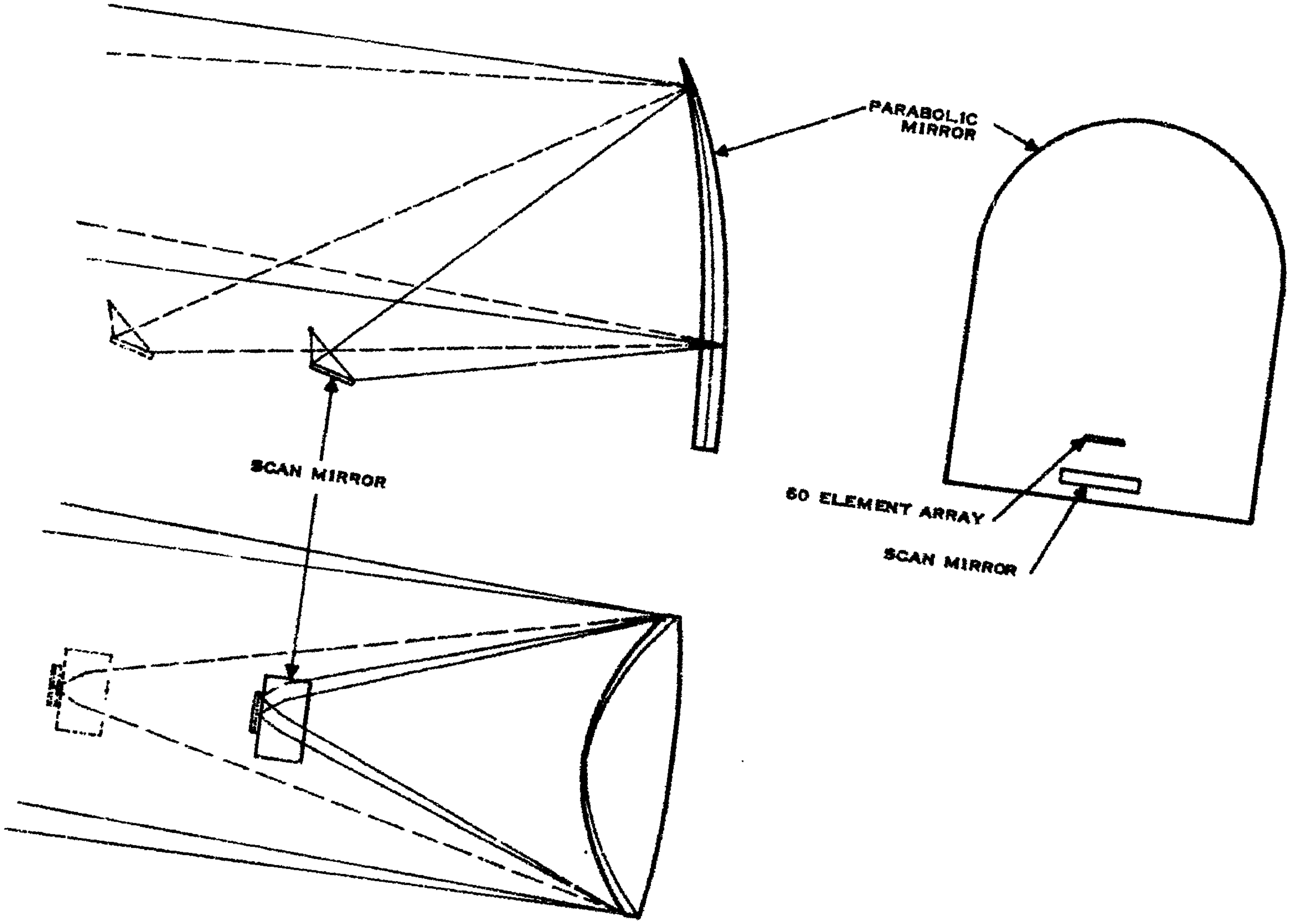

162374

Figure 51. Ray Trace for Sc ror and Focal Plane in 7-Meter and ∞-Focus Positions

1. Primary Mirror

Although the off-axis parabola is very large by infrared standards, it is not unreasonably large for microwave applications. An accuracy of 0.003 inch in surface shape and finish would represent a very good optical finish for 0.8-mm radiation. While this is greater accuracy than required in microwave applications, it does appear to be achievable using the fiberglass and epoxy molding techniques available at Texas Instruments. Computer-controlled machines can be used to make an aluminum mold with somewhat better than 0.003-inch accuracy. Some experimentation with honeycomb or other supportive materials may be required to cast a 1.2-m collector that will retain its shape within tolerance after removal from the mold. The collector would be flashed with a solid metal coating. One advantage of this technique is that the finished collector would be very much lighter than one made entirely from metal.

A parabola has the property that the on-axis blur size is limited only by diffraction. Therefore, the nominal resolution (for $\lambda = 0.8$ mm, $D = 1$ m) limit is

$$\alpha = \frac{1.22\lambda}{D} = 1.0 \times 10^{-3} \text{ radian}$$

Detector spacing will be 2.0 mm so that system resolution focused at infinity (image distance 170 cm) will be about 1.2×10^{-3} radian. The horizontal field of view for 60 detectors will then be about 4 degrees. The detector at the ends of the array will be 2 degrees off-axis. These will have both coma and astigmatism. This system has a 1.7 f-number and therefore,

$$\text{Coma} = \frac{0.0625 \times \theta}{(f\#)^2} = 7.6 \times 10^{-4} \text{ radian}$$

and

$$\text{Astigmatism} = \frac{0.5 \times \theta^2}{(f\#)} = 4.6 \times 10^{-5} \text{ radian}$$

Both of these effects are less than the diffraction limit.

2. Scanning Mirror

The scanning mirror could be rotated or oscillated to sweep the images across the detector array. In this example, an oscillating mirror will be used to avoid the larger size and lower scan efficiency of a multifaceted rotating mirror. Since this system will have a relatively narrow field of view (≅8 degrees vertical), the scan mirror would only have to oscillate about 4 degrees, plus a few degrees, to linearize the scan. To generate 30 frames per second, the oscillation frequency will be 15 Hz, assuming no interlacing. The decision not to interlace increases the difficulty of making the focal plane because of the number of detectors required, but it greatly simplifies the scanning optics.

3. Focal Plane

The most prominent feature of any focal plane used for imaging at these wavelengths is its large size. The criteria for focal-spot diameter (Rayleigh criterion of resolution) is

$$\zeta = \frac{1.22\lambda q}{D}$$

where D = 100 cm is the effective aperture diameter and q is the distance between the collecting mirror and the detector.

The diameter of the first dark ring of the diffraction pattern is twice this value and therefore some radiation will fall in adjacent resolution elements. The 2 mm spacing of detectors in this f# 1.7 system leads to a 1.2×10^{-3} radian resolution which is slightly larger than the diffraction limit of one milliradian for the central wavelength (0.8 mm) with the system focused for large distances. However, the detectors are smaller than the spot size at the near focus, where $\delta = 2.2$ mm. The detectors are of exactly the diffraction limit size for a focus at 10 m. A 60-element array will be 12-cm long. Assembling such an array may be slow and tedious, but should present no insurmountable difficulties since detectors can be tested individually before mounting. To achieve uniformity, the 60 detectors must be selected from a larger set.

Detector cooling will require special design. While a closed-cycle system may be considered in a later version, a specially designed helium Dewar would be used in this arrangement. The design must allow for a long window subtending about 32 degrees at the detector array and must be shaped in such a way that it does not obscure any of the parabolic collector as seen from the detectors. The arrangement shown in Figure 50 will result in a few-percent field of view obscuration for distant focus, but allows a fairly simple Dewar design.

Windows and filters will be easy to fabricate for this spectral band since polyethylene has high transmissivity and black polyethylene effectively filters out all visible and near-infrared radiation.

4. Electronics and Display

At present, it seems that the best InSb detectors will have operating resistances in the range of several hundreds of ohms, or greater. This will make small, low-noise amplifier design somewhat easier than is the case for the very low-resistance detectors. Details of the amplifier chain for each channel must wait until more certain information is available on detector characteristics. It is possible that amplifiers presently being used for HgCdTe detector arrays can be modified slightly for this purpose.

The output of each detector will drive one light emitting diode in a linear array which is arranged exactly like the detector array but much smaller as shown in Figure 52. The array will be viewed by reflection from a small de-scan mirror attached to the same axis as the scanning mirror. Therefore, the light intensity pattern on the diodes will match that of the submillimeter radiation falling on the detectors. It is convenient to image these light emitting diodes with a vidicon tube looking at the de-scan mirror. The image can then be displayed in the usual TV format.

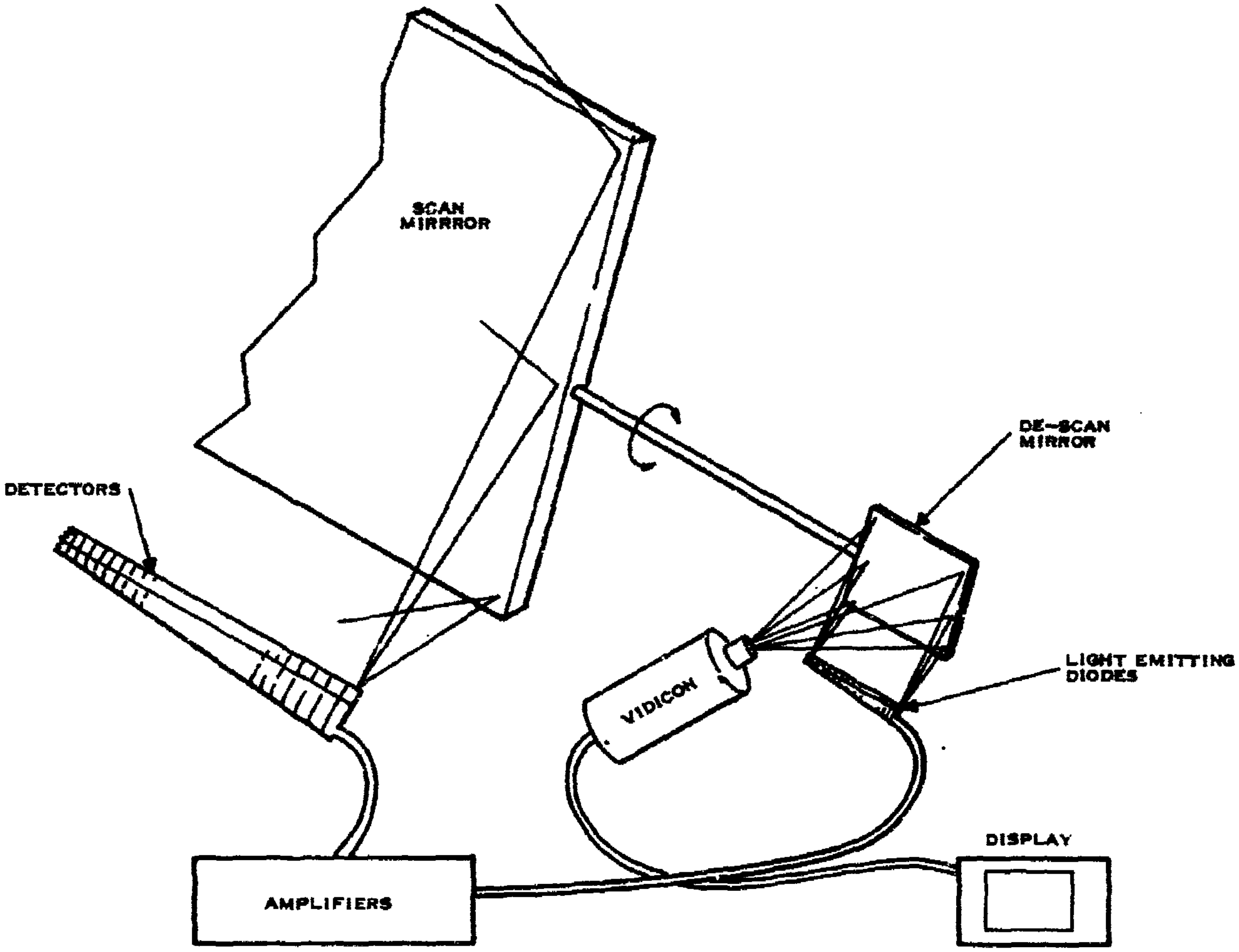

162375

Figure 52. Display Method Schematic

C. Detector Array

The ultimate success of building a real-time imaging system will depend on the ability to produce a large number of submillimeter detectors with uniformly good detection characteristics. To gain insight into the feasibility of this task, a 10-element array was assembled.

Each of the InSb detectors in this array was fabricated individually according to the procedure outlined in section II.A. The 10 detectors were then epoxied to a ½- by 1-inch sapphire substrate in the form of a linear array. A photograph displaying this arrangement and the associated electrical leads is shown in Figure 53.

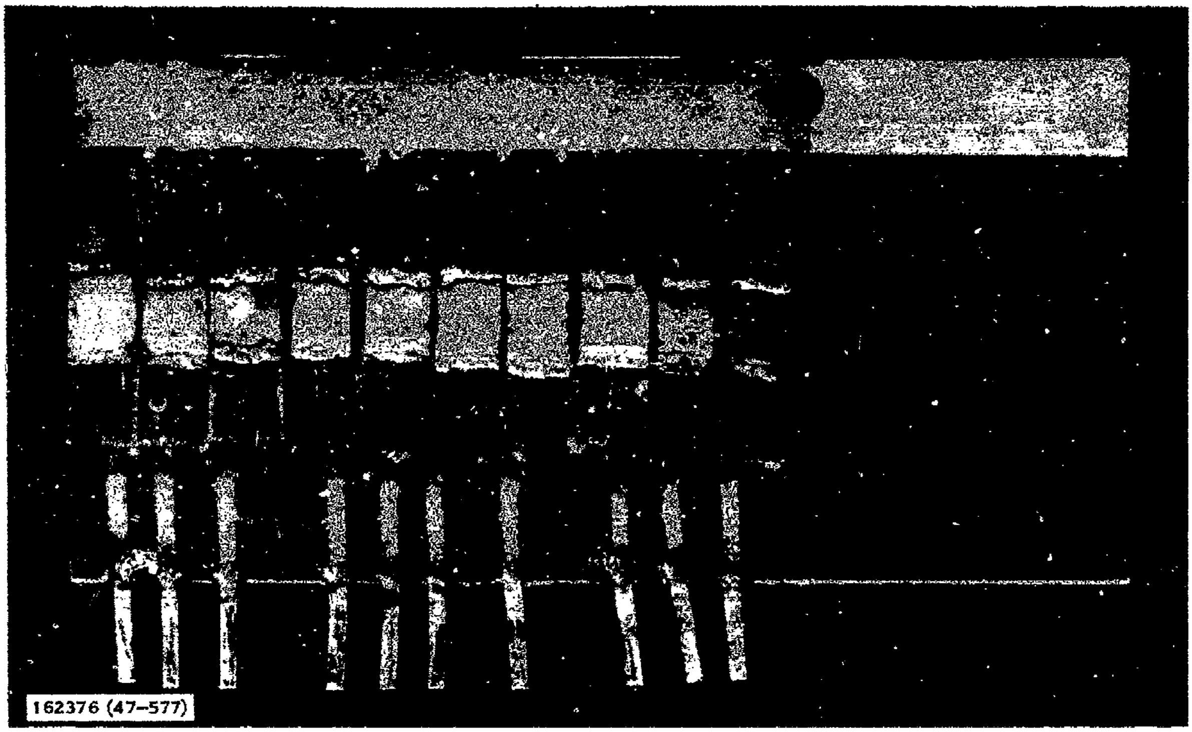

Figure 53. 10-Element InSb Free Electron Bolometer Linear Array

Measurements for these detectors were taken on an individual basis just before their mounting in the final array. Figure 54 exhibits the current-voltage relationship of three of these detectors. Data for the remaining seven detectors fall within the extremes established by detectors no. 2-16 and no. 3-9 and have been omitted for clarity.

The NEP variation along the array is shown in Figure 55. Deviation from the average value of 1.4 X 10^{-13} W-$Hz^{-1/2}$ is about ±30 percent. This deviation can be tightened simply by fabricating a larger set of detectors and by replacing the fringe units of the array with detectors closer to the average.

Stability of the detectors in an array with regard to storage time in various environments is always a concern when assembling an array. As pointed out earlier, some aging effects have been observed in the InSb detectors. These effects have been kept to a minimum by using low temperatures ($T \cong 270°C$) during the contact alloying process. The I-V curves of these units as monitored over a period of 2 to 3 months will, in general, move toward higher resistance by a few percent. This should present little problem since only minor adjustments in the biasing circuit of the preamplifier are necessary to compensate for this drift. In all cases, the aging has actually improved device sensitivity.

As discussed in Subsection IV.B, a real-time system using a 60-detector array is envisioned. With the experience gained in working with the 10-element array, the time and effort required to assemble 60 uniform detectors can be projected. Because the fabrication procedure is becoming increasingly efficient, it should be possible to attain yields (detectors with NEP values within the

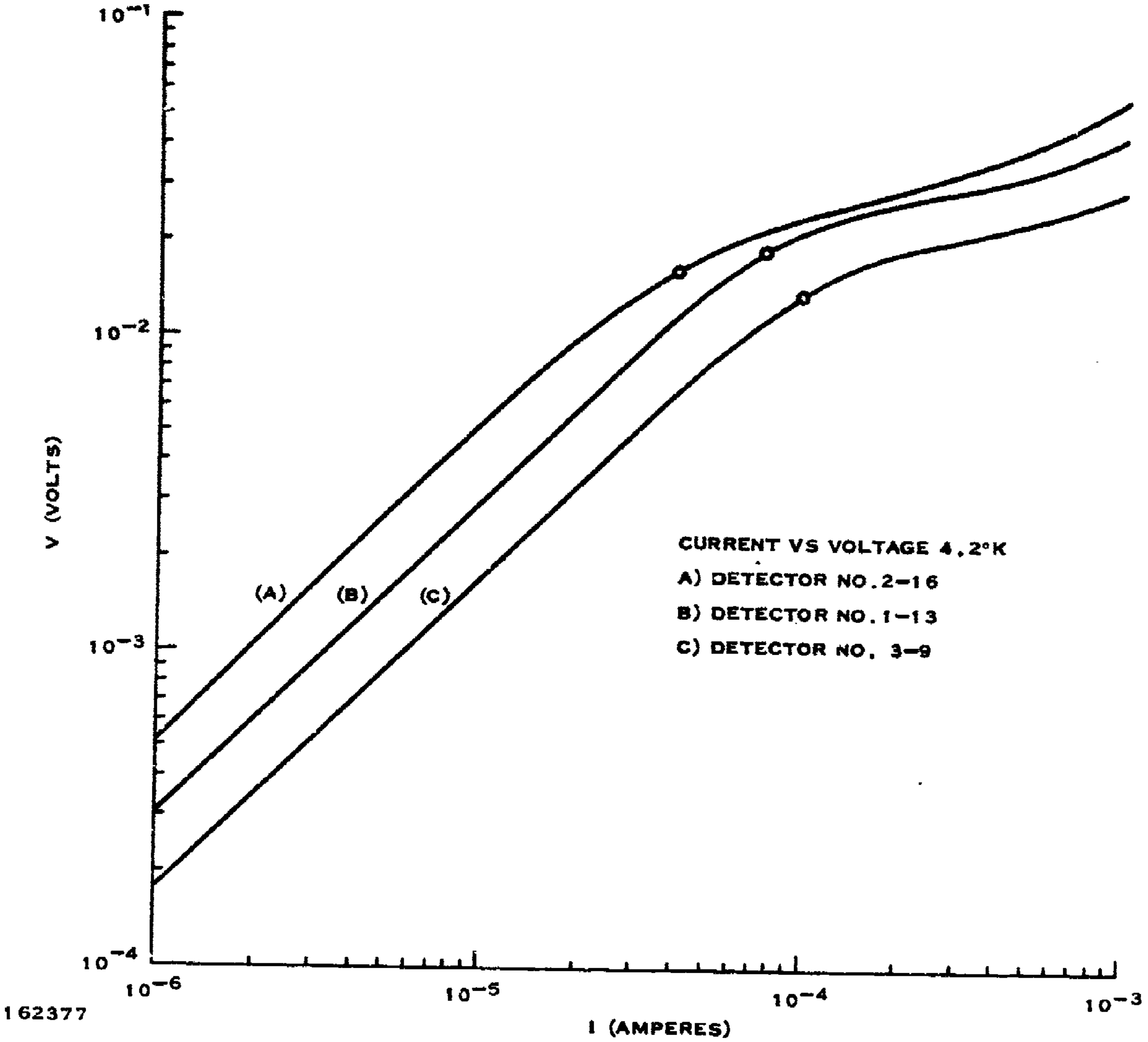

Figure 54. Current-Voltage Relationship of Three Detectors Used in the Array

limits established by the 10-element array) of about 50 percent. At the moment, one person starting from the cut material can assemble about 15 units in a week. Assuming this 50-percent yield and the aid of an additional person to measure the devices, a few months time would be required to assemble the larger array.

D. Increased Sensitivity

1. The Detector

During this study, system performance was quite noticeably improved by using an InSb detector which had an anomolously high sensitivity, approximately 2 to 3 times better than detectors used in the array. In contrast to the stable detectors used in the array, this detector

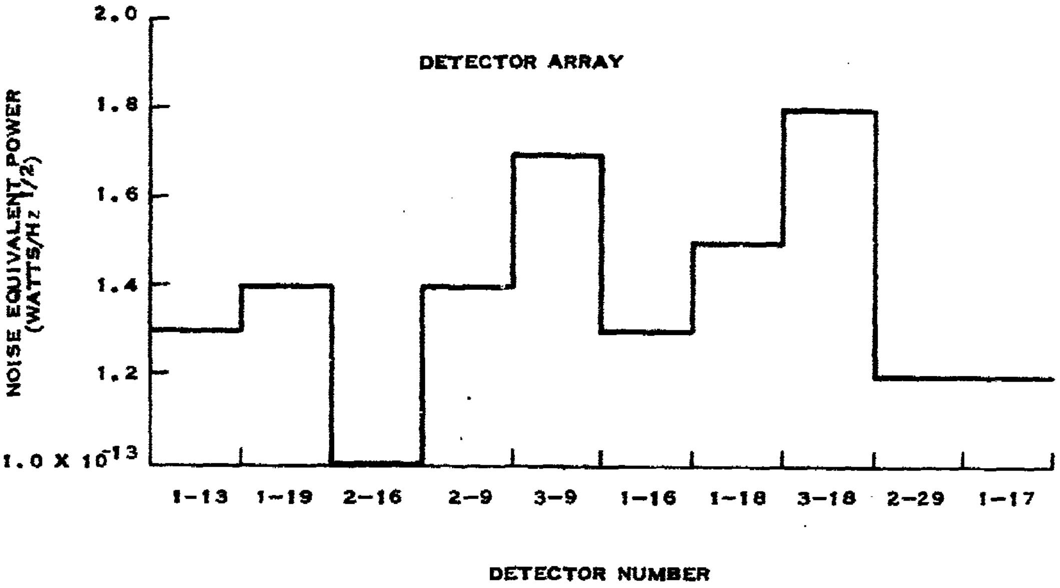

162378

Figure 55. NEP Variation Along the Detector Array

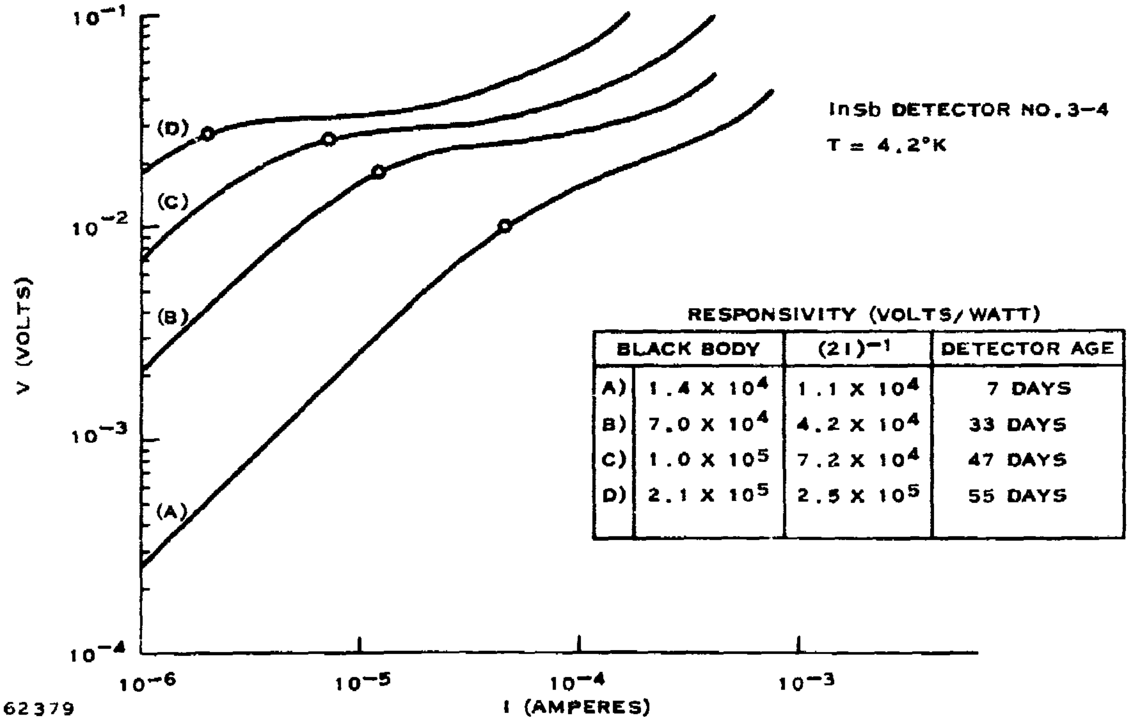

RESPONSIVITY (VOLTS/WATT)

	BLACK BODY	$(2I)^{-1}$	DETECTOR AGE
A)	1.4×10^4	1.1×10^4	7 DAYS
B)	7.0×10^4	4.2×10^4	33 DAYS
C)	1.0×10^5	7.2×10^4	47 DAYS
D)	2.1×10^5	2.5×10^5	55 DAYS

162379

Figure 56. Current-Voltage Relationships Taken at Various Times Since Detector was Fabricated

was fabricated using a relatively high alloying temperature (T > 350°C). In general, devices fabricated at these higher alloying temperatures exhibited very poor detection characteristics, usually because of excessive contact noise. However, in some instances as in this case, detectors were successfully fabricated.

In these detectors, an aging phenomena was frequently observed. This is displayed in Figure 56 where I-V data are plotted at various times since the device was made. The entire aging process occurred while the detector was mounted in a helium Dewar and was maintained in a vacuum. It should be mentioned that this detector is an extreme example of this effect and, in general, other detectors did not exhibit this degree of aging.

A possible explanation of this phenomenon comes from the work of Vystavkin, et al.[18] The effects of varying degrees of compensation on the characteristics of InSb submillimeter detectors were studied by this group. They found that as the compensation increases, the device resistance increases and the nonohmic region begins at higher electric fields in a manner similar to that shown in Figure 56. Thus, it is possible that the Texas Instruments detector is moving toward a higher degree of compensation during the aging process.

Additional evidence for this interpretation is obtained by noting the negative differential resistance region in the I-V data taken at a reduced temperature as shown in Figure 57. Bannaya, et al.[19] observed a similar effect in the absence of a magnetic field only for samples that were very highly compensated.

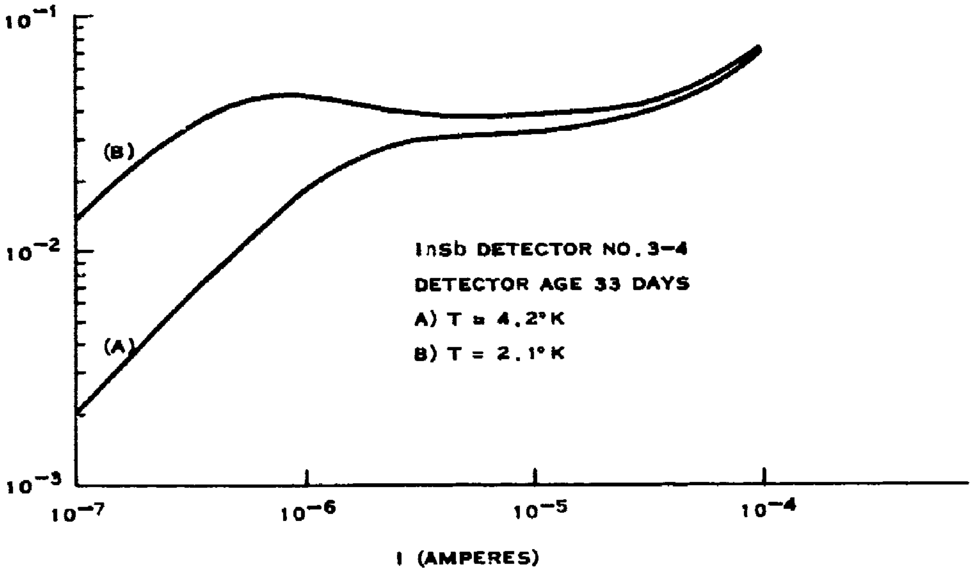

162380

Figure 57. Negative Differential Resistance Observed in the Current-Voltage Data at Reduced Temperature

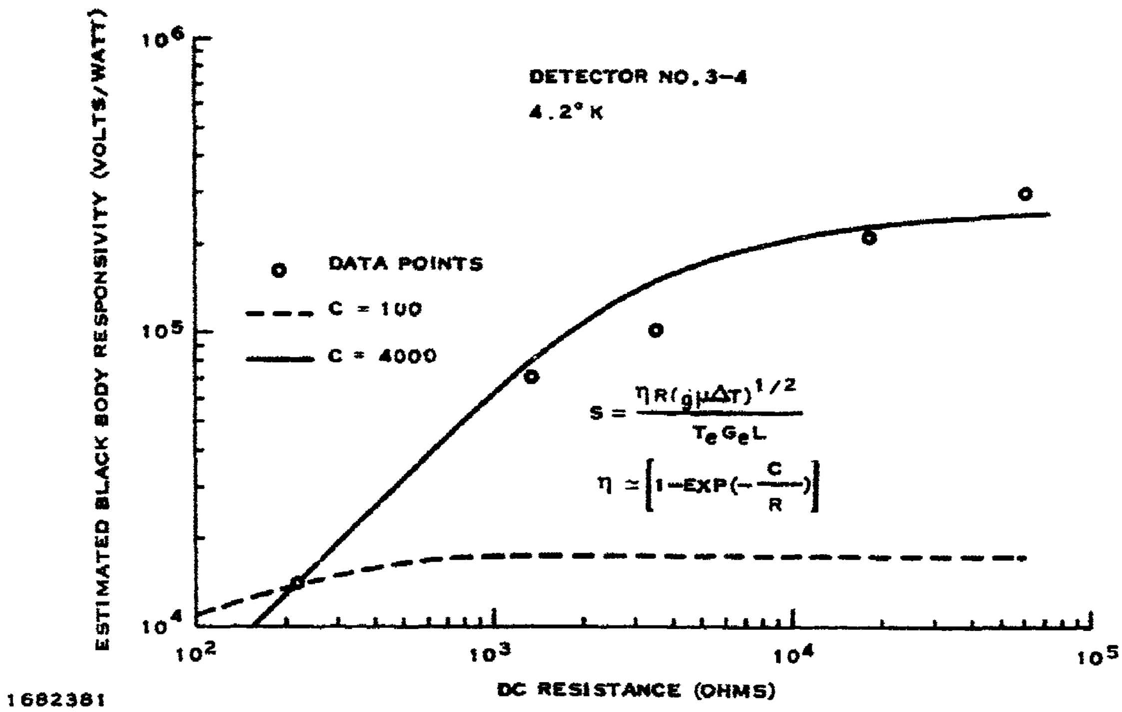

Figure 58. Dependence of Detector Responsivity on Device DC Operating Resistance

There are two schools of thought as to the cause of this negative differential resistance. One associates the effect with the freezing-out of carriers into an impurity band which has separated from the conduction band. The other explains the phenomena in terms of the momentum and energy scattering mechanisms in the material at this reduced temperature. Both interpretations are reviewed in the literature.[20] In any event, the high-temperature alloying process has likely introduced impurities and defects into the sample which slowly anneal with time and give rise to the aging phenomena.

Blackbody responsivity estimates were made for the detector as it has progressed through the aging processes. These values are tabulated in the inset of Figure 56, which shows that they are in rough agreement with the responsivity estimates taken from the I-V curves. The dependence of the responsivity on the dc operating resistance is shown in Figure 58. These measured responsivities are much higher than those predicted earlier for the free electron bolometer. It is also noted that, at these high operating resistances, the free-carrier absorption efficiency η should be rapidly approaching zero. The effect of this loss of absorption on responsivity is demonstrated by the dashed line in the figure. This line represents the responsivity as computed by assuming an absorption coefficient given by Equation (7) and then matching the data with the calculations at 220 ohms. The continued rise in the measured responsivity with increasing resistance indicates that the absorption coefficient is much larger than that predicted in Equation (7). Assuming an increase in α of 40 times, the solid curve shown in the figure can be calculated. The agreement with measured values is much better in this case. The justification for using such a large absorption coefficient may come from recent work carried out at the A.F. Joffe Institute in the USSR.[21] A model is proposed in which the conduction band in

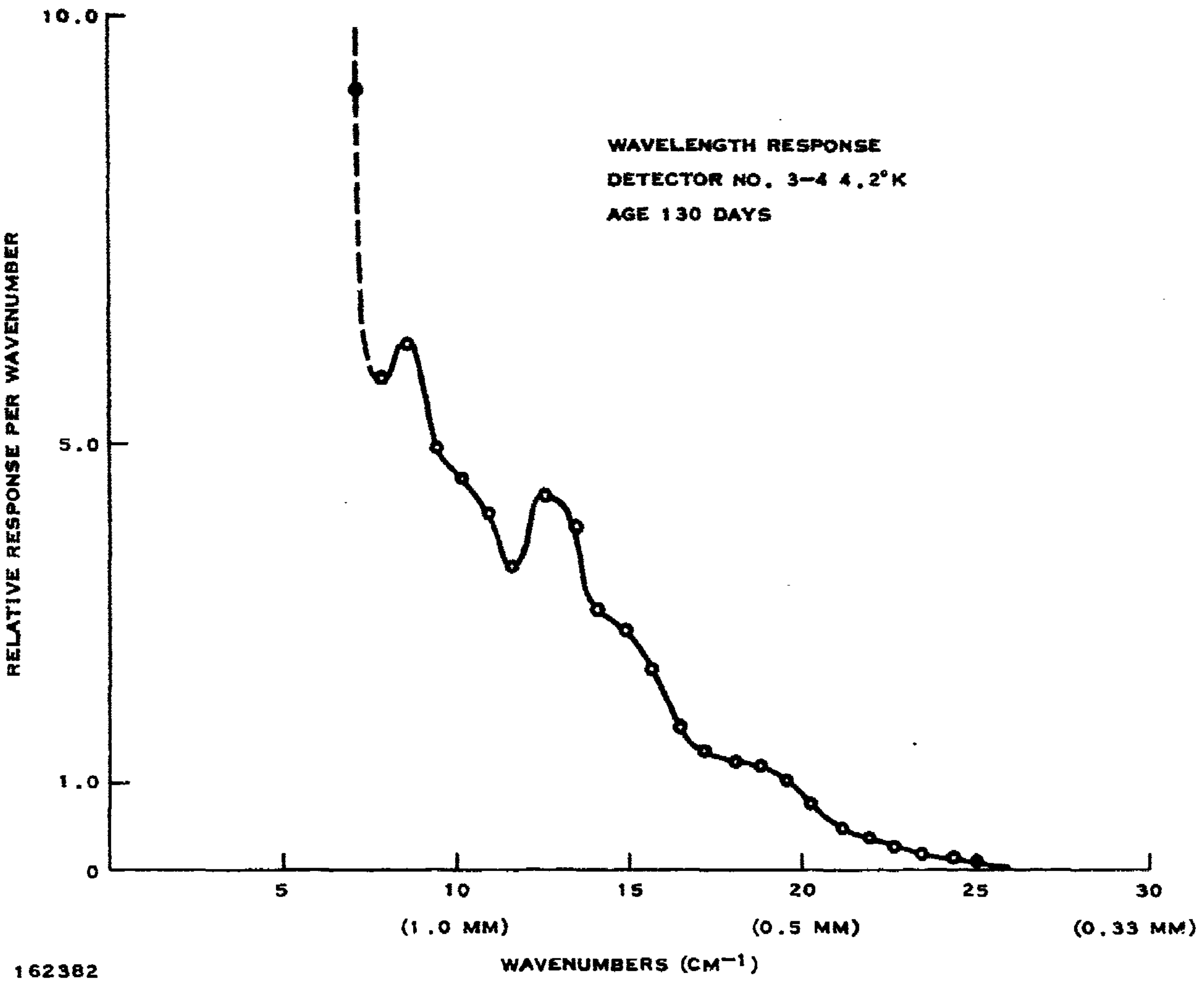

Figure 59. Relative Response as a Function of Wavelength for the Aging Detector

closely compensated InSb becomes modulated by regions of varying charge density. The dc conductivity is limited by barriers formed from the undulating conduction band. However, these barriers are far enough apart so as not to limit the high-frequency conductivity. Thus, the absorption coefficient which is dependent on the high-frequency conductivity may be many times larger than that predicted using the dc conductivity.

The above suppositions are based on the premise that the absorption is occurring via the free-carrier mechanism. To determine the validity of this assumption, relative response versus wavelength data were taken. This was done using a Fourier transform spectrometer capable of obtaining the response out to about 1.5 mm. The results are shown in Figure 59. The filtered detector response begins at about 0.4 mm and continues to increase out to 1.5 mm. Structure in the data is thought to be related to filtering and interference effects in the spectrometer rather than to physical processes in the detector. The typical free-electron bolometer response flattens out at about 0.8 mm (Figure 8). That the measured response is still increasing at 1.5 mm implies that the momentum relaxation time in this detector is longer than in previous units or that absorption is occurring by some other mechanism. To differentiate between the two possibilities, one must observe either a flattening in the response curve, characteristic of free-carrier absorption, or a strong peaking in the response data, more characteristic of other absorption mechanisms. Unfortunately, the limitations of the spectrometer were reached before this differentiating region in the spectra was reached. Thus, the spectral data is inconclusive, neither establishing nor ruling out the possibility of free-carrier absorption.

For practical applications where a real-time imaging system is desired, the ability to consistently reproduce detectors with these high sensitivities is of major concern. At the moment, the materials and processes required to do this can only be speculated. With the information obtained from this detector, it appears that very highly compensated (≅99 percent) InSb having impurity concentrations near 10^{15} cm^{-3} is desired. The contacting process must be undertaken in as clean an environment and at as low a temperature as possible to prevent unintentional contamination of the material. The goal is to fabricate detectors that exhibit the high-resistance characteristics of detector no. 3-4 without going through the aging process.

2. The Optics

Before leaving the topic of improved sensitivity, comments on system optics are in order. The feasibility scanner used only reflective optical elements for GaAs (only one with optical power) and, in addition, two aplanatic lenses for the InSb sensor. Polyethylene, Teflon and some of the acrylics can be made into good transmission elements. A system combining these might improve the overall collection efficiency and would probably aid in the design of a scanning technique that would not degrade resolution. The properties of many materials at these wavelengths need to be determined, particularly dielectric constants, so that the usual optical techniques such as antireflective coatings can be applied.

E. Closed Cycle Coolers

An imaging system using InSb or GaAs for detecting radiation at submillimeter wavelengths must provide means for maintaining the detectors at temperature below 5°K and the cold shields below 20°K, or there about. This can be done easily with liquid helium storage Dewars for periods of 6 or more hours. For operating convenience, it would be desirable to avoid the necessity of filling the detector Dewar prior to each use.

While closed cycle coolers are reasonably compact for small heat-loads and temperatures down to 20°K, temperatures below 5°K can be reached only with somewhat large units. The specifications for a closed cycle cooler for a submillimeter imaging system can be determined only when a preliminary design has been decided upon; however, some estimates can be made.

Heat that must be cooler dissipated comes from three principle sources; radiative transfer from the outside world, conduction along lead wires, and radiation through the window which is absorbed by the cold filter or by the detectors. A rough approximation of the radiative heat load on a cold assembly ($\ll 300°K$) contained in double-walled Dewar with a simple heat shield is

$$q \simeq \frac{A_0\, \sigma\, (T)^4}{4/\epsilon - 2} \text{ watts}$$

where A_0 is the outside area, ϵ is the emissivity of all the surfaces, T is the temperature of the outside world (≅300°K) and $\sigma = 5.67 \times 10^{-12}$ W/cm^2 (°K)^4. Therefore, if the detector and cold shield assembly has an area of 200 cm^2 and $\epsilon = 10^{-2}$, the heat load from this source would be approximately $q \cong 2.3 \times 10^{-2}$ W.

The heat conducted down n lead wires of conductivity, k_s, cross-sectional area, A_s, and length L_s is

$$q \cong nk_sA_s\ \Delta T/L_s$$

Typical values in this case might be $n = 100$, $A_s = 5 \times 10^{-5}$ cm^2, $L_s = 10$ cm, $\Delta T = 300$°K, and for a wire with low thermal conductivity, $k_s = 0.1$ W/cm°K. The heat load from this source would be $q \cong 1.5 \times 10^{-2}$ W.

The radiation absorbed by the filter and detectors can be approximated conservatively (high value) by calculating the energy incident on the filter as equal to the total energy that would be emitted by a blackbody of the same area and at the temperature of the outside world A 300°K blackbody emits 4.5×10^{-2} W/cm^2 so that a 25 cm^2 filtered aperture would receive about 1 watt and would be the dominant heat load.

A cooler that would maintain 4.5°K with a 1- to 2-W heat load would most likely be more than adequate to cool the detector array of any system developed for the submillimeter imager. As an indication of the characteristics of such a cooler, Cryogenic Technology, Incorporated, model 504 cooler provides up to 2.5 W cooling at 4.5°K. This total unit weighs about 550 pounds and requires over 9 kW to operate.

F. Active System Considerations

An imaging system can be made active in two ways, broadband illumination and detection, or narrowband heterodyne detection of reflected energy similar to radar. The illumination technique can be used to enhance metal objects in an image made from emitted radiation. However, much more power is necessary than when heterodyne detection is used to reject all emitted radiation and the image is made entirely from energy reflected in the very narrow spectral bandpass of the source.

InSb and GaAs detectors have the high sensitivity and fast response necessary for passive imaging in the submillimeter and millimeter wavelength part of the electromagnetic spectrum. If sources of coherent radiation were readily available in this region, other applications requiring active systems would become possible. Targets could be illuminated, heterodyne detection could be used, and radar and communication systems would be possible.

For most applications, atmospheric absorption at wavelengths between 0.03 and 0.2 millimeters is excessive. When fog is present, scattering prohibits the use of wavelengths shorter than 0.03 mm, therefore 10-mm and longer wavelengths have been used to penetrate fog. However, when resolution is important, as for imaging, it is desirable to operate at as short a wavelength as possible. For ranges up to a few hundred meters, submillimeter wavelengths may be the most suitable.[22,23] A resolution of 1 mrad is possible with only a 1-m collecting aperture.

1. Illumination

The radiant emittance of a blackbody in a broad spectral bandpass near 0.7 mm is approximately 10^{-6} W/cm^2. To overpower this in a 1-m field of view with radiation from a high reflectivity diffuse surface would require greater than 10^{-2} W. Since there will be less than perfect reflectivity from concealed metal objects, it would appear that at least 0.1 W would be needed to enhance passive imagery with an illuminator. It is likely, however, that specular reflection from edges could highlight concealed metal objects with significantly lower power levels, possibly only milliwatts.

Radiation with wavelengths between 0.2 and 2.0 mm can be generated with either electron beam devices, gaseous molecular lasers or avalanche diodes. Molecular gas lasers have been operated at many wavelengths between 0.2 and 2.0 mm.[23] Among the gases used are H_2S, H_2O, CH_3, HCN, SO_2, and alcohols.

The gaseous molecular lasers are generally low-power devices delivering microwatts to a few mW. However, recent research[24,25,26] shows promise of producing watts of power throughout the submillimeter portion of the spectrum by pumping with CO_2 lasers because of the extremely high power available from these lasers.

It has been demonstrated that tens of milliwatts of power can be obtained in the submillimeter portion of the spectrum by pumping symmetric top molecular gases with 10-μm radiation from a 200-W pulsed CO_2 laser. The efficiency of this process is presently less than 0.1 percent. No matter how efficiently the CO_2 laser radiation is absorbed, the process will always have low efficiency as long as each 10-μm photon results in only one rotationally excited molecule in the submillimeter cavity. Since molecular collisions tend to destroy population inversions, this mechanism is not available for distributing the 10-μm energy. Therefore, it appears that the maximum theoretical efficiency would be the ratio of the pump wavelength to the submillimeter wavelength.

Electron beam devices and avalanche diodes have been pushed to shorter wavelengths so that both have been made to produce radiation at less than 1 mm. However, the power output is generally less than 1 mW. The difficulties experienced in increasing the efficiency or power are related to device geometry. All the energy must be generated in volume comparable to a wavelength. In spite of this, one backward-wave oscillator (the Thompson CSF Carcinotron) can be made to deliver about 1 watt at 1 mm and up to several tenths of a watt at 0.5 mm. Carcinotrons develop their power in a relatively small volume and appear to be very difficult to construct. Another electron device, still in the research stage, holds promise of greater power and efficiency since the radiation is generated as a standing wave in a larger, multimode cavity. This electron tube is described in some detail by Mizuno, et al.[27] and has been reported on by Rusin and Bogomolov,[28] who called it an "orotron."

The principle of operation can be seen from the sketch of Figure 71 from the Mizuno report.[27] A thin ribbon-shaped beam of electrons is passed very close to a grooved mirror surface. The electrons interact with the grooved surface and emit Smith-Purcell radiation.[29] The flat plate forms a Fabry-Perot cavity with the grooved surface as the other mirror. A standing wave is set up and extracts energy from the electron beam.

The most difficult part of the assembly is the accurate machining of the grooved surfaces.[30] However, a relatively new technique for precise preferential etching along certain crystal lattice axes in silicon has been developed at Texas Instruments and should make possible the manufacture of gratings with extremely accurate dimensions through the use of photomask techniques. In addition, this method would make possible the creation of groove shapes that could not be machined at all. Some of these may significantly improve the efficiency and power output of the device.

The most important initial step that could be taken would be to expand the theory in order to predict the optimum groove shape and dimensions. A rigorous three-dimensional theory of the Smith-Purcell effect was recently presented[31] and may be useful in expanding the theory given by Mizuno et al.[27] in the design of their resonator. While the optimum design for a given wavelength grating was being developed, the photoetching techniques could be perfected by building a grooved surface similar to the ones that have already been used but with the greater precision made possible by these techniques.

For illumination, then, there is one source that can produce adequate power and several others that might do so after further development. In the other mode of operation where heterodyne detection of reflected radiation is used, less radiation by orders of magnitude is needed and most of these sources are adequate; therefore, this mode of operation will be considered in more detail.

2. Heterodyne Detection of Submillimeter Electromagnetic Energy

a. Theory

The heterodyne concept is used widely in radio, television, and radar because of high gain and narrow bandwidth which allows greater sensitivity and frequency selectivity than other detection methods. Since the invention of the laser, heterodyne detection has been done at optical wavelengths. The basic schematic layout[32,33] for an optical heterodyne detector is shown in Figure 60. Here, the illuminator is a coherent source such as a carcinotron or a laser, and beamsplitters mix a small part of the illuminator power with that scattered from objects within the field of view to effect a local oscillator signal.

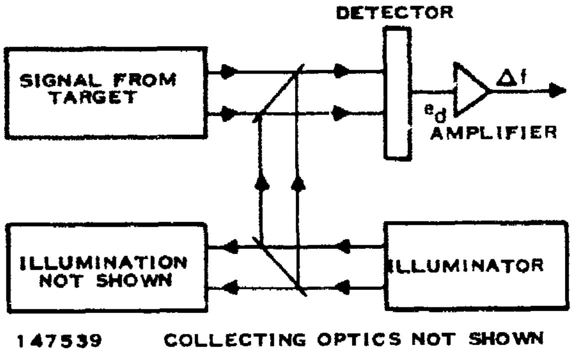

Figure 60. Basic Concept of Heterodyne Detector

If e_i is the e-vector of the incident wave and e_o is the e-vector of the local oscillator wave, then the power detected by the detector is

$$P = |e_i + e_o|^2 \tag{61}$$

The actual detector voltage is

$$e_d = RP$$

where R is the detector responsivity. Assuming e_i and e_o to be sinusoids then the detector voltage becomes

$$\begin{aligned} e_d &= R|e_i + e_o|^2 \\ &= R[E_i^2 \sin^2 w_i t + 2E_iE_o \sin w_i t \sin w_o t + E_o^2 \sin^2 w_o t] \\ &\simeq 2RE_iE_o \sin (w_i - w_o)t \end{aligned} \tag{62}$$

The double frequency and sum frequency terms are filtered out by stray capacitance of the detector. The difference frequency can be a few megahertz or less and is amplified by the amplifier following the detector. The coefficient of the difference frequency term E_iE_o shows how the intensity of the local oscillator E_o introduces gain into the process. Actually, for the condition where the local oscillator beam is vastly greater than that of the signal, the gain is so high that the signal for unit signal-to-noise ratio (SNR) is only a few photons, or

$$P_o = \frac{2hc\Delta f}{\lambda\eta} \tag{63}$$

according to Teich.[32] Here the equation parameters are

h = Planck constant

c = speed of light

Δf = electrical bandwidth

λ = wavelength

η = photon efficiency.

Teich reports measured minimum detectable powers near that calculated from Equation (63) at 10.6 μm. For example, at $\lambda = 750$ μm and unit bandwidth, P_o becomes

$$P_o = \frac{2 \times 6.626 \times 10^{-34} \times 3 \times 10^8 \times 1}{750 \times 10^{-6} \times 0.5} = 1.06 \times 10^{-21} \text{ W/Hz}$$

assuming a detector photon efficiency of $\eta = 0.5$. Equation (63) is the basic equation determining the ultimate sensitivity of a heterodyne detector.

The frequency selectivity can be determined from the derivative of the wavenumber definition, or

$$d\nu = \frac{d\lambda}{\lambda^2} \quad (\text{cm}^{-1})$$

and (64)

$$df = \frac{c\,d\lambda}{\lambda^2} \quad (\text{hertz})$$

For example, for a bandwidth of 10 kHz, the wavelength interval of interest is

$$d\lambda = df\,\lambda^2/c = 10^4 \times (750 \times 10^{-6})^2/3 \times 10^8 = 1.88 \times 10^{-5} \ \mu\text{m}$$

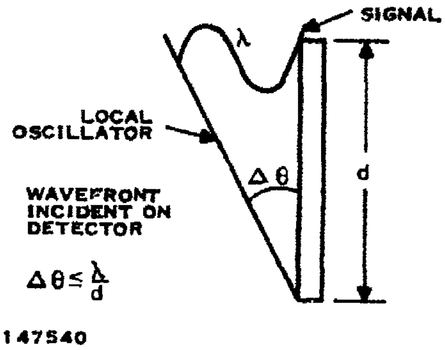

Figure 61. Basic Restriction on the Angle Between Incident Wavefronts for Heterodyne Action

The overall effect of this selectivity is to reduce greatly the influence of thermal background since the signal spectrum is entirely within dλ while the background has a graybody spectral distribution.

The wavefronts of the signal and local oscillator must be very close to parallel, as shown in Figure 61. According to Siegman,[34] heterodyne action will occur if this angle is such that

$$\Delta\theta < \frac{\lambda}{d} \tag{65}$$

The sine of $\Delta\theta/2$ is the numerical aperture of the system. For a square detector 1 mm on an edge

$$\Delta\theta = 750 \times 10^{-6}/10^{-3} = 0.75 \text{ rad} = 42.9 \text{ degrees}$$

For a single lens possessing this angle, the corresponding *f*-number would be

$$f/n = \frac{1}{2 \tan \Delta\theta/2} = 1.27$$

Thus, a fairly fast optical system could be used here. For shorter wavelengths in the infrared and in the visible, the constraint on $\Delta\theta$ results in high *f*-number systems.

b. Anticipated Performance

(1) Active Heterodyne System

There is a substantial body of literature on heterodyne detectors used with imaging laser radars at 10.6 μm. The imagery from such a system tends to be brilliantly highlighted on curved surfaces where specular reflections occur. Elsewhere, the imagery is low contrast because of low diffuse reflection. Beyond a certain distance everything is black because the laser return is too weak to register and the thermal background is suppressed effectively by the tiny dλ. The visible portions of the imagery possess the speckled pattern characteristic of imagery made with laser light. Coherent imagery at 750 μm should also possess these properties.

Some idea of the reflected signal irradiance can be obtained from the equation

$$H' = \frac{P_T \, A_T \, \rho}{\alpha^2 \, R^4 \, \pi} \quad \text{for } \frac{A_T}{R^2} < \alpha^2 \tag{66}$$

Assuming a transmitted power of $P_T = 1$ W, target area $A_T = 10$ cm², diffuse reflectivity $\rho = 1$ percent, resolution $\alpha = 1$ mrad, and range $R = 200$ feet, the irradiance at the sensor collecting aperture is $H' = 2.30 \times 10^{-11}$ W/cm². If a bandwidth of 10 kHz is assumed along with an optical efficiency of $\epsilon = 0.3$ and an $A_c = 1\ m^2$ collecting aperture, then the noise equivalent irradiance (NEI) of the system is

$$\mathrm{NEI} = \frac{P_o\ \Delta f}{A_c\ \epsilon} = \frac{1.06 \times 10^{-21} \times 10^4}{10^4 \times 0.3}$$

$$= 3.53 \times 10^{-21}\ \mathrm{W/cm^2} \tag{67}$$

The irradiance incident on the collecting aperture due to thermal background at 300°K is

$$\begin{aligned} H_B &= N_{BB}\ (300)\ \alpha^2\ d\lambda \\ &= 0.758 \times 10^{-9} \times 10^{-6} \times 1.88 \times 10^{-5} \\ &= 1.425 \times 10^{-20}\ (\mathrm{W/cm^2}) \end{aligned} \tag{68}$$

Comparing H′ with both NEI and background, it is seen that H′ is a very strong signal. If gain and dynamic range are adjusted so that the brightest signal just saturates the display, and assuming a dynamic range of 100:1, it is seen that the background N_B is not visible on the display.

(2) Passive Heterodyne System

In the absence of an illuminator beam, it is unlikely that the heterodyne detector also can be used to image the thermal background. The irradiance for a 310°K blackbody is $1.47 \times 10^{-20}\ \mathrm{W/cm^2}$ so that its contrast with the 300°K blackbody is $\Delta H = 4.90 \times 10^{-22}\ \mathrm{W/cm^2}$, which is well below the NEI of Equation (67).

(3) Broadband System

For comparison purposes, consider the performance of a broadband nonheterodyne system possessing the same optical system and scanner. Assume an InSb detector with an NEP of $5 \times 10^{-13}\ \mathrm{W/Hz^{1/2}}$ and a wavelength band of 500 to 1,000 μm, the NEI for that system is

$$\begin{aligned} \mathrm{NEI} &= 5 \times 10^{-13} \times \sqrt{10{,}000}/(10{,}000 \times 0.3) \\ &= 1.66 \times 10^{-14}\ \mathrm{W/cm^2} \end{aligned}$$

The background at 300°K over that wavelength interval is

$$\begin{aligned} H_B &= \bar{N}\ (300)\ \alpha^2 \\ &= 0.5589 \times 10^{-12}\ \mathrm{W/cm^2} \end{aligned}$$

A target possessing a temperature of 310°K produces a contrast of

$$\begin{aligned} \Delta H &= \bar{H}\ (310) - \bar{H}\ (300) \\ &= (0.57826 - 0.55890) \times 10^{-12} \\ &= 1.94 \times 10^{-14}\ \mathrm{W/cm^2} \end{aligned}$$

which is slightly greater than NEI. The bars over N and H refer to integration over the wavelength band of interest.

3. Summary

These data are summarized in Table VII. It is evident from these calculations that a heterodyne system yields higher signal-to-noise ratio in the active case. The nonactive heterodyne system should not image the thermal background at all, which is consistent with the imagery taken at 10.6 μm.[35,36] At the 200-foot range, the active system reflection is so strong that the illuminator could be reduced from 1 W to a lower level.

TABLE VII. COMPARISON OF ANTICIPATED PERFORMANCE OF HETERODYNE AND BROADBAND DETECTORS

	Heterodyne (W/cm²)	Broadband (W/cm²)
Noise equivalent irradiance (NEI)	3.53×10^{-21}	1.66×10^{-14}
300°K background	1.43×10^{-20}	5.59×10^{-13}
310°K signal	1.47×10^{-20}	5.78×10^{-13}
$\Delta H_{passive}$	4.9×10^{-22}	1.94×10^{-14}
ΔH_{active}	2.30×10^{-11}	2.30×10^{-11}

SECTION V

CONCLUSIONS AND RECOMMENDATIONS

The modified Thermlscope developed under this contract has produced imagery from radiation emitted by objects in the submillimeter spectral region. The major conclusions based on experiments conducted with this system and related studies are listed.

1. At a wavelength near 0.3 mm, good images can be obtained through one or two layers of cloth. Only occasionally can an image be made that is distinguishable from folds and varying cloth thickness when the weapon is covered by several cloth layers, such as a suit coat. At this wavelength, variations in cloth temperature are easily visible when the cloth is thick enough to represent more than one optical depth of material. These results are entirely consistent with the measured transmissivities of cloth samples.
2. At wavelengths of greater than 0.5 mm, greater penetration of cloth is observed. Because of the broad spectral response of this detector and the wavelength-dependent diffraction pattern on the detector, the exact wavelength of maximum system response is not known. However, peak response to blackbody radiation must lie between 0.6 and 1.0 mm. Images made with the InSb long-wavelength detector show that images are obtainable through suit coats at a 0.75-mm wavelength.
3. Penetration of fairly thick layers of cloth could be achieved by a system operating in the 1.0- to 1.5-mm atmospheric window. However, the resolution for a reasonable size ($\cong$3 foot) collecting aperture would limit the range of shape recognition for small weapons to probably 15 to 20 feet (2×10^{-3} radian resolution).
4. A broadband source of radiation has been found to be useful as an illuminator to highlight metallic objects. It is possible that a milliwatt source of monochromatic submillimeter radiation would make a significant contribution to system performance.
5. The most crucial step in the fabrication of InSb detectors has been found to be the contacting process where indium is alloyed onto the ends of the indium antimonide chip. By maintaining a minimum temperature ($\cong$270°C) during this process, a high yield of good detectors with uniform detection characteristics can be obtained.
6. A 10-element linear array of these InSb detectors was assembled and tested. The NEP values of the 10 detectors vary by less than 30 percent from an average value estimated to be 1.4×10^{-13} W-Hz$^{-1/2}$. These detectors can be consistently reproduced and yields as high as 50 percent may ultimately be attainable.
7. Detectors fabricated at higher alloying temperatures have frequently undergone an aging process in which the device resistance has changed significantly over a period of months. This aging has been found to act in favor of higher detector sensitivity. The most sensitive detector to date has undergone this aging and has NEP values a factor of 3 better than any other detector. Unfortunately, neither the aging process nor the anomalously high sensitivity associated with this detector is completely understood. Further study will be required before detectors of this quality can be consistently reproduced in a sufficiently uniform manner for use in an array.

To achieve an effective real-time imaging system based on the knowledge gained in working with this feasibility model, three parallel programs are necessary. One is further detector development, the second is the development of a submillimeter source of radiation, and the third is preliminary system design.

A. Detector Development

Detectors are often the keys to successful imaging system performance and require considerable time and optimization effort. In this case, the InSb detector appears to be the proper detector for this application. It not only has a longer wavelength response where clothing is more transparent, but by proper filtering and material selection, it can be made to have peak response at wavelengths from 0.5 mm to microwaves.

The InSb detector used in this study exhibited detection characteristics considerably better than those of the typical detector. However, there is no capability to fabricate a large array of these detectors at this time. To attain this capability further study of the InSb detectors will be required. The most important detector characteristics requiring understanding are the reasons for the detector aging and the mechanism by which these detectors absorb submillimeter radiation.

B. Submillimeter Source Development

InSb and GaAs detectors have the high sensitivity and fast response necessary for passive imaging in the submillimeter and millimeter wavelength part of the electromagnetic spectrum. If sources of coherent radiation were readily available in this region, other applications requiring active systems would become possible. Targets could be illuminated, heterodyne detection could be used, and radar and communication systems would be possible.

One such possible source, the "Orotron," is still in the research stage. This electron-beam device holds promise for good efficiency at reasonable power output in the submillimeter portion of the spectrum.

The most difficult part of this device assembly is the accurate machining of a grooved surface used as a grating. However, a relatively new technique for precise preferential etching along certain crystal-lattice axes in silicon has been developed at Texas Instruments and should make possible the manufacture of gratings with extremely accurate dimensions through the use of photomask techniques.

The most important initial step that could be taken in developing the Orotron would be to expand the existing theory in order to predict the optimum groove shape and dimensions. While the optimum design for a given wavelength grating was being developed, the photoetching techniques could be perfected by building a grooved surface similar to the ones that have already been used but with the greater precision made possible by these techniques.

C. Preliminary System Design

One possible design for a real-time imaging system was discussed in the text of this report. Numerous other designs are possible and, at this time, the best choice is not clear. In general, both transmission and reflection optics could be used. The precision with which components must be made is very much less than in the infrared portion of the spectrum but somewhat greater than for microwaves. Therefore, even the materials and construction techniques that might be used are not well-defined. Considerable time and effort may be saved by using microwave techniques for collectors and scanning components, wherever possible. It is recommended that a detailed design study be conducted for the purpose of defining a real-time 1-milliradian imaging system which uses radiation emitted in the submillimeter wavelength portion of the spectrum.

The present feasibility system can be of considerable value during the development of detector sources and system design. Detectors and mounting techniques can be performance-tested. Atmospheric effects and image quality at increased ranges can be checked. Present sensors can be used to measure material properties such as transmissivity and reflectivity. Some aspects of an active system in which the target is illuminated can be investigated. The ability to test techniques on an operating imaging system should prevent many surprises in the construction of a prototype.

REFERENCES

1. R.A. Smith, F.E. Jones, and R.P. Chasmar, *The Detection and Measurement of Infra-Red Radiation*, Oxford England, the Clarendon Press, 1968, p. 82.
2. M.A. Kinch and B.V. Rollin, *British Journal of Applied Physics*, Volume 14, 1963, p. 672.
3. M.A. Kinch, *Proceedings of the Physical Society*, Volume 90, 1967, p. 819.
4. H.P. Baltes et al., "Spectral Densities of Cavity Resonances and Black Body Radiation Standards in the Submillimeter Wave Region," *Proceedings of the Symposium on Submillimeter Waves*, Polytechnic Press, April 1970, Vol. XX, p. 667.
5. G.E. Stillman, C.M. Wolfe, and J.O. Dimmock, *Proceedings, Symposium on Millimeter Waves*, Microwave Research Institute Symposia, Volume 20, Polytechnic Institute of Brooklyn, New York, 1970, p. 345.
6. J.L. Pipher and J.R. Houck, "Black Paints for Far Infrared Cryogenic Use," *Applied Optics*, Volume 10, 1971, p. 567.
7. N.I. Furashov, "Far Infrared Absoprtion by Atmospheric Water Vapor," *Optics and Spectroscopy*, Volume 20, 1966, p. 234.
8. K.D. Moller, D.J. McMahon, and D.R. Smith, "Far Infrared Transmission Filters for the 300- to 18-cm^{-1} Spectral Region," *Applied Optics*, Volume 5, 1966, p. 403.
9. Y. Yamada, A. Mitsuishi, and H. Yoshinga, "Transmission Filters in the Far Infrared Region," *Journal of the Optical Society of America*, Volume 52, 1962, p. 17.
10. A. Mitsuishi, Y. Otsuka, S. Fujita, and H. Yoshinga, "Metal Mesh Filters in the Far Infrared Region," *Japanese Journal of Applied Physics*, Volume 2, 1963, p. 574.
11. K.D. Moller, V.P. Tomaselli, L.P. Skube, and B.K. McKenna, "Far Infrared Vacuum Grating Spectrometer," *Journal of the Optical Scoeity of America*, Volume 55, 1965, p. 1233.
12. H.S. Carslaw and J.C. Jaeger, *Conduction of Heat in Solids*, 2nd Edition, Oxford Press, 1959, p. 100.
13. E. O'Neill, *Journal of the Optical Society of America*, Volume 46, 1956, p. 285.
14. A.H. Sheppard, K.H. Breeden, and A. McSweeney, "High Resolution Submillimeter Measurements of Atmospheric Water Vapor Absorption," *Submillimeter Waves*, Jerome Fox, Editor, Polytechnic Press, Brooklyn, New York, 1970, p. 445.
15. V.I. Rozenberg, "Radar Characteristics of Rain in Submillimeter Range," *Radio Engineering and Electronic Physics*, 15, 1970, p. 2157.
16. C.M.R. Platt "Transmission of Submillimeter Waves Through Water Clouds and Fogs," *J. Atmos. Sci.*, 27, 1970, p. 421.
17. D.R. Johnston and D.E. Burch, "Attenuation by Artificial Fogs in the Visible, Near Infrared, and Far Infrared," *Appl. Optics*, 6, 1967, p. 1497.
18. A.N. Vystavkin, V.N. Gubankov, V.N. Listvin and V.V. Migulin, *Sov. Phys.-Semiconductors 1*, No. 6, 1967, p. 702.
19. V.F. Bannaya, E.M. Gershenzon and L.B. Litvak-Govskaya, *Sov. Phys.-Semiconductors 2*, No. 7, 1969, p. 812.

20. V.F. Bannaya, E.M. Gershenzon and L.B. Litvak-Govakaya, *Sov. Phys.-Semiconductors 4*, No. 1, 1969, p. 159.

21. B.I. Shklovskii et al., *Sov. Phys.-Semiconductors 5*, No. 9, 1972, p. 1682.

22. R.C. Hofer, H. Jacobs, and J. Schumacher, "Visible Displays of Submillimeter and Millimeter Wave Images," *Proceedings of the Symposium on Submillimeter Waves*, Polytechnic Press, 1970, p. 553.

23. W.J. Burroughs, E.C. Pyatt, and H.A. Gebbie, "Transmission of Sub-Millimeter Waves in Fog," *Nature*, 212, 1966, p. 387.

24. T.Y. Chang, T.J. Bridges, and E.G. Burkhardt, "CW Submillimeter Laser Action in Optically Pumped Methyl Fluoride, Methyl Alcohol, and Kinyl Chloride Gases," *Appl. Phys. Lett.*, 17, 1970, p. 249.

25. T.Y. Chang, T.J. Bridges, and E.G. Burkhardt, "CW Laser Action at 81.5 and 263.4 μm in optically Pumped Ammonia Gas," *Appl. Phys. Lett.*, 17, 1970, p. 357.

26. T.Y. Chang and J.D. McGee, "Millimeter and Submillimeter Wave Laser Action in Symmetric Top Molecules Optically Pumped via Parallel Absorption Bands," *Appl. Phys. Lett.*, 19, 1971, p. 103.

27. K. Mizuno, S. Ono, and Y. Shibata, "A New Electron Tube with a Fabry-Perot Resonator for Generation of Millimeter and Submillimeter Radiation," *Proceedings of the Symposium on Submillimeter Waves*, Polytechnical Press, 1970, p. 115.

28. F.S. Rusin and G.D. Bogomolov, "Orotron—An Electronic Oscillator with an Open Resonator and Reflection Grating," *Proc. IEEE*, 1969, p. 720.

29. S.J. Smith and E.M. Purcell, "Visible Light from Localized Surface Charges Moving Across a Grating," *Phys. Rev.*, 92, 1953, p. 1069; I. Palocz and A.A. Oliner, "Leaky Space-Charge Waves II: Smith-Purcell Radiation," *Proc. IEEE*, 55, 1967, p. 46.

30. K. Mizuno, et al., "Craft Milling of the Grooved Mirror for the Fabry-Perot Resonator Used in the Submillimeter Wave Tube," *Record Elec. Comm. Eng. Conversation*, Tohoku University, 37, No. 4, 1969.

31. E. Lalor, "Three-Dimensional Theory of the Smith-Purcell Effect," *Phys. Rev. A*, 7, 1973, p. 435.

32. M.C. Teich, *Proceedings of the IEEE*, Volume 56, No. 37, 1968.

33. M.C. Teich, "Coherent Detection in the Infrared," *Semiconductors and Semimetals*, Volume 5, in *Infrared Detectors*, R.K. Willardson and A.C. Beer, Editors, Academic Press, 1970, pp. 361–408.

34. A.E. Siegman, "The Antenna Properties of Optical Heterodyne Receivers," *Proceedings, IEEE*, Volume 54, No. 10, 1966, pp. 1350–1356.

35. R.A. Brandewie, et al., *10.6 Micron Target Data (U)*, AFAL-TR-71-333, February, 1972 (CONFIDENTIAL).

36. R.A. Brandewie, et al., *Coherent Imaging and Moving Target Detection at 10.6 Microns (U)*, AFAL-TR-69-360, June 1970 (CONFIDENTIAL).